Wind Tunnel Studies of Decay and Spatial Diffusion of Turbulence

by

Adrien R. W. M. Thormann

A dissertation submitted to The Johns Hopkins University in conformity with the requirements for the degree of Doctor of Philosophy.

Baltimore, Maryland

August, 2015

Abstract

The study of homogeneous isotropic turbulence is one of the founding blocks of turbulence theory. It helps understanding the behavior of the Navier-Stokes equation in its most fundamental form and contributes to the development of numerical models. The first part of this thesis is dedicated to the study of decaying homogeneous isotropic turbulence generated by fractal active grids. The motivation for this study comes from previous studies of fractal-generated decaying turbulence which argued the existence of unusual decay behaviors. Specifically, exponential or very fast power law decays were reported instead of the widely accepted power-laws in times with decay exponents ranging between 1.0 and 1.4, approximately. These non-classical decays were later argued by other researchers to be limited to regions near the grid or perhaps to be due to low Reynolds numbers. In order to provide more definitive answers, in this work measurements are performed in the far field of a fractal grid at high Reynolds numbers. The results presented here exhibit power-law decays with decay exponents ranging approximately between 1.0 and 1.3, confirming that even fractal-generated grid turbulence conforms to classical decay laws.

ABSTRACT

The second part of the work also explores the decay of the turbulent kinetic energy, but including possible effects of spatial diffusion. An initial nearly-uniform gradient of kinetic energy of the form $k \sim \beta(y - y_0)$ is introduced in a flow with zero mean shear (y is the spanwise direction). In the wind tunnel this type of flow is achieved by combining spatially varying winglet geometries in the active grid placed downstream of a mesh with spatially varying solidity. The measurements taken in the test section with in-house built hot-wire anemometers show that at all spanwise locations the decay in the streamwise direction follows a power-law but with exponents $n(y)$ that depend upon the spanwise location. The third part of this thesis revisits the previous problem while using different instruments. The Princeton-made nanoscale thermal anemometers (NSTAP) are used to study the decay and achieve full resolution of viscous range to accurately determine dissipation. These data then enable us to evaluate the gradient of the transverse spatial flux of the turbulent kinetic energy. The same dependence between the initial distribution of kinetic energy and the decay exponent were recovered. The results presented also suggest (but do no prove) the presence of a strong lateral flux of turbulent kinetic energy going up-gradient, from the low kinetic energy side to the high kinetic energy side of the initial distribution. The measurements do not prove up-gradient transport since another possibility to explain the measurements is down-gradient transport, but with a diffusion coefficient that increases in the direction of decreasing turbulent kinetic energy. We comment on other possible reasons for the surprising findings and on the need for Direct Numerical

ABSTRACT

Simulations of this flow to provide simultaneous pressure-velocity data.

Primary Reader: Dr. Charles Meneveau

Secondary Readers: Dr. Dennice Gayme and Dr. Tamer Zaki

Acknowledgments

I would first like to acknowledge and thank my advisor, Dr. Charles Meneveau. The work presented in this thesis would not have been completed without his support, patience, and guidance. I would also like to thank Dr. Dennice Gayme, Dr. Tamer Zaki, and Dr. Gergory Eyink for their insightful suggestions, and the faculty of the Mechanical Engineering Department for the excellent academic education I have received during my doctoral studies.

I also acknowledge and thank Dr. A. Smits, Dr. Hultmark, and Yuyang Fan for their generous contributions and help with the NSTAP system.

To my colleagues, family, and friends for their help, good spirit, and support, which greatly contributed to this work. In particular, I would like to thank Dr. Claire Verhulst, Dr. Michael Wilczek, Dr. Richard Stevens, Dr. Jason Graham, Dr. Kunlun Bai, Juliaan Bossuyt, Perry Johnson, Theo Drivas, Adam Sierakowski, Brendan Hagan, Tim While, Mike Howland, and Vincent Rolin.

The financial support from the National Science Foundation (CBET 1033942) is gratefully acknowledged.

ACKNOWLEDGMENTS

Dedication

À mon cher grand-père, Dr. Wolfgang E. Thormann, à qui aucune dédicace ne saurait exprimer tout ce que je ressens. Je le remercie pour le soutien exemplaire et l'amour exceptionnel qu'il m'a porté. Je lui rends hommage par ce travail en guise de reconnaissance et d'admiration.

Contents

List of Tables

List of Figures

Chapter 1

Introduction

1.1 The Nature of Turbulence

Turbulence plays a major role in our world and we have a myriad of occasions to observe it on a daily basis. Whether it is the flow of a river going around a rock, the smoke coming out of a chimney in the winter time, or feeling gusts of wind when walking outside, turbulence is always around us. It also controls the way houses are heated or cooled, the way cars behave on the highway, or the way airplanes fly. More than that, turbulence is also responsible for the transport of pollen from one location to another, or even for the dispersion of pollutants away from cities. All these examples could potentially have positive or negative impacts on our society, or on our everyday life, so having a deeper physical understanding of the field is of great importance.

CHAPTER 1. INTRODUCTION

Turbulent flows are often very complex; they encompass and interact with a wide array of scales, as can be seen in Figure 1.1. These scales can range from microscopic scales (1.1 (A)), to mesoscales (1.1 (B)), and all the way up to astrophysical scales in the case of magnetohydrodynamics (MHD) (1.1 (C)). One can observe in all these images, eddies of multiple sizes, attesting of a strongly fluctuating velocity field. These fluctuations, both in position and time, are a characteristic feature of turbulent flows but are also what makes the field challenging to study. In fact, turbulence has a unique place in the field of classical physics in that regard. Its governing equations (the Navier-Stokes equations) have been known for more than 150 years, but yet, we are still unable to predict precisely the behavior of a turbulent fluid flow.

Nonetheless, these flows are heavily studied and many approaches and techniques have been developed to acquire a deeper fundamental understanding, and also to achieve and complete engineering projects. However, these projects often rely on simpler models that do not capture the full complexity of the flow. The building blocks of these models are commonly derived from the most fundamental and simple of turbulent flows, namely homogeneous isotropic turbulence. This type of flow has the advantage of being statistically invariant under translation or rotation, thus simplifying the governing equations, as will be illustrated in the following section.

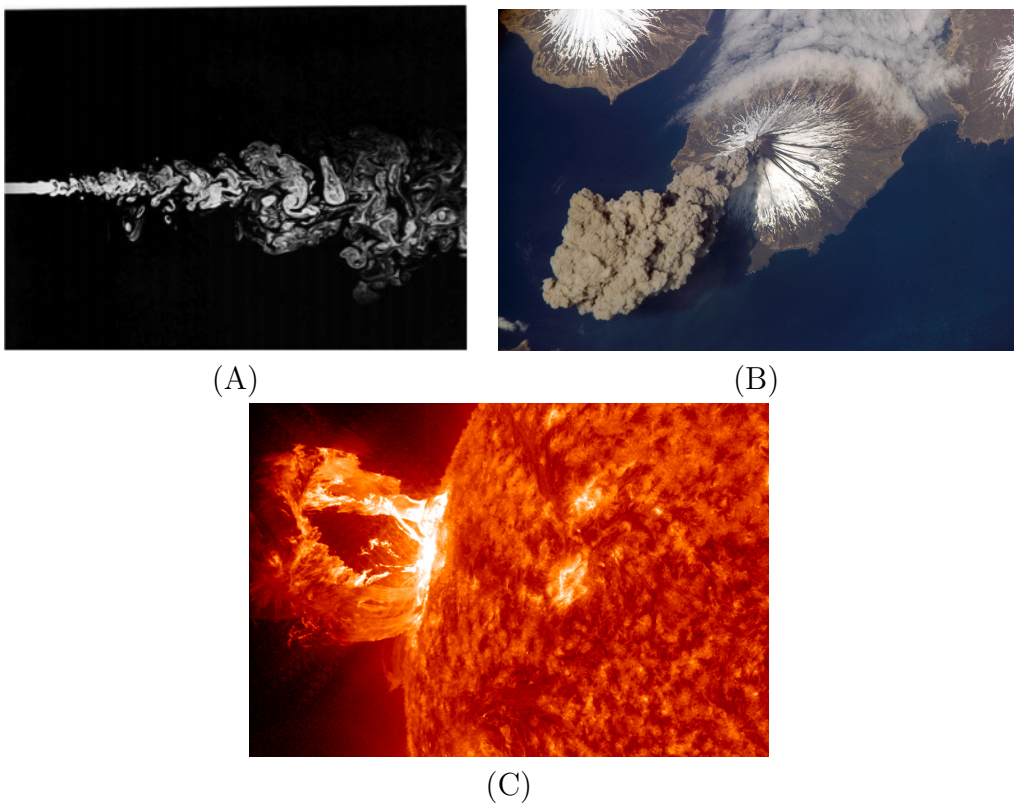

(A) (B)

(C)

Figure 1.1: (A): Photograph of a turbulent jet (taken from Van-Dyke's *An Album of Fluid Motion*). (B): Eruption of the Cleveland Volcano, Alaska, photographed from the International Space Station (www.nasa.gov). (C): Coronal mass ejection (CME) shot off the sun on April 16, 2012 (www.nasa.gov).

1.2 Motivation

To provide a quantitative description of the kinetic energy in a turbulent flow and illustrate the complexity underlying the physics of turbulence, one can look at the governing equation for the transport of kinetic energy in a turbulent flow. It is expressed by the following relation:[1–3]

$$\frac{dk}{dt} + \nabla \cdot \mathbf{T} = \mathcal{P} - \epsilon \tag{1.1}$$

where k is the turbulent kinetic energy defined by $k = \frac{1}{2}\langle u_i' u_i' \rangle$. In this notation, the Reynolds decomposition is used to express the turbulent velocity field u_i in terms of the mean velocity $\langle u_i \rangle$ and its fluctuations u_i' such that: $u_i = \langle u_i \rangle + u_i'$. The first term is the mean substantial derivative defined by $\frac{dk}{dt} = \frac{\partial k}{\partial t} + \langle u_i \rangle \frac{\partial k}{\partial x_i}$. Then, the transport term $\nabla \cdot \mathbf{T}$, is the divergence of $T_j = T_j^u + T_j^{p'} + T_j^\nu$, i.e. the sum of the following terms: $T_j^u = \left\langle u_j' u_i' u_i' \right\rangle$ which represents the turbulent convection, $T_j^{p'} = \left\langle u_j' p' \right\rangle / \rho$ is the pressure transport, and $T_j^\nu = -2\nu \langle u_i' s_{ij} \rangle$, the viscous diffusion. On the right side, $\mathcal{P} = -\left\langle u_i' u_j' \right\rangle \frac{\partial \langle u_i \rangle}{\partial x_j}$ is the production of turbulent kinetic energy, and finally, ϵ is the dissipation rate defined by: $\epsilon = 2\nu \langle s_{ij} s_{ij} \rangle$. In these expressions $s_{ij} = \frac{1}{2}\left(\frac{\partial u_i'}{\partial x_j} + \frac{\partial u_j'}{\partial x_i}\right)$ is the fluctuating strain rate tensor.

In the absence of a mean velocity gradient, this equation can be reduced to the

following for decaying turbulence since no production of energy is present in a flow:

$$\frac{dk}{dt} + \nabla \cdot \mathbf{T} = -\epsilon \tag{1.2}$$

Finally, one can further simplify this expression for decaying turbulence in homogeneous isotropic flows to the following, where no spatial diffusion is present:

$$\frac{dk}{dt} = -\epsilon. \tag{1.3}$$

The theory of homogeneous isotropic turbulence and the study of its kinetic energy decay dates back to G.I. Taylor and Von-Kármán in the 1930s,[4,5] and the topic has been studied extensively since then.[6–12] The traditional view of the energy decay is a power law in time t of the form:

$$k = k_0 \left(\frac{t}{t_0} \right)^{-n} \tag{1.4}$$

where k is the turbulent kinetic energy that has the value k_0 at some reference time t_0. The decay exponent n has been extensively studied and most experimental studies,[13–18] numerical studies[19–21] as well as the prominent theories,[10,22–24] found values between 1 and 1.4 (approximately), but no consensus has ever been reached over a unique value. However, the universality of this decay exponent is assumed in many engineering applications, especially in the $k - \epsilon$ model,[25] which is widely used for in-

dustry applications. It is a two equations model governed by the following relations:

$$\frac{dk}{dt} = \nabla \cdot \left(\frac{\nu_T}{\sigma_k} \nabla k \right) + \mathcal{P} - \epsilon \tag{1.5}$$

$$\frac{d\epsilon}{dt} = \nabla \cdot \left(\frac{\nu_T}{\sigma_\epsilon} \nabla \epsilon \right) + C_{\epsilon 1} \frac{\mathcal{P}_\epsilon}{k} - C_{\epsilon 2} \frac{\epsilon^2}{k} \tag{1.6}$$

where the energy flux $\mathbf{T}$ has been modeled with a gradient-diffusion hypothesis as follows

$$\mathbf{T} = -\frac{\nu_T}{\sigma_k} \nabla k. \tag{1.7}$$

The "turbulent viscosity" is specified by $\nu_T = c_\mu \frac{k^2}{\epsilon}$, thus solving for k and ϵ is needed to determine ν_T. It can then be used in the averaged momentum equation to obtain the mean velocity distribution. The constants listed in the expressions above are given by:

$$c_\mu = 0.09,\ C_{\epsilon 1} = 1.44,\ C_{\epsilon 2} = 1.92,\ \sigma_k = 1.0,\ \sigma_\epsilon = 1.33$$

The value of $C_{\epsilon 2}$ plays an important role in this model and it is directly related to the decay exponent n presented above, in equation 1.4. In the absence of a mean velocity gradient and spatial diffusion (i.e. for homogeneous isotropic turbulence

without production), the equations of the $k-\epsilon$ model can be reduced to

$$\frac{dk}{dt} = -\epsilon \qquad \text{and} \qquad \frac{d\epsilon}{dt} = -C_{\epsilon 2}\frac{\epsilon^2}{k}. \tag{1.8}$$

The first of these equations admits power-law solution of the form

$$k = k_0 \left(\frac{t}{t_0}\right)^{-n} \qquad \text{and} \qquad \epsilon = n\frac{k_0}{t_0}\left(\frac{t}{t_0}\right)^{-(n+1)}. \tag{1.9}$$

Replacing these power-law expressions in the second equation in 1.8 leads to $C_{\epsilon 2} = \frac{n+1}{n}$, and using the value quoted above for $C_{\epsilon 2}$ returns $n = 1.08$. This shows that having a better fundamental understanding of the decay rate exponent n will allow for more accurate predictions when using this popular model. The $k-\epsilon$ model is greatly prized for industrial applications due to its numerical robustness and relatively low computing power requirements. It is implemented in the most widely used CFD softwares, such as COMSOL$^{\text{TM}}$, Fluent$^{\text{TM}}$, or OpenFOAM$^{\text{TM}}$. For example, Figure 1.2 shows a snapshot of a simulation performed by the U.S. Department of Transportation for the Federal Highway Administration to evaluate the the hydrodynamic forces on bridge decks. This simulation used the implemented version of the $k-\epsilon$ model in the Fluent software (where $C_{\epsilon 2} = 1.92$). For studies that will have an impact on the safety of people, like the one presented above, or as a building block for theories and a benchmark for numerical simulations, it is therefore important to have a solid understanding of how rapidly homogeneous isotropic turbulence decays. Even

though decaying homogeneous isotropic turbulence is the 'simplest' turbulent flow to be studied, it is still not a solved problem, and thus additional empirically-obtained insights are valuable.

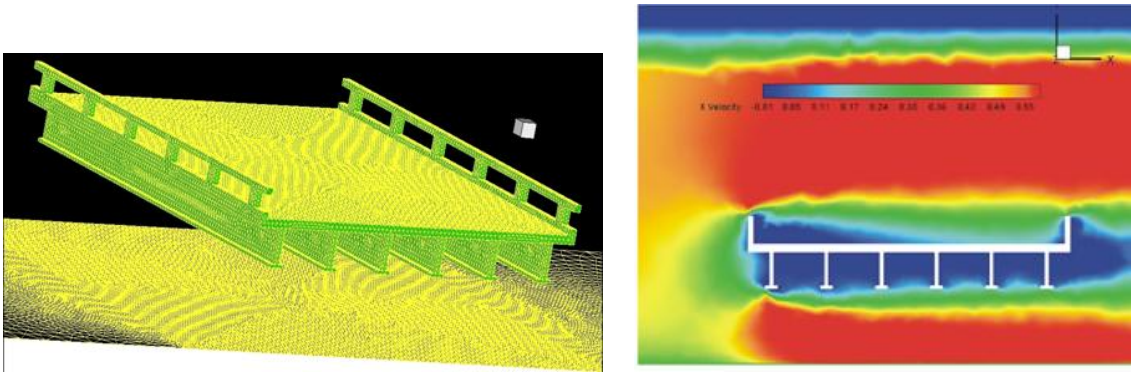

(A) (B)

Figure 1.2: Results from the Fluent^{TM} simulation using the $k-\epsilon$ model for a six-girded submerged bridge. (A): 3D rendering of the deck of bridge, (B): Snapshot of the velocity contours of the 3D model presented in (A). Figures reproduced from the U.S. DOT, Report: FHWA-HRT-09-028 (2009)

1.3 Grid Turbulence

The intrinsic complexity of the physics and mathematics that describe the hydrodynamics governing equations leaves room for different opinions and theories to arise. The theories often have to be validated against experimental data in order to be accepted, or otherwise they will be dismissed. The simplest and most fundamental experiment that can be conducted takes the form of grid turbulence. In order to perform this type of experiment, a grid is placed upstream of the test section of a wind tunnel and a uniform flow is passed through it, as shown in figure 1.3. The

resulting flow is usually a good approximation to decaying homogeneous turbulence, and allows experimentalists to study the structure of turbulence in its most basic environment. As one can expect, many scientist have studied grid turbulence in many different wind tunnels using various designs of grids.

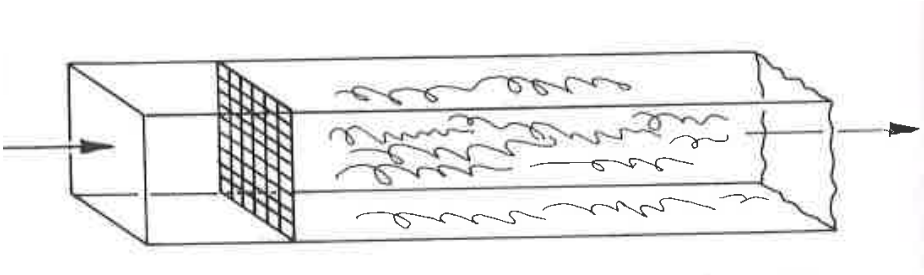

(A)

Figure 1.3: Schematic of grid generated turbulence. Figure taken from P. A. Davidson.[3]

Among all these studies, the most notable and cited studies are the ones of Comte-Bellot and Corrsin[14,26] performed in the very same wind tunnel as the one used to gather the data presented throughout this thesis. In these studies, a wide array of passive grids composed of static bars and rods arranged in a mesh pattern were used, similar to the sketch presented in figure 1.4 (A). One should note that these grids can be characterized by a single characteristic lengthscale. The results by Comte-Bellot and Corrsin on decaying homogeneous isotopic turbulence remain today a reference for all scientists studying grid turbulence, and will be presented in this report.

More recently, more elaborate and complex static grids have been used to study experimental decaying turbulence.[16,17,27–30] In particular, these studies renewed the interest in the field of such experiments by introducing grids with multiscale geometry.

They allow experimentalists to study the behavior of flow when energy is initially injected at a multitude of lengthscales, as opposed to the single-lengthscale energy injection of traditional grids. An example of the design of such grids is illustrated in figure 1.4(B) & (C). The results of these studies will be discussed in greater depth in Chapter 3.

Another class of grids can be used in place of the ones presented above. Conventional grids used in wind tunnels generate turbulence only up to moderate Reynolds numbers. Typically we find $150 \leq Re_\lambda \leq 200$, unless very large (or pressurized) facilities are used.[9,18,31] Makita[32] proposed a new type of grid to increase the turbulent Reynolds number without having to increase the size of the facility by using active turbulence generators. This new type of active grid is composed of agitator winglets attached to rotating rods, each independently controlled by external motors, as shown in figure 1.4 (D). The novelty of this configuration is that it generates a time-varying blockage ratio. Active grids have been used in various wind-tunnels[15,33–38] and have reached $Re_\lambda \approx 1500$,[36] as well as showing good levels of homogeneity and isotropy. In this document, the term "active grid" will refer to the Makita-type of mechanically activated grid. More details on the active grid used for the work presented in this thesis will be presented in the following section (1.3.1).

All the grids described above, whether they are 'passive' or mechanically controlled, rely on the interaction of jets and wakes induced by the designed blockage to generate a turbulent flow. In 1965, Mathieu and Alcaraz[39] proposed a new concept for

turbulence generation which involved a combination of controllable jets and passive grid. Gad-el-Hak and Corrsin[40] used a similar apparatus where the injecting nozzles are facing both 'downwind' and 'upwind'. Turbulence intensities were found to be higher than in the non-injecting case, but higher anisotropy levels were also recorded. More recently, Thole et al.[41] implemented cases where high velocity jets were inserted perpendicular to the free stream, both in a water channel and in a wind tunnel. This method resulted in highly turbulent flows with turbulence intensity reaching 20%. This work was motivated by the study of gas turbine, where high levels of turbulence intensities are found ($20 - 30\%$[41]), translating to Taylor Reynolds numbers ranging from $159 \leq Re_\lambda \leq 270$. These levels, higher than previous passive grid experiments, were obtained by varying the jet-to-maintream velocity ratio. However, they resulted in high anisotropy ratio where the spanwise component, v' was found to be lower than the streamwise component, u', by 30%.

1.3.1 The Corrsin Wind Tunnel Active Grid

A Makita-type of active grid is used in the experiments presented in this thesis. It is placed in the wind tunnel facility following the secondary contraction, which marks the beginning of the test section (due to structural reasons the grid could not be placed upstream of the secondary tunnel contraction, which would have been beneficial to improve turbulence isotropy[14]), as shown in figure 1.5. The grid is composed of

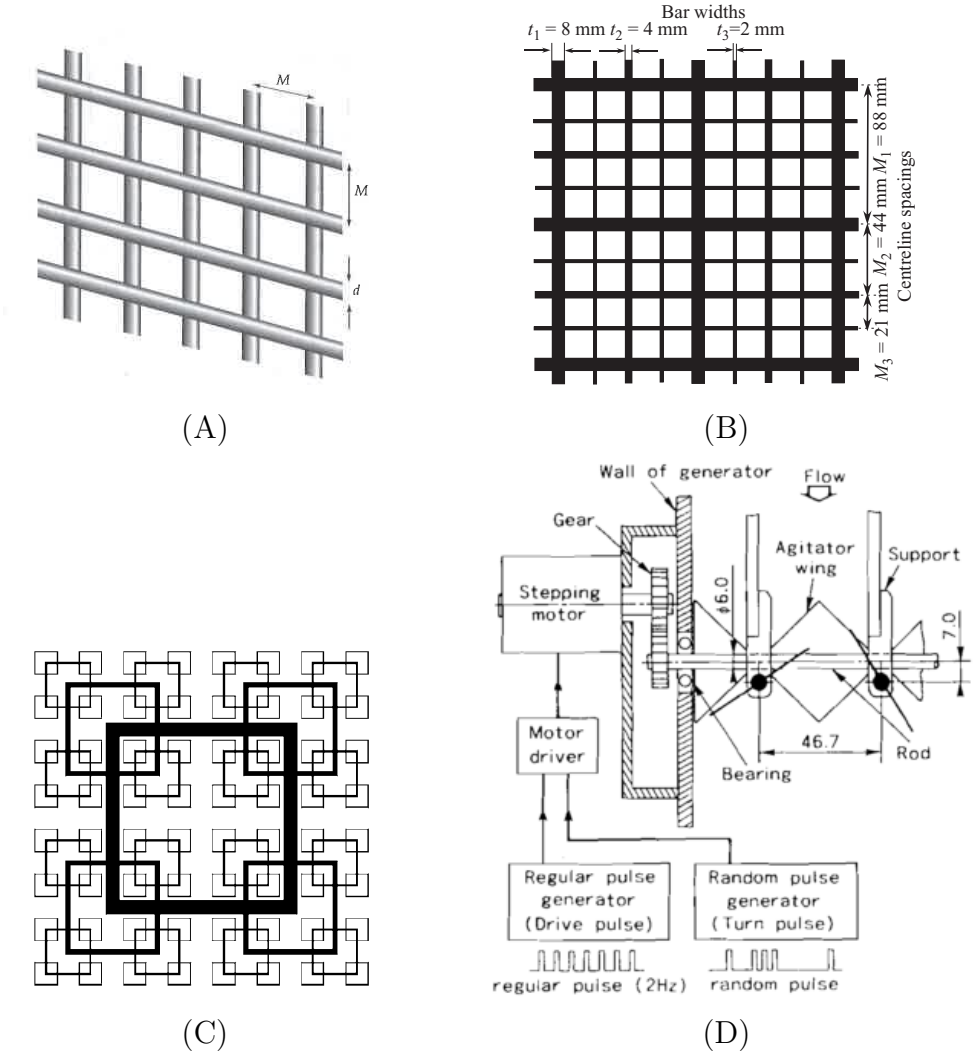

Figure 1.4: Various types of turbulence generating grids: (A) Classic mesh-type passive grid, (B) Multiscale passive grid, figure reproduced from Krogstad & Davidson,[16] (C) Fractal passive, figure reproduced from Hurst and Vassilicos,[27] (D) Detail of the active grid control system, figure reproduced from Makita[32]

seven vertical and five horizontal rotating square aluminum shafts, each independently driven by 1/4 hp motors. The shafts can be suited with up to 82 agitators, or winglets, to generate high-intensity turbulence depending on the experimental setup. The rods are placed every 15.2 cm, representing the 'mesh size' of this grid. It is also the closest the winglets can be spaced. The motors have a rotation rate which varies between 210 and 420 r.p.m., in both directions, separated by random time-intervals. More details on the setup of the grid for the different experiments are discussed in the corresponding sections below.

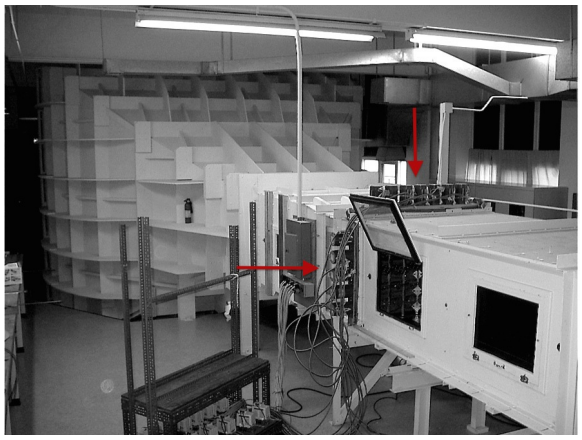

(A)

Figure 1.5: Overview of the primary and secondary contractions of the S. Corrsin Wind Tunnel. The red arrows point to the location of the active grid, located downstream of the secondary contraction.

1.4 Hot Wire Anemometry

In this section, a brief introduction to hot wire anemometry is presented in order to provide the reader with a basic understanding of their operation as hot wire

probes were extensively used for the studies presented in this document. More in depth information about this topic can be found in various articles and books cited in the bibliography,[14,15,37,42] and a step-by-step manufacturing guide is provided in Appendix A.

Hot wire probes have been used since the late 1800's originally in the form of the simple constant current anemometer. The word *anemometer* itself implies that the instrument is only to be used in air (from the greek *anemos*), but they can be used in many other fluids. Measurements can be made in fresh or salted water, polymer concentrations, oil, and various gases (among others), but also in compressible flows.

Hot wires are relatively inexpensive and have a very high frequency response, a good spatial resolution, and an excellent sensitivity, which makes them extremely attractive to researchers in labs around the world. The sensor of a hot wire probe is typically made of a $1 - 0.5$ mm long tungsten wire. To avoid edge effects, the length-to-diameter ratio has to be kept around 200, which means that the diameter of the wire will range from 5 to 2.5 μm - much thiner than a human hair. The scale of these wires implies that they are extremely fragile instruments but also that the manufacturing process has to be done under a microscope.

The sensor is heated by a passing current, which then gets convectively cooled by the measured fluid. It is this difference in temperature that is translated into a measure of the fluid velocity. Hot wire probes can be operated under constant current (CCA), or constant temperature mode (CTA). The heating current flowing through

the sensor varies with the fluid velocity in order to maintain a constant resistance across the wire, and keeping the resistance constant directly translates to having a constant sensor temperature.

In order to achieve this operation, the heart of the electronic package that controls a CTA system is a Weatstone bridge, with the sensor acting as one of the resistances, as seen in figure 1.6(A). The circuit is completed by an adjustable resistance, and two constant ones. A feedback loop is used to sense when the bridge is unbalanced, and increases (or decreases) the current in order to keep the temperature of the sensor constant. The adjustable resistance of the Weatstone bridge is set to a higher resistance than the probe itself using an appropriate 'over-heat ratio' to unbalance the bridge (note: the over-heat ratio is typically set around 1.6 for the half-millimeter probes used in this study). If it is set too high the probe will burn out once a heating current passes through it, but if it is set too low, the sensor will not be sensitive enough. When power is applied, the resistance of the sensor will rise, and thus the temperature will too, until the Weatstone bride is balanced. The sensor will cool down or heat up if an increase or a decrease in velocity occurs in the measured fluid, forcing the bridge to become unbalanced. This sudden change in resistance will force the feedback amplifier to increase or decrease the current in the circuit in order to bring the bridge back to a balance. As a result, the voltage difference measured across the bridge will be directly proportional to the fluid velocity. Using prior calibrations, one can easily convert the outputted voltage into physical velocity measurements.

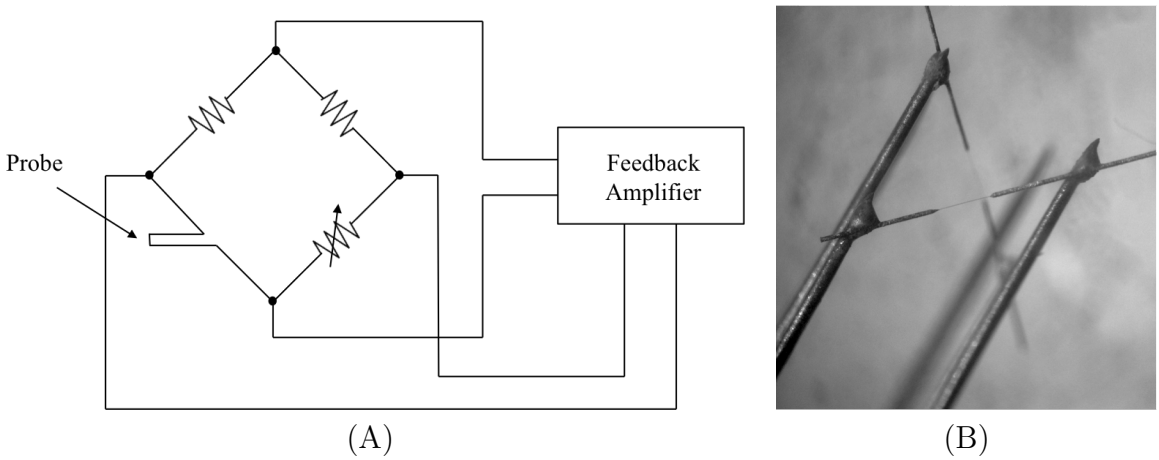

Figure 1.6: (A): Schematic of the components comprising a Constant Temperature Anemometer. (B): In-house built 0.5 mm two-component hot-wire probe.

The in-house built probes used for the experiments described in this manuscript are two-component anemometers. The X-wire design consists of two orthogonal arrays of sensor inclined at a 45^o with respect to the axis of the probe. This configuration allows to measure two perpendicular components of the flow: the streamwise component, and either the horizontal or the vertical one.[42] Three component anemometer also exist, but require a more intricate design. The in-house built X-wires are made out of 0.5 mm long and 2.5 μm wide tungsten wires (cf. figure 1.6(B)). The wires are first electroplated with copper for better handling, and then etched until the desired active length is obtained. More details about the manufacturing process of the in-house built hot wire can be found in Appendix A.

More recently, a new kind of hot-wire anemometer was developed at Princeton.[43–48] The nanoscale thermal anemometer probe (NSTAP) works as a constant temperature anemometer, hence following the rules of operation described above, but the novelty

lies in the length of its active wire. The NSTAP has a free standing 60 or 30 μm long, 1 μm wide, and 0.1 μm thick platinum filament with a frequency response exceeding 300 kHz. In order to reach such scales, the manufacturing process relies on deep reactive ion etching (DRIE) together with other MEMS fabrication technique (see Vallikivi & Smits[44] for more details). These probes are revolutionizing the field of hot-wire anemometry as they allow the user to resolve the smallest scales in the flow, and hence give a complete picture of the energy cascade. As an example, the flows presented in this thesis typically have Kolmogorov scale on the order of 100 μm, therefore having the resolution provided by the NSTAP is desirable over the 0.5 mm (500 μm) in-house built probes. The NSTAP is currently a single component anemometer, but at the time of the writing of this document, the Princeton team was in the process of manufacturing two-component nanoscale thermal anemometers. The single component probes are used in the study presented in Chapter 5, and a step-by-step user guide is provided in Appendix B.

1.5 The Stanley Corrsin Wind Tunnel

Dr. Stanley Corrsin was awarded in 1958 by the National Science Foundation a grant entitled "Construction of a Low Speed, Low Turbulence Wind Tunnel" for $\$165,000$. In the proposal, he motivates the need of such facility with five potential research activities: "The Nature of Isotropic Turbulence", "Isotropic Turbulent Mix-

ing", "Turbulent Dispersion from Localized Sources", "Axi-symmetric Turbulence and Temperature Fluctuations", and "Gradient Heat Transfer in Isotropic Turbulence", all of which are still active research topics today. The construction of the Wind Tunnel began in 1959 in Maryland Hall, on the Johns Hopkins University Homewood campus in Baltimore, MD. By 1966, a study was published with Dr. Comte-Bellot, a post-doctoral fellow working with Dr. Corrsin at the time, entitled "The Use of a Contraction to Improve the Isotropy of Grid Generated Turbulence" in the Journal of Fluid Mechanics.[14] This publication reported on very precise and well conducted measurements of decaying homogeneous isotropic turbulence, and remains to this day one of the most cited and highly regarded works on the topic.

The facility, sketched in Figure 1.7, has a test section of 10 meters in length, and a cross section of 1.22 meters in width, by 0.91 meters in height. It is a closed loop facility with a 25:1 primary, and a 1.27:1 secondary contraction, which are located upstream of the turbulence producing grid used for this work due to structural and access limitations of the facility (for additional details, see Kang et al.[15] and Thormann and Meneveau[37]). The background turbulence intensity in the facility without the grid in place is less than 0.1%.

Fifty-seven years later, the work presented in this thesis is still in the line of study that Dr. Corrsin had set for this Wind Tunnel.

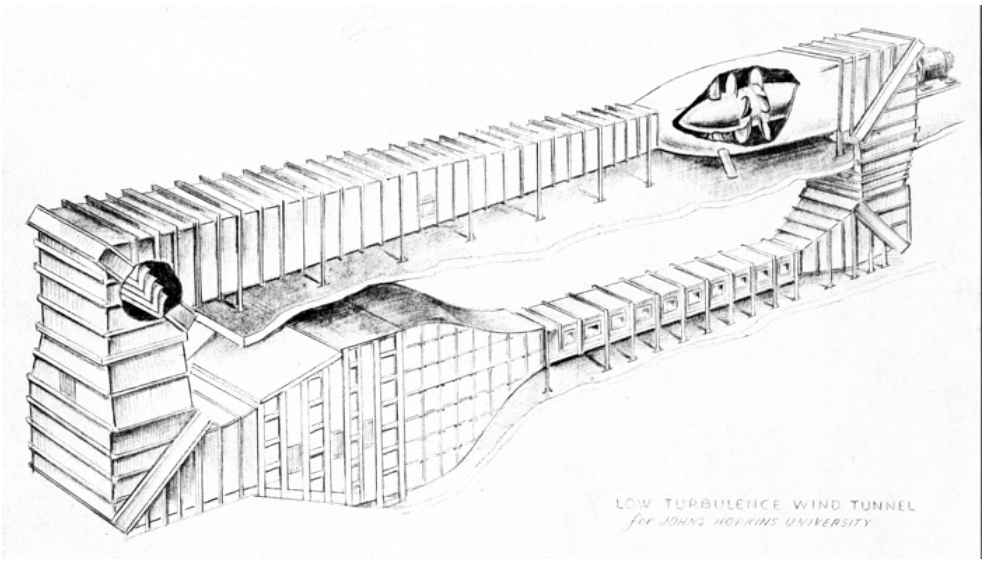

(A)

Figure 1.7: (A): Sketch of the Corrsin Wind Tunnel by Aircraft Armament Inc.

1.6 Guide Through This Thesis

Several studies on decaying turbulence are presented in this dissertation. Chapter 2 provides an overview of the main classical results in the literature on decaying turbulence. These are the foundations for the work presented in the subsequent chapters. Chapter 3 is devoted to the study of decaying homogeneous, isotropic turbulence behind fractal multiscale grids. The investigation focuses on possible deviations from classical predictions and observations. Chapters 4 & 5 focus on decaying turbulence in the presence of an initial kinetic energy gradient in a shearless flow. This non-standard flow is first studied using the in-house hot-wire anemometer (Chapter 4), and then revisited with higher spatial resolution in the following section (Chapter 5) using Princeton's nanoscale probes (NSTAP). Important additional materials can be

found in the appendices. Additionally, Appendices A & B are provided as guides on the techniques developed for the different hot-wire anemometry systems used for the studies presented in this thesis, and are meant to assist future experimentalists in this laboratory. Note that the material presented in Chapter 2 & 3 has been published in Ref.[37] and the work described in Chapter 4 has been published in Ref.[38]

Chapter 2

Overview of Decaying Turbulence

2.1 Power-law Decay

The theory of homogeneous isotropic turbulence and its decay dates back to G.I. Taylor and Von-Kármán in the 1930's,[4,5] and the topic has been studied extensively since then.[3,6–11] Some recent papers,[16,19,49] as well as a rather complete Annual Review of Fluid Mechanics article[12] provide useful reviews. The conceptually most salient points are summarized below.

The traditional view of the energy decay is a power law of the form:

$$k \sim t^{-n}, \tag{2.1}$$

where $k = \frac{3}{2}\langle u'^2 \rangle$ and u' is a component of the fluctuating velocity. The averaging is

meant to be over directions of statistical homogeneity, and time t is measured from some appropriate initial condition. For the rest of this section, we define the turbulent velocity scale according to $u = \langle u'^2 \rangle^{1/2}$. The most prominent predictions for the decay exponent are the ones based on Kolmogorov and Batchelor,[22,23] Saffman[24] and the fully self-similar decay.[23]

2.2 The Kolmogorov Decay Law

The Kolmogorov prediction can be motivated by considering the Kármán-Howarth equation:[50]

$$\frac{\partial}{\partial t}\left(u^2 f(r,t)\right) = \frac{u^3}{r^4}\frac{\partial}{\partial r}\left(r^4 g(r,t)\right) + 2\nu\frac{u^2}{r^4}\frac{\partial}{\partial r}\left(r^4\frac{\partial f(r,t)}{\partial r}\right) \tag{2.2}$$

where $f(r,t)$ and $g(r,t)$ are the two-point second and third-order longitudinal velocity correlation functions. When multiplied by r^4 and integrated from $r = 0$ to $r \to \infty$ (r is the distance between two points), Equation 2.2 reads:

$$\frac{\partial}{\partial t}\left[u^2 \int_0^\infty r^4 f(r,t)\ dr\right] = \left[u^3\ r^4 g(r,t)\right]_\infty + 2\nu\left[u^2 r^4 f'(r,t)\right]_\infty, \tag{2.3}$$

If one makes the assumption that $f(r,t)$ and $g(r,t)$ decay sufficiently fast as $r \to \infty$, then only the left hand side of the equation remains. This term, the Loistsyansky

integral, is thus invariant in time leading to the following scaling:

$$I \;=\; u^2 \int_0^\infty \; r^4 f(r,t)\; dr \;\sim\; u^2 \ell^5 \;\sim\; t^0, \tag{2.4}$$

where ℓ is the characteristic integral scale characterizing the correlation function, i.e. $\ell = \int_0^\infty f(r,t)dr$. The constancy of I implies that if $u^2 \sim t^{-n}$ then $\ell \sim t^{n/5}$. Combined with the kinetic energy equation and the 'dissipation anomaly' assumption (namely that $\epsilon = C_\epsilon\, u^3/\ell$ where C_ϵ is assumed to be constant in time) underlying Kolmogorov's turbulence phenomenological theory, one obtains

$$\frac{3}{2}\frac{du^2}{dt} = -\epsilon = -C_\epsilon \frac{(u^2)^{3/2}}{\ell} \sim -t^{-3n/2-n/5}. \tag{2.5}$$

When equated to $du^2/dt \sim -n\; t^{-n-1}$ one obtains[23] $n = 10/7$. The assumption that C_ϵ remains constant in time (or at least that if it varies it does so much more slowly than as a power-law in time) is crucial in this derivation.

2.3 The Saffman Decay Law

The Loistsyansky invariant can be related to the low-wavenumber behavior of the energy spectrum. The radial energy spectrum is defined according to

$$E(k,t) = \frac{1}{\pi}\int_0^\infty \langle \mathbf{u}(\mathbf{x})\cdot\mathbf{u}(\mathbf{x}+\mathbf{r})\rangle kr\ \sin(kr)\ dr, \tag{2.6}$$

where $\langle \mathbf{u}(\mathbf{x})\cdot\mathbf{u}(\mathbf{x}+\mathbf{r})\rangle$ is the two-point correlation function separated by a distance r. Assuming that $E(k,t)$ is analytic at $k=0$ (other options including a family of invariants and non-analyticity at $k=0$ are discussed in recent papers[51–54]), a Taylor expansion at small kr shows the following leading terms:

$$E(k,t) = \frac{Lk^2}{4\pi^2} + \frac{Ik^4}{24\pi^2} + ... \tag{2.7}$$

where I is the Loitsyansky integral discussed above, and L is Saffman's integral, defined by:

$$\begin{aligned} L = \int \langle \mathbf{u}(\mathbf{x})\cdot\mathbf{u}(\mathbf{x}+\mathbf{r})\rangle d^3\mathbf{r} &= \int \frac{u^2}{r^2}\frac{\partial}{\partial r}\left(r^3 f\right) d^3\mathbf{r} \\ &= 4\pi u^2 \int_0^\infty \frac{\partial}{\partial r}\left(r^3 f\right) dr = 4\pi u^2 \left[r^3 f\right]_{r\to\infty}. \end{aligned} \tag{2.8}$$

If $L=0$ (if $f(r,t)$ decays sufficiently fast at large r), one recovers the Loistsyansky invariant as the most dynamically relevant constraint at large scales. If $L\neq 0$ (i.e.

$f(r)$ does not decay sufficiently fast at large r), then it instead may play the most dominant role for the large scales of turbulence. If it remains invariant in time, then:

$$L = 4\pi u^2 \left[r^3 f\right]_{r\to\infty} \sim u^2 \ell^3 \sim t^0. \tag{2.9}$$

This leads, when combined as before with Eqs. (2.1) and (2.5), to a kinetic energy decay exponent[24] of $n = 6/5$.

2.4 The Self-similar and Exponential Decay Laws

Assuming a self-similar decay in which spectra and correlation functions involve a single length-scale but the dynamics include effects of both inertial and viscous terms, one obtains that this length-scale must be the Taylor microscale $\lambda = (15\nu u^2/\epsilon)^{1/2}$.[10] With this single length-scale, it follows that $du^2/dt \sim u^3/\lambda$ since the decay time-scale must go like λ/u. When equated to $-\epsilon = -15\nu u^2/\lambda^2$, it yields that the Taylor Reynolds number $Re_\lambda = \lambda u/\nu$ remains constant, i.e. $\lambda \sim u^{-1}$ and thus $du^2/dt \sim u^4$. Upon using $u^2 \sim t^{-n}$ one obtains $-n-1 = -2n$ or $n = 1$, as originally pointed out by Batchelor[23] (and rejected by him as a suitable theory at that time). Another possibility elaborated upon by George[10] and Speziale & Bernard[11] is power-law decay with an exponent $n > 1$ that may depend on initial conditions. Yet another type of

decay is obtained if it is assumed that the Taylor scale λ remains constant in time during the decay.[27,55,56] Then from $\epsilon = 15\nu u^2/\lambda^2$, one obtains that $du^2/dt \sim -u^2$ and thus $u^2 \sim \exp(-Ct)$, i.e. exponential decay.

2.5 Experimental Investigations

As already summarized in section 1, the nature of kinetic energy decay is not only important from fundamental perspectives, but also for practical applications. It is embedded in the constant $C_{\epsilon 2}$ of the transport equation for dissipation rate ϵ in the popular $k-\epsilon$ model.[25,57] As described in the previous section, for homogeneous isotropic turbulence without production, the $k-\epsilon$ model's equation for dissipation coupled to power-law decay leads to the following constant $C_{\epsilon 2}$:

$$C_{\epsilon 2} = \frac{n+1}{n}, \tag{2.10}$$

Thus, knowing n can be used for calibration of the strength of the "dissipation of dissipation" parameter in the standard $k-\epsilon$ model.

Many experimental and numerical studies have been performed to study the rate of decay of isotropic turbulence. Well-known experiments including those performed by Comte-Bellot & Corrsin,[14,26] finding a decay exponent of about $n \approx 1.25$. Values in this range have since been reported more recently in experiments including those reported in Kang et al.[15] and Krogstad & Davidson.[16] Direct Numerical Simulations

of decaying isotropic turbulence, although restricted to lower Reynolds numbers compared to experiments, have tended to report power-law decays values of n in a broad range, Ref.[19–21]

Decaying isotropic turbulence is of particular interest also in the context of testing universality of various theories of turbulence and trends of turbulent flows to forget initial and boundary conditions. In particular, in works of W. K. George and coworkers[10] the possibility has often been highlighted that initial conditions may linger for extended periods of time and qualitatively change the entire flow evolution. For the decay of turbulence, dependence upon initial conditions could mean that the decay rate n depends on initial conditions, that the decay may even not be according to a power-law, or that the coefficient C_ϵ may depend on time during the decay. Since C_ϵ is a large-scale quantity, it is not expected to be universal and can vary from one flow to another also according to classical Kolmogorov theory.

Over the past several years, following works by Hurst & Vassillicos[27] and Mazellier & Vassilicos[28] there has been renewed interest in decaying turbulence, for the case when its initial condition has been significantly perturbed by injecting kinetic energy at a multitude of length-scales. Such non-classical flow conditioning was achieved using passive, space-filling square fractal grids.[27,28] Their work focused on the dissipation of energy in regions close to the grid, especially the behavior of the coefficient C_ϵ at various downstream distances. Of interest to the studies presented in this thesis, their works also touched on the decay rate of kinetic energy. Initially, the

measured decay rates showed evidence of exponential rather than power-law decay, in the near-field of the grid. Later, the same fractal grids were studied by Valente & Vassilicos[29] who reported power law decay with an elevated exponent, i.e. $n > 2$. Gomes-Fernandez et al.[30] use PIV to characterize the flow behind the space-filling fractal grid, in a region up to about three times the distance where the kinetic energy peaks in the near-field behind the grid. Within this region, they find that C_ϵ varies, whereas the ratio of Taylor and integral scale remains constant.

However, the far-field behavior of decay could not be established based on these measurements since the largest characteristic length-scale of the grid was not small compared to the wind tunnel cross-section. It is usually believed that for regular grid turbulence, past $x \gtrsim 30M$ or so[14] (where M is the mesh size of the grid), the production due to mean shear becomes negligible and the kinetic energy evolves only due to pure decay. As shown by Krogstad & Davidson[16,17] based on measurements using a different multiscale passive grid with three length-scales in which larger distances x/M could be reached, a likely reason for departures from classical power law decay was the proximity to the grid and the presence of some remaining mean shear.

Effects of Reynolds number have also been difficult to study due to inherent experimental limitations. Prior experiments were performed at relatively low Reynolds numbers, with values (once it has decayed to distances $x \gtrsim 30M$) typically ranging from $Re_\lambda \sim 80$ to 70 for the multi-scale experiments of Krogstad & Davidson.[16,17] A recent experiment in a passive fractal grid in which large x/M could be reached had

Reynolds numbers of about $Re_\lambda \sim 100$.[58] The study presented in Chapter 3 explores this topic at higher Reynolds numbers. At the time it was performed, the highest we could achieve due to structural limitations of the grid was $Re_\lambda \sim 300$.

Performing high Reynolds number experiments is a challenge and new approaches must be developed such as increasing the Reynolds number by increasing the density in a gas by pressurization. Recently, Sinhuber, Bodenschatz, and Bewley[18] reached very high Reynolds number using a traditional (non-multiscale) grid in the new Variable Density Turbulence Tunnel (VDTT)[59] at the Max Planck Institute for Dynamics and Self-Organization in Göttingen, Germany. Most recent grid turbulence experiments performed in wind tunnels have been contained within $100 \leq Re_\lambda \leq 600$, but the VDTT allowed the Max Plank Institute team to reach extremely high Reynolds Number, up to $Re_\lambda = 8000$.[36] The study reported by Sinhuber et al.[18] using this facility revealed a Saffman-like decay exponent with $n \approx 1.2$ using the Princeton-manufactured NSTAP.

Chapter 3

Decay of Homogeneous, Nearly Isotropic Turbulence Behind Active Fractal Grids

3.1 Introduction

The main objective of this study is to reconsider the question of decay of turbulence behind multi-scale or fractal grids, but now under conditions where more elevated values of Re_λ can be reached ($Re_\lambda \gtrsim 300$), while large enough values of x/M can be achieved so that production due to mean shear can be neglected. In this work, higher Reynolds numbers are achieved by using an active grid with fractal winglets. A fractal is defined as any shape of curve which appears to be self-similar

at any scale, namely, it appears to be repeated within itself an infinite number of times. A fractal object is often characterized by its fractal dimension, defined by: $D_f = log(N)/log(\varepsilon)$, where N is the number of children, and ε is the scaling factor of each generation. Measurements are performed behind three types of fractal winglets, namely the space-filling fractal shape already considered in prior experiments (with fractal dimension $D_f = 2$), as well as a classical Sierpinski triangular fractal (a self-similar sequence of triangles divided into four subtriangles in which the middle one is removed (more details provided below), with fractal dimension of $D_f \approx 1.58$) and an Apollonian fractal (a statistically self-similar sequence of embedded tangent circular holes (more details provided below), with fractal dimension of $D_f \approx 1.26$). For comparison, a fourth case with solid (non-fractal) winglets is considered. The experiments are repeated with the four types of grids rigidly fixed in a passive mode. As will be seen, a limitation of these data is the lack of complete velocity component isotropy. For three out of the four cases, the ratio of streamwise to cross-stream root-mean-square deviated from unity by 8-23%. In one of the cases (the Apollonian Packing fractal grid), very good isotropy was achieved. The experiments are described in Section 3.2, the flow characterizations are presented in Section 3.3, while results and conclusions are presented in Sections 4.4 and 4.5, respectively.

3.2 Experimental Setup and Active Grid

3.2.1 Wind Tunnel Facility

Experiments were performed in the Corrsin Wind Tunnel at the Johns Hopkins University. Details on the facility can be found in Section 1.5.

3.2.2 Active Grid Design

The active grid apparatus presented in section 1.3.1 is used for this work. The study seeks to investigate the role of the initial energy injection on the decay of kinetic energy in nearly homogeneous isotropic turbulent flows, thus new agitators winglets were designed to suit the grid's supporting rods.

One classic fractal shape is the Sierpinski Triangle, consisting of subdividing a triangle into four sub triangles of half the original scale, and deleting the middle one. As a result, the fractal dimension of the resulting set is $D_f = \log(3)/\log(2) \approx 1.58$. Here we use a right-triangle as the base figure so that two can be assembled into a square winglet. Figure 3.1 shows a sketch of the design considered for this geometry. The winglet are cut out of 2 mm thick acrylic sheets, using a laser cutter. A total of five generations are included, thus spanning a range of scales going from $M/2 \sim 8$cm down to $8\text{cm}/2^5 = 2.5$mm. On the edges, stationary half-winglets are attached to the frame of the active grid.

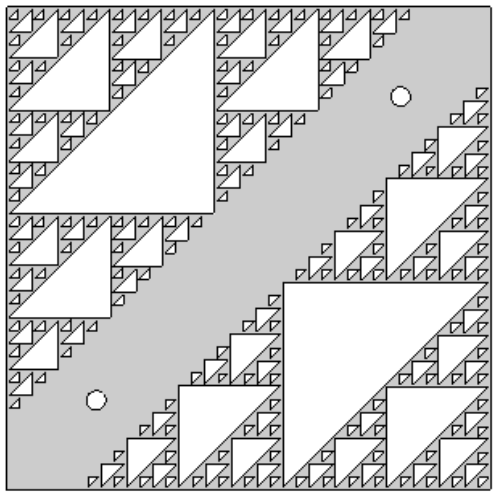

(A)

Figure 3.1: Schematic of the Sierpinski Triangle winglets.

Several other winglet shapes are considered: a Space Filling Square, an "Apollonian Packing" fractal, and a Non-Fractal (solid) winglet. The Space Filling Square winglet design (see Figure 3.2) is very similar to the one of Hurst & Vassilicos (2007), Mazellier & Vassilicos (2010), and Valente & Vassilicos (2011). Its construction (also cut out of acrylic plates) includes four generations, spanning scales from the largest square edge of 7.3 cm down to $73/2^4 = 4.56$ mm. At each scale reduction of 1/2 it quadruples the number of squares, and hence its similarity fractal dimension is $D_f = \log(4)/\log(2) = 2$.

The Apollonian Packing Design, shown in Figure 3.3, consists of inscribing and subtracting the largest possible tangent circles into successively narrower remaining gaps. We measured its fractal dimension using the box-counting method, and arrived at $D_f \sim 1.26$, quite close to the value $D_f \sim 1.306$ quoted[60] for an Apollonian Packing

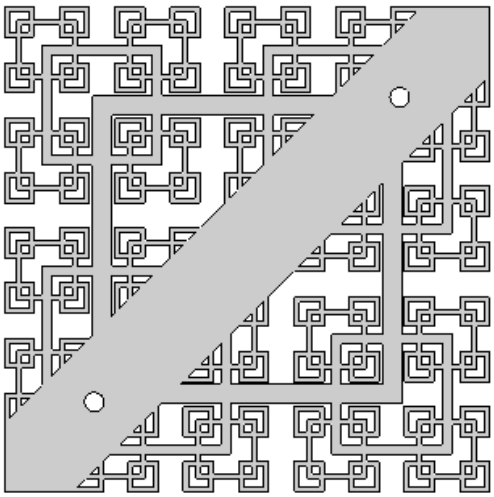

(A)

Figure 3.2: Space Filling Squares design.

that starts with three circles inscribed in a circle (rather than the present case of circle inscribed in a right triangle).

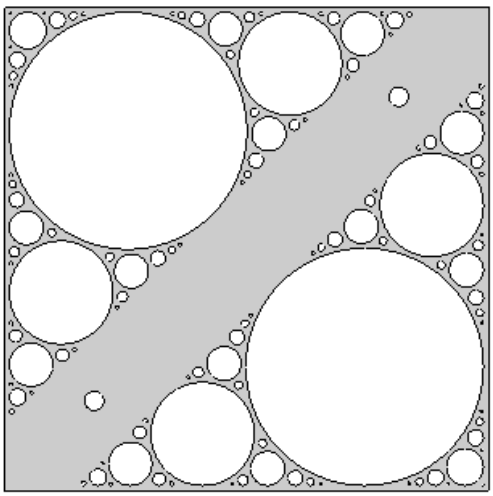

(A)

Figure 3.3: Rendering of the winglet geometry used for the Apollonian Packing Design

The fourth winglet, shown in Figure 3.4, is non-fractal and is to be used as a

comparison case as its scale is chosen to match the blockage area of the Sierpinski Triangle winglet. As will be documented below, the flows generated by these grids are close to homogeneous in the spanwise directions at about $x/M = 14$.

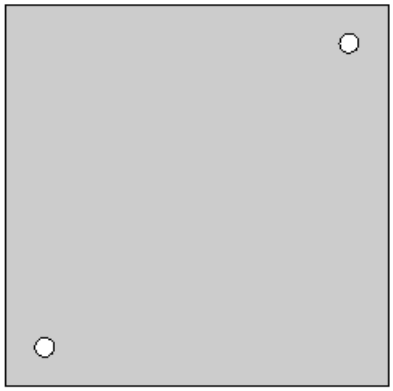

(A)

Figure 3.4: Non-Fractal winglet design used on the active grid

Figure 3.5(A) shows a sketch of the entire active grid, and Figure 3.5(B) shows a photograph of the active grid suited with the Sierpinski triangle winglets. Note that there are 8×6 replicas of such winglets across the section, enabling us to reach transverse homogeneous flow early in the decay (see homogeneity tests presented below). Furthermore, the main characteristics of each winglet design can be found in Table 3.1, where the blockage area and ratio listed include the surface area of the shafts.

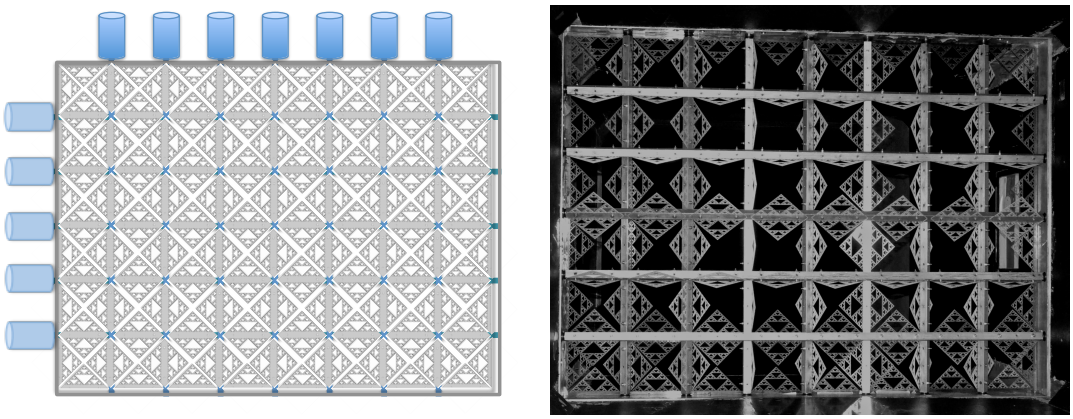

(A) (B)

Figure 3.5: (A) Schematic of the entire active fractal grid fitted with Sierpinski Triangle winglets. (B) Photograph of active grid with the Sierpinski triangle winglets.

Table 3.1: Geometrical characteristics of the various winglets fitted on the active grid.

	Sierpinski	Space Filling	Apollonian	Non-Fractal
Fractal Dimension	1.58	2.00	1.26	2.00
Blockage Area (cm^2)	62.7	58.9	38.6	62.7
Blockage Ratio	0.463	0.435	0.285	0.463

3.2.3 Passive Grids

The second set of data is measured behind a passive grid. The grid used is the same as the one presented in section 3.2.2 with the rods blocked such that the winglets remain perpendicular to the flow. However, for the case of the Space Filling Squares winglets the resulting mean profiles showed persistent deviations from uniformity. As a remedy, the angular positions of the static winglets are adjusted to generate (empirically) a more uniform mean velocity profile, as described in section 3.3.1.

3.2.4 Data Acquisition

Data are acquired using an in-house built X-wire probe. It is made using $2.5\mu m$ platinum-coated tungsten wire, which is copper-plated and soldered to the X-wire prong ends. The wires are then etched using droplets of nitric acid until the desired resistance is obtained, and then carefully cleaned. An active length-to-diameter ratio of ≈ 200 is achieved, leading to an active length of ≈ 0.5mm. The wire spacing between the hot wires is 0.5mm, and the slant angle of each sensor is 45^o. The probe is operated in a constant-temperature anemometry (CTA) mode, and is controlled by a TSI-IFA-300 system. The anemometer is calibrated using an overheat ratio of 1.55 in the core of an axisymmetric jet of a TSI automatic velocity calibrator using flow velocities spanning from 5 to 25 m/s, tailored from experiment to experiment. The angular calibration is performed at eleven different yaw angles α, with 6^o increments, and implemented according to the effective voltage relation:[61] $V^2_{\text{effective}} = V^2\left[\cos^2\alpha + k^2\sin^2\alpha\right]$, where k, the yaw coefficient, is determined experimentally through calibration. Calibration relies on a fourth-order polynomial as a function of output voltage. Calibrations and data acquisition are accompanied with thermocouple temperature measurements in order to compensate for any temperature increase in the wind tunnel which can occur during the course of the experiment. The temperature corrections applied to the corrected voltage are calculated as follow: $E = E_b\sqrt{(T_s - T_c)\,/\,(T_s - T_e)}$, where E_b is the bridge voltage, T_s is the sensor operating temperature, T_c is the fluid temperature measured during the

calibration, and T_e is the fluid temperature recorded during the experiment. The data are sampled at $40,000$Hz using a $20,000$Hz low-pass filter, for a total time of 52.43 seconds at each downstream location (over 2×10^6 samples). The decay of turbulence is captured by taking data at the following sixteen downstream locations: $x/M = [10, 12, 15, 17, 20, 22, 25, 27, 30, 32, 35, 37, 40, 42, 45, 50]$. The first two locations are not taken into consideration when fitting the results, since they are located upstream of where tests for transversal flow homogeneity and component isotropy are performed.

The mean velocity of the experiment is chosen to approximately match the Taylor-scale Reynolds number for the different fractal grids. At the reference location of $x/M = 20$, a Taylor-scale based Reynolds number of about $Re_\lambda \approx 300$ is targeted. Due to differing solidities of the various grids, this implies different mean velocities. For the passive grids, the turbulence intensity is systematically lower but the mean velocity could, typically, not be increased above a threshold due to winglet fragility. Thus, for the static grid, the target Reynolds number is about $Re_\lambda \approx 200$.

3.3 Flow Characteristics

3.3.1 Homogeneity and Component Isotropy

Transverse profiles of mean and root-mean-square (*r.m.s.*) velocities are obtained behind each grid, at a downstream distance of $14M$. Figure 3.6 shows profiles of the mean and *r.m.s.* velocity of the streamwise (u) and transverse (v) velocity components, taken both in the horizontal (z) and vertical (y) directions. From here on, time-averaged mean velocities will be indicated using brackets, i.e. $\langle u \rangle$ and $\langle v \rangle$, whereas the *r.m.s.* values are indicated as u_{rms} and v_{rms}. These results are shown for the Sierpinski Triangle and Space Filling Square fractal active grids. One should note that all the *r.m.s.* velocity profiles presented are multiplied by a factor 5 for presentation purposes, i.e. so the same velocity scale can be used in the axes. The profiles corresponding to the Apollonian Packing Design and the non-fractal winglets are presented in the Figure 3.7, and as can be seen, the profiles are quite uniform in the central part of the test section.

The same tests were performed on the passive configuration of the different winglet designs, and the case of the passive grid with Space Filling Square fractal winglets required special consideration. With the winglets fixed to face the flow, both the horizontal and vertical profiles revealed a non-negligible mean velocity gradient at $x/M = 14$ (see Figure 3.8). In order to correct these non-homogeneous distributions, the winglet orientations were adjusted, by trial and error. Instead of being perfectly

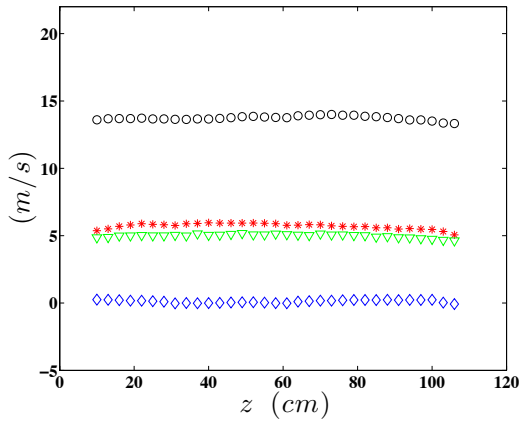

(A): Sierpinski Triangle: Horizontal Traverse

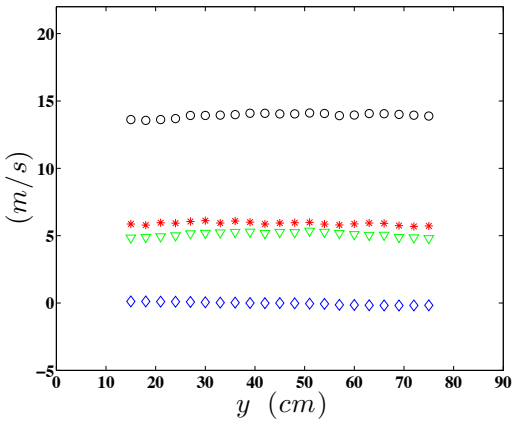

(B): Sierpinski Triangle: Vertical Traverse

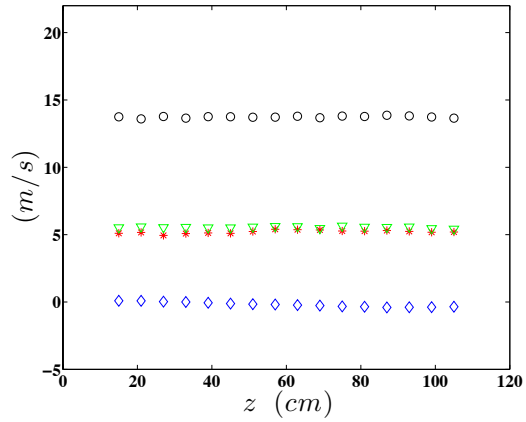

(C): Space Fill. Squares: Horizontal Traverse

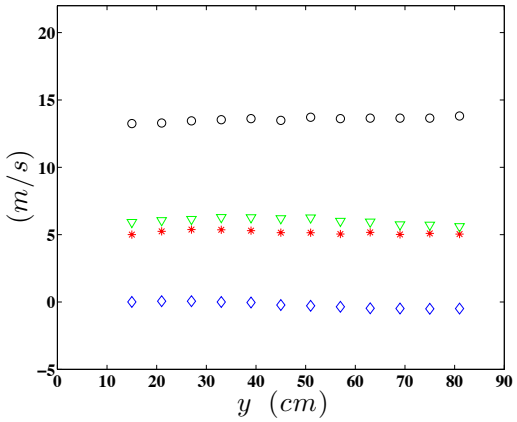

(D): Space Fill. Squares: Vertical Traverse

Figure 3.6: Profiles of mean and r.m.s. velocities at $x/M = 14$ downstream for Sierpinski Triangle and Space Filling Fractal active grids. $\circ$: $\langle u \rangle$, $\diamond$: $\langle v \rangle$, $*$: $5u_{\rm rms}$ $\bigtriangledown$: $5v_{\rm rms}$.

perpendicular to the flow, some have been angled. On the vertical rods, the angles for the seven sets of winglets were (from one side to another) -30, -40, 0, -30, 0, 40, and 50 degrees. On the horizontal rods, the angles for the five sets of winglets were 0, 0, -20, -20, and -20 degrees. The resulting profiles (black circles in Fig. 3.8) displayed good spatial homogeneity. It is possible that this is due to the space-filling nature of this type of fractal: after all if iterated to an infinite number of generations, for

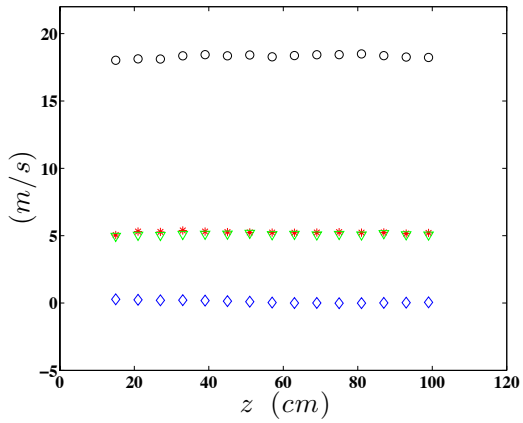

(A): Apollonian: Horizontal Traverse

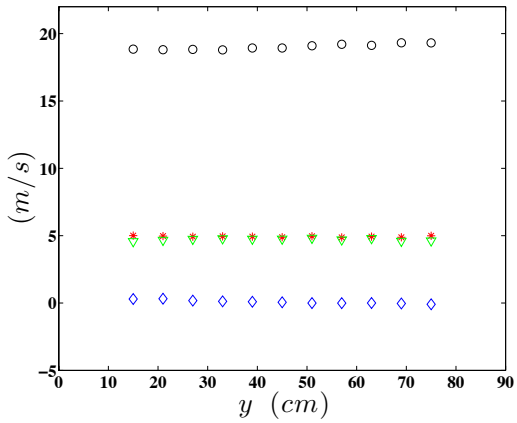

(B): Apollonian: Vertical Traverse

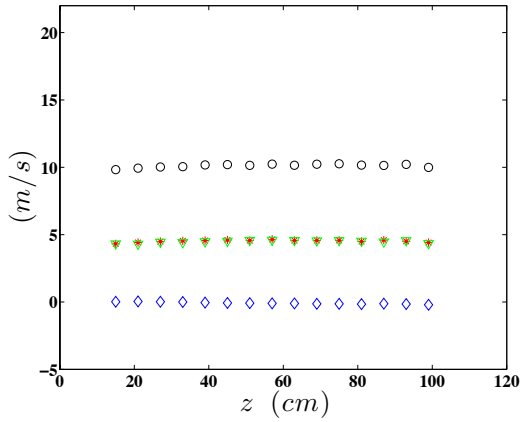

(C): Non-Fractal: Horizontal Traverse

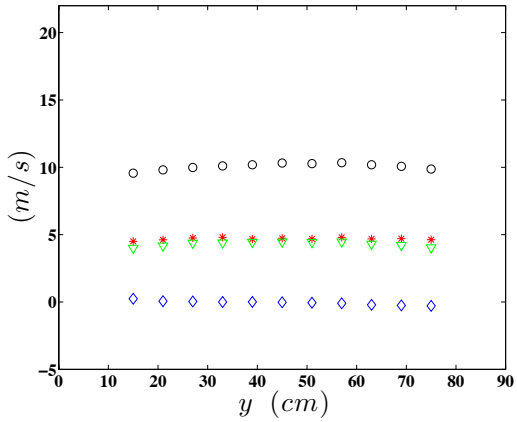

(D): Non-Fractal: Vertical Traverse

Figure 3.7: Profiles of mean and r.m.s. velocities at $x/M = 14$ for the Apollonian and Non-Fractal active grids.
$\circ$: $\langle u \rangle$, $\diamond$: $\langle v \rangle$, $*$: $5u_{\mathrm{rms}}$, $\bigtriangledown$: $5v_{\mathrm{rms}}$

this fractal the surface would be entirely blocked (solidity = 1). For the passive case, the winglets are oriented to fully block the cross-section. This does not occur for the active grid case in which additional time-dependent openings occur. This correction for the passive mode was successful and produced a nearly shear-less profile in the core region, both across the horizontal and vertical direction.

Figures 3.9 & 3.10 present results from tests performed for the four passive grids at $x/M = 14$. As for the active grids, the flow has no mean shear at the location of the measurements.

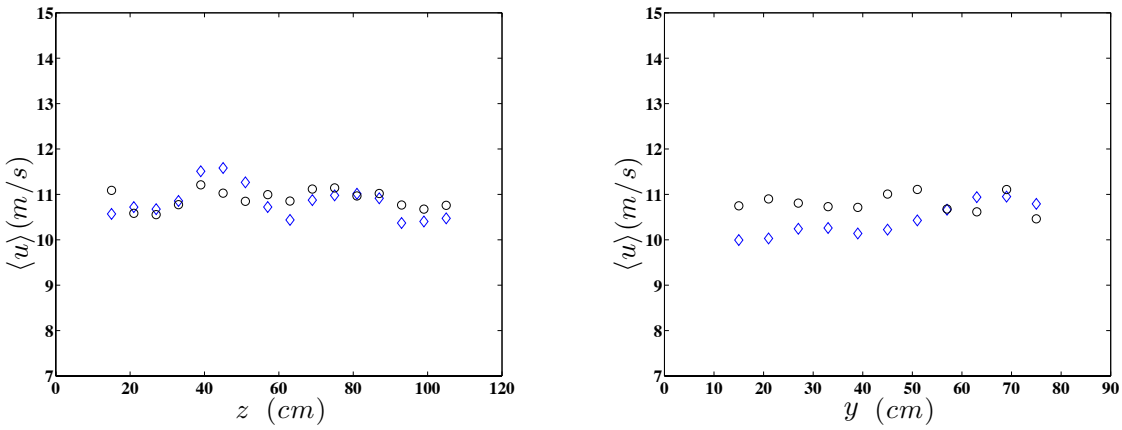

(A): Horizontal Traverse (B): Vertical Traverse

Figure 3.8: Horizontal and vertical profiles for the case of passive Space Filling square grid, before ($\diamond$), and after the correction ($\circ$). The original mean shear induced by the grid is corrected by changing the angle of attack of the winglets

To quantify spatial variability in these profiles, the standard deviations of $\langle u \rangle$, $\langle v \rangle$, u_{rms}, and v_{rms}, around their respective spatial mean values across the profiles are documented in Table 3.2, for the horizontal and vertical traverses. Spatial standard deviations are denoted as σ. Table 3.2 also contains the deviations of these profiles in percentage, computed in the core region of the tunnel (from 0.4m to 0.8m in the horizontal direction, and from 0.3m to 0.7m in the vertical direction) by taking the difference between the highest and the lowest values in that range, and dividing by the respective means. They are quite small in all of the four cases and we can conclude that the mean shear is negligible and the flow is nearly homogeneous. It implies that

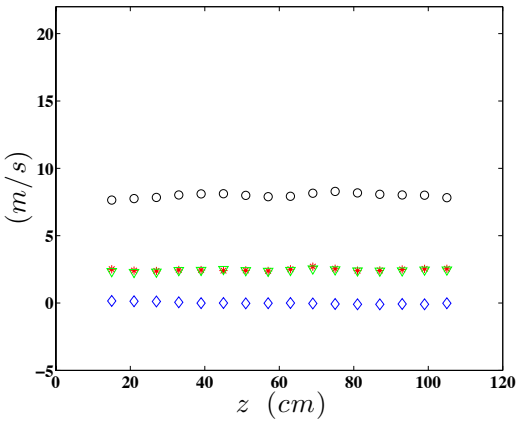

(A): Sierpinski: Horizontal Traverse

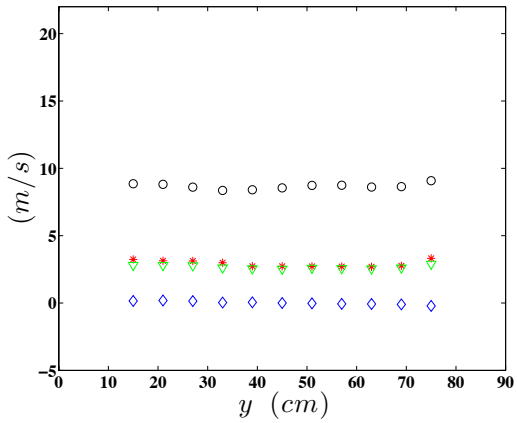

(B): Sierpinski: Vertical Traverse

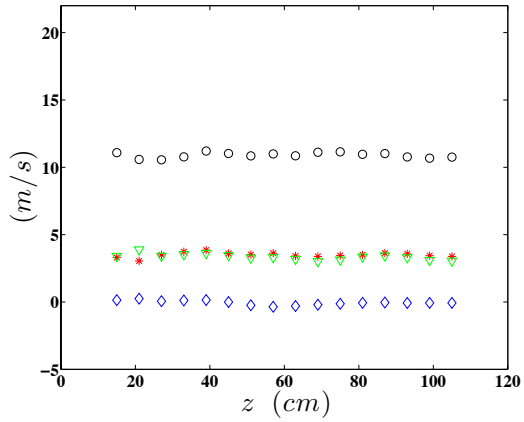

(C): Space Fill. Squares: Horizontal Traverse

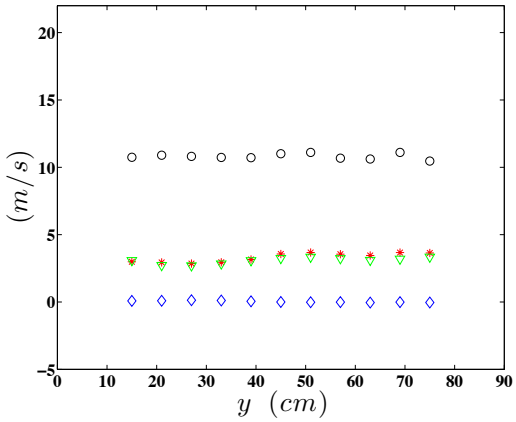

(D): Space Fill. Squares: Vertical Traverse

Figure 3.9: Profiles of mean and r.m.s. velocities at $x/M = 14$ for the Sierpinski and Space Filling square passive grids.
$\circ$: $\langle u \rangle$, $\diamond$: $\langle v \rangle$, $*$: $5u_{\rm rms}$, $\bigtriangledown$: $5v_{\rm rms}$

the downstream evolution of the turbulent kinetic energy occurs, essentially, due to dissipation only. However, since some component anisotropy is present (except for the case of the Apollonian Packing in which component anisotropy is quite small), for individual component variances $u^2_{\rm rms}$ and $v^2_{\rm rms}$, some of the evolution may be affected by pressure-strain correlations. Pressure-strain correlations should have no effect on the total kinetic energy $k = \frac{1}{2}(u^2_{\rm rms} + 2\ v^2_{\rm rms})$, however.

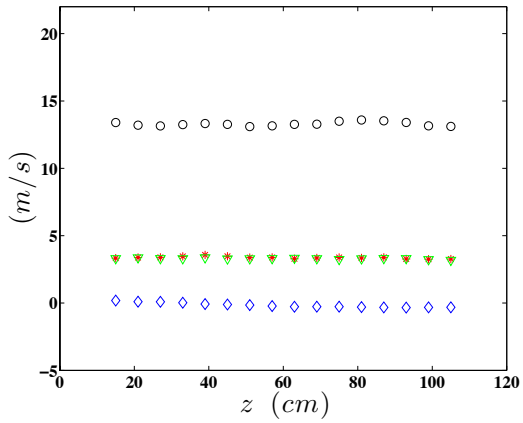

(A): Apollonian: Horizontal Traverse

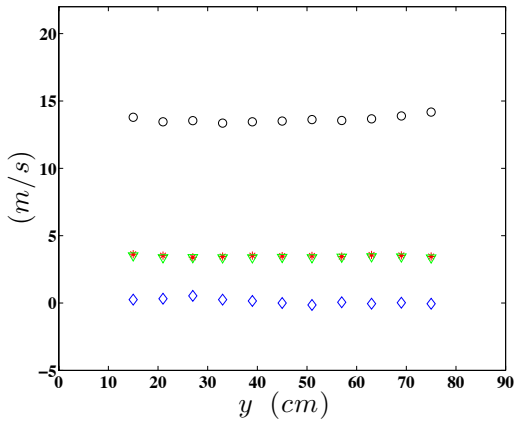

(B): Apollonian: Vertical Traverse

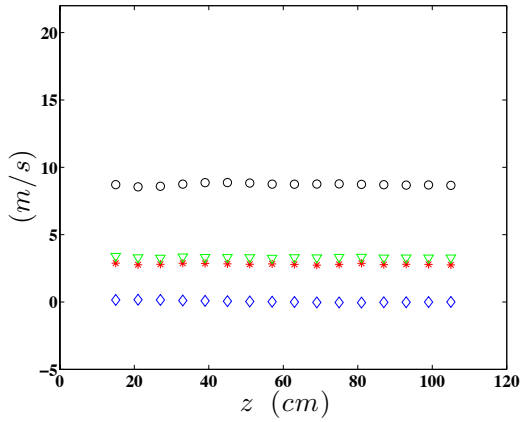

(C): Non-Fractal: Horizontal Traverse

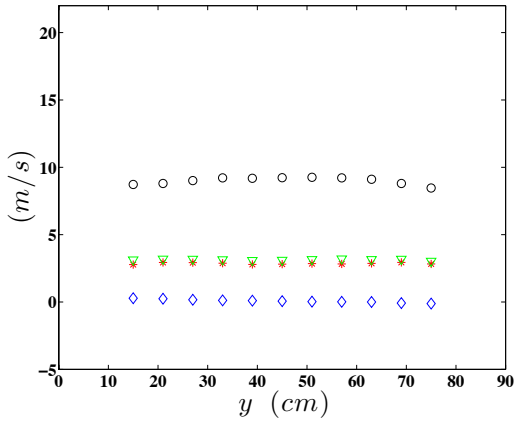

(D): Non-Fractal: Vertical Traverse

Figure 3.10: Profiles of mean and r.m.s. velocities at $x/M = 14$ for the Apollonian and Non-Fractal passive grids.
$\circ$: $\langle u \rangle$, $\diamond$: $\langle v \rangle$, $*$: $5u_{\mathrm{rms}}$, $\bigtriangledown$: $5v_{\mathrm{rms}}$

The isotropy ratios, quantified by the ratio of *r.m.s.* $I = u_{\mathrm{rms}}/v_{\mathrm{rms}}$ are presented in Figure 3.11 as function of x/M. Many previous active grids measurements[15,33] have shown isotropy ratios greater than 1. This is also observed for all present grids, except for the Space Filling Square winglets, whose isotropy ratio is $I \approx 0.77$. It is notable that the normal stresses produced by this grid configuration are larger

Table 3.2: Spatial r.m.s of profiles mean velocity and velocity temporal r.m.s., across horizontal and vertical direction for the the four active grids at $x/M = 14$.

	Horizontal Traverse			
	Sierpinski	Space Filling	Apollonian	Non-Fractal
$\sigma\left(\langle u\rangle\right) \quad (m/s)$	0.15	0.06	0.13	0.12
$\sigma\left(\langle v\rangle\right) \quad (m/s)$	0.10	0.10	0.04	0.02
$\sigma\left(u_{\mathrm{rms}}\right) \quad (m/s)$	0.04	0.02	0.015	0.01
$\sigma\left(v_{\mathrm{rms}}\right) \quad (m/s)$	0.02	0.01	0.01	0.01
$\delta\left\langle u\right\rangle / \langle\bar{u}\rangle\vert_{0.4-0.8\mathrm{m}} \quad (\%)$	2.5	0.9	1.1	1.1
$\delta\left(u_{\mathrm{rms}}\right) / \left\langle u_{\mathrm{rms}}\right\rangle \vert_{0.3-0.7\mathrm{m}} \quad (\%)$	4.9	5.7	1.6	3.5
$\delta\left(v_{\mathrm{rms}}\right) / \left\langle v_{\mathrm{rms}}\right\rangle \vert_{0.3-0.7\mathrm{m}} \quad (\%)$	3.0	3.2	2.4	2.3
	Vertical Traverse			
	Sierpinski	Space Filling	Apollonian	Non-Fractal
$\sigma\left(\langle u\rangle\right) \quad (m/s)$	0.16	0.20	0.20	0.24
$\sigma\left(\langle v\rangle\right) \quad (m/s)$	0.10	0.06	0.13	0.25
$\sigma\left(u_{\mathrm{rms}}\right) \quad (m/s)$	0.02	0.02	0.008	0.017
$\sigma\left(v_{\mathrm{rms}}\right) \quad (m/s)$	0.03	0.03	0.17	0.03
$\delta\left\langle u\right\rangle / \langle\bar{u}\rangle\vert_{0.4-0.8\mathrm{m}} \quad (\%)$	1.3	1.6	2.8	2.7
$\delta\left(u_{\mathrm{rms}}\right) / \left\langle u_{\mathrm{rms}}\right\rangle \vert_{0.3-0.7\mathrm{m}} \quad (\%)$	6.2	6.7	1.7	2.7
$\delta\left(v_{\mathrm{rms}}\right) / \left\langle v_{\mathrm{rms}}\right\rangle \vert_{0.3-0.7\mathrm{m}} \quad (\%)$	9.0	8.9	4.7	6.0

in the lateral than in the axial direction. Finally, it is noted that the case of the Apollonian Packing shows an excellent level of component isotropy. Next, the same characterizations are performed for the passive grids, and the results are presented in Figure 3.12. As for the active grid cases, small levels of spatial variance, i.e. good spatial transverse homogeneity, are found for all cases

All the results presented bellow will be restricted to the data acquired downstream of $x/M = 14$ (starting at $x/M = 15$) in order to avoid any possible inhomogeneous regions. In all, 14 different downstream distances ranging from $x/M = 15$ to $x/M = 50$ will be considered.

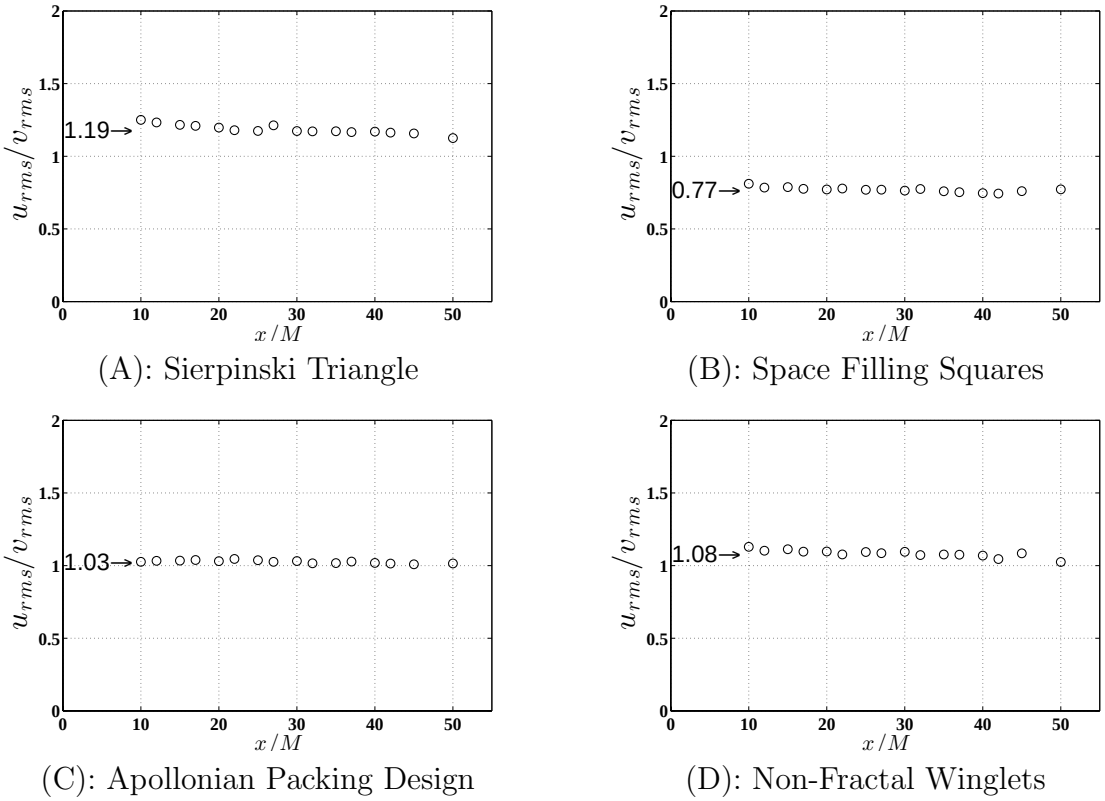

(A): Sierpinski Triangle (B): Space Filling Squares

(C): Apollonian Packing Design (D): Non-Fractal Winglets

Figure 3.11: Isotropy Ratios $I = u_{\rm rms}/v_{\rm rms}$ for the four types of active grids

3.3.2 Flow Parameters

Tables 3.3 & 3.4 present the major flow parameters measured as a reference at location $x/M = 20$ for the active and passive cases, respectively. Taylor's hypothesis is used to compute spatial quantities from the measured temporal signals. The tables show the streamwise mean velocity and the *r.m.s.* of the two measured fluctuating velocity components. Also shown is ϵ, the molecular dissipation rate computed directly from the decay of kinetic energy $k = \frac{1}{2}(u_{\rm rms}^2 + 2v_{\rm rms}^2)$. As will be shown based on the actual data, power-law decay is evident. Therefore, to determine the value of ϵ we fit a power-law to the kinetic energy decay and evaluate the derivative. Specifically,

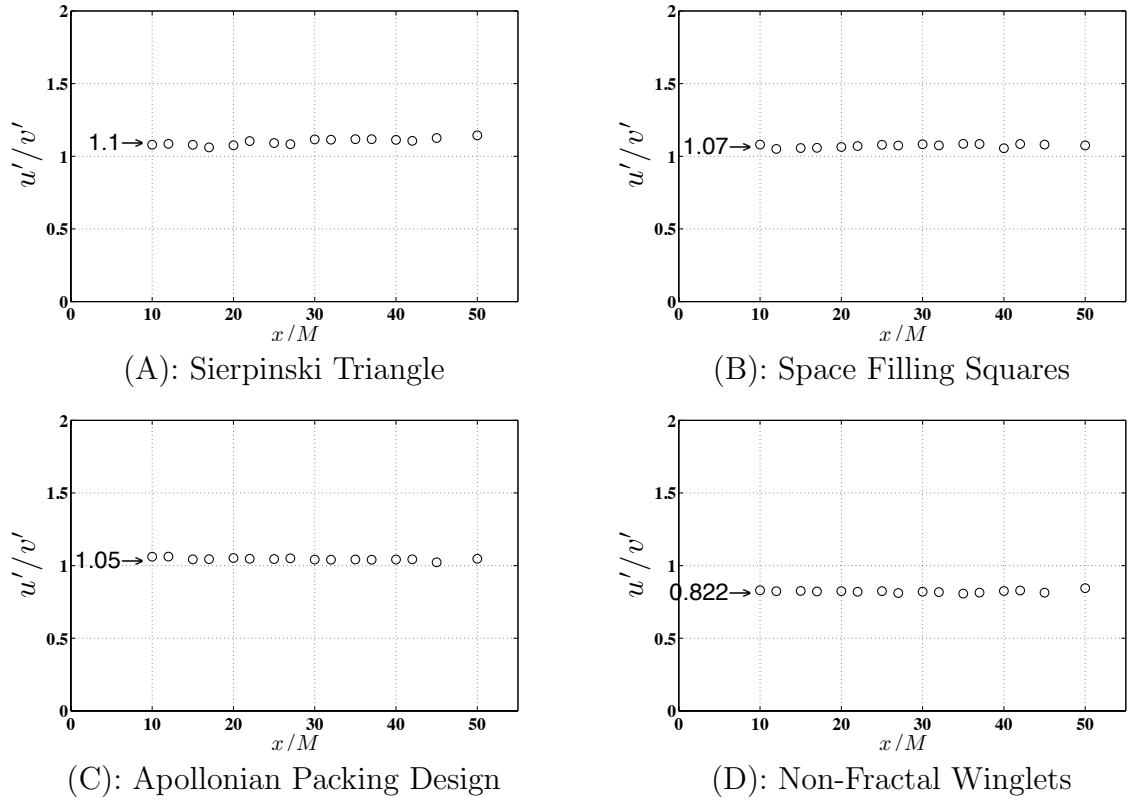

(A): Sierpinski Triangle (B): Space Filling Squares

(C): Apollonian Packing Design (D): Non-Fractal Winglets

Figure 3.12: Isotropy Ratios $I = u_{\rm rms}/v_{\rm rms}$ for the four types of passive grids

we use:

$$\epsilon_{\rm decay} \;=\; -\frac{dk}{dt} = -\langle u\rangle\frac{dk}{dx} = -\langle u\rangle\frac{d}{dx}\left[A\langle u\rangle^2\left(\frac{x-x_0}{M}\right)^{-n}\right] = nA\frac{\langle u\rangle^3}{M}\left(\frac{x-x_0}{M}\right)^{-n-1} \quad (3.1)$$

where A and n, the kinetic energy decay exponent, are obtained through fitting the data as presented in section 4.4. When a value of ϵ is quoted, unless indicated otherwise, it will have been obtained from the decay measurement, i.e. $\epsilon = \epsilon_{\rm decay}$ henceforth. Quoted values include as error bars ($\pm$) the uncertainty in determining $\epsilon_{\rm decay}$. The relative uncertainty in $\epsilon_{\rm decay}$ arises only due to uncertainties of the fitted

value of decay exponent n as well as uncertainties in the mean velocity, according to

$$\epsilon = nA\frac{\langle u\rangle^3}{M}\left(\frac{x-x_0}{M}\right)^{-n-1} \Rightarrow \frac{\delta\epsilon}{\epsilon} = \left\{\left(\frac{\delta n}{n}\left[1 - n\log\left(\frac{x-x_0}{M}\right)\right]\right)^2 + \left(3\frac{\delta u}{u}\right)^2\right\}^{1/2} \quad (3.2)$$

The relative uncertainty in the exponent, $\delta n/n$, is determined in the next section from considerations of how the fitting is performed. The relative uncertainty in measuring the velocity between the prior and post calibrations is quite small, leading to $\delta u/u \approx 2\%$.

Also shown in Tables 3.3 & 3.4 are three estimates of the integral scale: first, the value $\ell_\epsilon = 0.9u_{\rm rms}^3/\epsilon_{\rm decay}$, as used in Mydlarsky & Warhaft[34] is shown. The value ℓ_f as measured from the integral of the longitudinal correlation function is shown later in this work, where it is evaluated by integrating the correlation functions only to the first zero crossing, obtaining ℓ_{fc} (which tends to be larger than ℓ_f due to omitted contributions from negative lobes in the correlation function - see Chapter 3.4.4 for more details).

Tables 3.3 & 3.4 also list the Kolmogorov scale $\eta = (\nu^3/\epsilon_{\rm decay})^{1/4}$, the Taylor microscale $(15\nu u_{\rm rms}^2/\epsilon_{\rm decay})^{1/2}$, and the Reynolds number based on the latter, $Re_\lambda = \lambda u_{\rm rms}/\nu$. The corresponding error bars are determined based on the sensitivity analysis for $\epsilon_{\rm decay}$ appropriately propagated to the Taylor scale λ, and to Re_λ

in a similar manner:

$$\frac{\delta\lambda}{\lambda} = \left[\left(-\frac{1}{2}\frac{\delta\epsilon}{\epsilon}\right)^2 + \left(\frac{\delta u}{u}\right)^2\right]^{1/2} \Rightarrow \frac{\delta Re_\lambda}{Re_\lambda} = \left[\left(\frac{\delta\lambda}{\lambda}\right)^2 + \left(\frac{\delta u}{u}\right)^2\right]^{1/2} \tag{3.3}$$

Table 3.3: Parameters of the flow generated by the four different active grids at $x/M = 20$

	Sierpinski	Space Filling	Apollonian	Non-Fractal
$\langle u \rangle$ (m/s)	12.9	13.2	21.2	9.59
u_{rms} (m/s)	0.83	0.82	0.89	0.72
v_{rms} (m/s)	0.69	1.1	0.87	0.65
$\epsilon_{\mathrm{decay}}$ (m^2/s^3)	4.86 ± 0.45	5.02 ± 0.38	11.0 ± 0.71	2.56 ± 0.32
$\ell_\epsilon = 0.9\ u_{\mathrm{rms}}^3/\epsilon_{\mathrm{decay}}$ (m)	0.106	0.100	0.058	0.128
ℓ_f (m)	0.082	0.072	0.057	0.147
ℓ_{fc} (m)	0.134	0.116	0.082	0.126
η (mm)	0.168 ± 0.005	0.166 ± 0.005	0.137 ± 0.004	0.197 ± 0.007
λ (mm)	5.78 ± 0.29	5.63 ± 0.24	4.12 ± 0.16	6.85 ± 0.45
$Re_\lambda = \frac{u'\lambda}{\nu}$	306 ± 17	295 ± 14	234 ± 10	312 ± 21

Table 3.4: Parameters of the flow generated by the four different passive grids at $x/M = 20$

	Sierpinski	Space Filling	Apollonian	Non-Fractal
$\langle u \rangle$ (m/s)	8.71	11.3	13.8	9.02
u_{rms} (m/s)	0.42	0.52	0.51	0.41
v_{rms} (m/s)	0.39	0.49	0.49	0.49
$\epsilon_{\mathrm{decay}}$ (m^2/s^3)	1.00 ± 0.08	2.14 ± 0.16	2.74 ± 0.20	1.06 ± 0.08
$\ell_\epsilon = 0.9\ u_{rmrms}^3/\epsilon_{\mathrm{decay}}$ (m)	0.066	0.059	0.044	0.057
ℓ_f (m)	0.054	0.051	0.049	0.052
ℓ_{fc} (m)	0.058	0.055	0.056	0.058
η (mm)	0.250 ± 0.007	0.206 ± 0.006	0.194 ± 0.005	0.245 ± 0.007
λ (mm)	6.43 ± 0.28	5.44 ± 0.28	4.72 ± 0.19	6.06 ± 0.25
$Re_\lambda = \frac{u'\lambda}{\nu}$	171 ± 8	180 ± 8	154 ± 7	157 ± 7

3.4 Results and Discussions

3.4.1 The energy decay rate

The decay of streamwise variance and kinetic energy behind the fractal and non-fractal grids presented in section 3.2.2 is considered by comparing the experimental data to power laws of the form:

$$\frac{\langle u'^2\rangle}{\langle u\rangle^2} \equiv A_u \left(\frac{x - x_{0u}}{M}\right)^{-n_u}, \qquad \frac{k}{\langle u\rangle^2} \equiv A_k \left(\frac{x - x_{0k}}{M}\right)^{-n_k}, \tag{3.4}$$

where, as before, the kinetic energy is deduced from the two measured components assuming spanwise isotropy (axisymmetry), $k = \frac{1}{2}(\langle u'^2\rangle + 2\langle v'^2\rangle)$. As a caveat we remark that there exist observations[62] in grid turbulence in which $v_{\rm rms} \neq w_{\rm rms}$. But given the symmetry of our grid it would appear reasonable to expect $v_{\rm rms} \approx w_{\rm rms}$.

First we consider the power-law without specifying any virtual origin, i.e. we set $x_{0u} = x_{0k} = 0$ and the downstream distance x is measured from the physical grid location. Figures 3.13 (A) and (B) show log-log plots of $\langle u'^2\rangle/\langle u\rangle^2$ and $k/\langle u\rangle^2$, respectively, for the four active grid experiments. The data shows good agreement with a power-law decay behavior for all four active grids. Solid lines indicate a least-squares error fit (in log-log axes) by using the following linear relation

$$\ln\left(\frac{\langle u'^2\rangle}{\langle u\rangle^2}\right) = \ln\left(A_u\right) - n_u \ln\left(\frac{x - x_{0u}}{M}\right), \tag{3.5}$$

and similarly for k.

To report the experimental uncertainty for the measured decay exponents n_u and n_k, we proceed as follows. The error bars associated with each decay exponent are obtained in a 95% (2σ) confidence intervals[63] ('REGRESS' routine in MatLab^{TM}) after applying the logarithmic transformation. We find that visually this quantification of uncertainty to be consistent with the data and its general behavior.

The first part of Table 3.5 contains the different decay exponents obtained by fitting the data with no virtual origin. The range of decay exponents obtained, $1.08 \leq n_u \leq 1.28$, is in reasonable agreement with the ones reported by Krogstad & Davidson,[16] certainly within the quoted level of uncertainty. The same analysis is performed for k, and shown in Figures 3.13 (B). Table 3.5 also contains the measured exponents, yielding values in the range $1.03 \leq n_k \leq 1.24$ quite close to the range observed for n_u.

Similarly, the analysis is repeated for the four passive grid cases. As can be seen in Figures 3.13 (C) and (D) the decays exhibit power-law behaviors, and exponents occur in a range of approximately $1.22 \leq n_u \leq 1.47$ for the longitudinal (u) velocity, and about $1.28 \leq n_k \leq 1.46$ for the kinetic energy, when no virtual offset, x_0/M, is taken into consideration. The energy measured seems to decay faster when the grid is static than when no virtual origin is used. As explained in section 3.4.2, and often cautioned in prior works,[13] results can be affected rather strongly depending upon the virtual origin x_0/M.

Table 3.5: Decay rate exponents (n), pre-factors (A) and r.m.s. of data about the fitted power-law (σ_{fit}), obtained with the four active grids.

Without a virtual origin				
Component: $\langle u'^2 \rangle$	Sierpinski	Space Filling	Apollonian	Non-Fractal
n_u	1.11 ± 0.032	1.12 ± 0.026	1.28 ± 0.028	1.08 ± 0.021
x_0/M	0	0	0	0
A_u	0.115	0.111	0.081	0.144
σ_{fit}	0.0188	0.0156	0.0168	0.0125
$k = \frac{1}{2}(\langle u'^2 \rangle + 2\langle v' \rangle^2)$	Sierpinski	Space Filling	Apollonian	Non-Fractal
n_k	1.05 ± 0.029	1.07 ± 0.020	1.24 ± 0.032	1.03 ± 0.017
x_0/M	0	0	0	0
A_u	0.116	0.208	0.106	0.163
σ_{fit}	0.0171	0.0122	0.0189	0.0102

With a virtual origin				
Component: $\langle u'^2 \rangle$	Sierpinski	Space Filling	Apollonian	Non-Fractal
n_u	1.15 ± 0.032	1.03 ± 0.023	1.08 ± 0.013	1.21 ± 0.021
x_0/M	-1	2	4	-3
A_u	0.138	0.077	0.035	0.246
σ_{fit}	0.0185	0.0149	0.0091	0.0110
$k = \frac{1}{2}(\langle u'^2 \rangle + 2\langle v'^2 \rangle)$	Sierpinski	Space Filling	Apollonian	Non-Fractal
n_k	1.05 ± 0.029	1.07 ± 0.021	1.00 ± 0.010	1.07 ± 0.017
x_0/M	0	0	5	-1
A_u	0.116	0.208	0.038	0.193
σ_{fit}	0.0171	0.0122	0.0073	0.0099

3.4.2 The effects of a virtual origin

The determination of the virtual origins x_{0u}/M and x_{0k}/M is done by finding the virtual origin that leads to smallest σ_{fit}. Fits using various values of the virtual origin x_{0u}/M are tested for the decay of $\langle u'^2 \rangle$. For simplicity only integer values of x_{0u}/M are tested. As shown in Figure 3.14 for both the active and passive cases for the

Table 3.6: Decay rate exponents (n), pre-factors (A) and r.m.s. of data about the fitted power-law (σ_{fit}), obtained with the four passive grid configurations.

Without a virtual origin				
Component: $\langle u'^2 \rangle$	Sierpinski	Space Filling	Apollonian	Non-Fractal
n_u	1.22 ± 0.034	1.35 ± 0.031	1.47 ± 0.032	1.33 ± 0.072
x_0/M	0	0	0	0
A_u	0.090	0.122	0.112	0.109
σ_{fit}	0.0202	0.0184	0.0188	0.0426
$k = \frac{1}{2}(\langle u'^2 \rangle + 2\langle v'^2 \rangle)$	Sierpinski	Space Filling	Apollonian	Non-Fractal
n_k	1.28 ± 0.024	1.37 ± 0.032	1.46 ± 0.030	1.33 ± 0.051
x_0/M	0	0	0	0
A_u	0.146	0.178	0.153	0.219
σ_{fit}	0.0144	0.0190	0.0182	0.0303

With a virtual origin				
Component: $\langle u'^2 \rangle$	Sierpinski	Space Filling	Apollonian	Non-Fractal
n_u	1.08 ± 0.025	1.19 ± 0.021	1.30 ± 0.018	0.97 ± 0.028
x_0/M	3	3	3	7
A_u	0.049	0.063	0.054	0.024
σ_{fit}	0.0172	0.0140	0.0126	0.0230
$k = \frac{1}{2}(\langle u'^2 \rangle + 2\langle v'^2 \rangle)$	Sierpinski	Space Filling	Apollonian	Non-Fractal
n_k	1.13 ± 0.016	1.16 ± 0.012	1.24 ± 0.012	1.02 ± 0.015
x_0/M	3	4	4	6
A_u	0.078	0.073	0.059	0.059
σ_{fit}	0.0110	0.0085	0.0087	0.0116

Sierpinski triangle grid, the exponent resulting from the fit depends rather strongly upon the choice of virtual origin, but the optimal values chosen can be considered "best" within the range of uncertainty already documented based on σ_{fit} as described before.

Figures 3.15 display the streamwise variance and kinetic energy decay, now including the best virtual origin. The prior classical decays rates n = 10/7, n = 6/5 and n

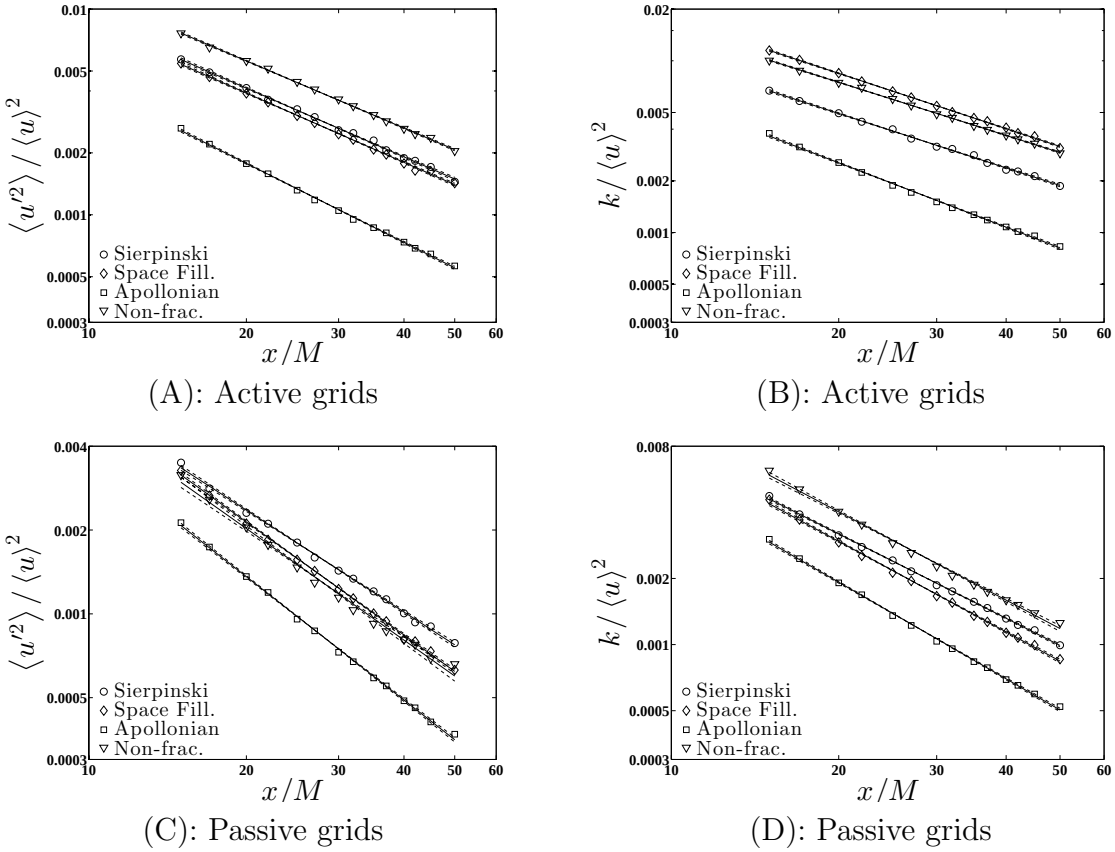

(A): Active grids (B): Active grids

(C): Passive grids (D): Passive grids

Figure 3.13: Decay of streamwise velocity variance and turbulent kinetic energy for the four different active and passive grid configurations, using a virtual origin $x_{0u} = x_{0k} = 0$. The corresponding fitted exponents and their associated errors are listed in table 3.6.

= 1, are also presented on Figure 3.15 (C) for comparison purposes. In the presence of a virtual origin, the fits become marginally better (the data fall more clearly onto a linear behavior rather than being slightly curved thus leading to the smaller σ_{fit}). Tables 3.5, & 3.6 show the decay exponents, which compared to the $x_{0u} = 0$ fits are slightly smaller, i.e. $1.03 \leq n_u \leq 1.17$. We remark that the obtained x_0 do not appear to offer insights on a possible trend nor any explanation of the effect of grid geometry on the flow.

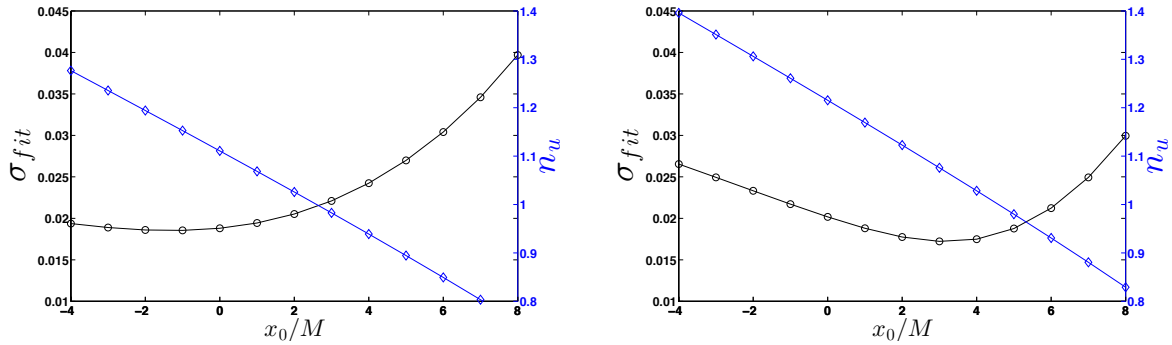

(A): Active grids (B): Passive grids

Figure 3.14: Root-mean-square σ_{fit} (circles, left axis) and fitted decay exponent n_u(diamonds, right axis) as function of virtual origin x_{0u} for the Sierpinski grids.

The same analysis is performed for the cases of the passive grid. Interestingly, a more consistent trend is observed as far as virtual origin is concerned: we obtain $x_{0u}/M = 3$ for all three fractal grids, and $x_{0u}/M = 7$ for the non-fractal grid. With the virtual origin included, the fitted decay exponent results somewhere lowered, to a range between $0.96 \leq n_u \leq 1.30$. Similar behaviors are observed for the decay of kinetic energy.

To convey clearly that the decay follows a power-law more convincingly than exponential decay, in Figure 3.16 we present the decay trends for the four active grid cases in semi-logarithmic axes. The solid lines shown are the power-law fits discussed before. In such plots, exponential decay would be linear, but clearly the decay is proceeding more slowly than exponential. We can confirm that in the measured region $x/M > 14$ the decay follows power-laws more closely than exponential. Similar results have also been observed by Krogstad and Davidson (2012).[17] We remark that at small x/M a short quasi-linear region could be fitted to the transition formula that

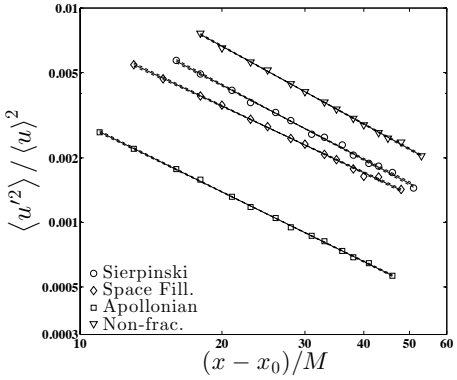

(A): Active grids, $x_0 \neq 0$.

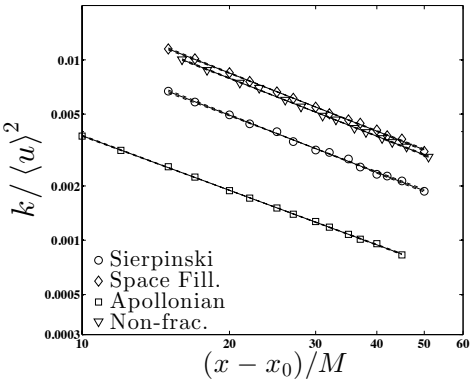

(B): Active grids, $x_0 \neq 0$.

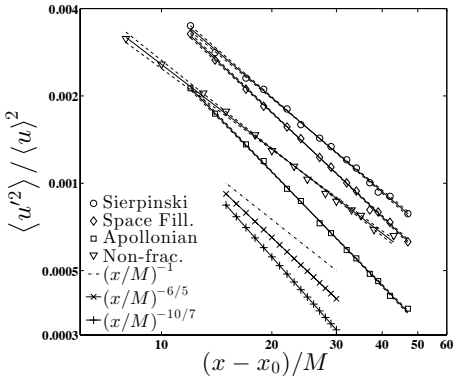

(C): Passive grids, $x_0 \neq 0$.

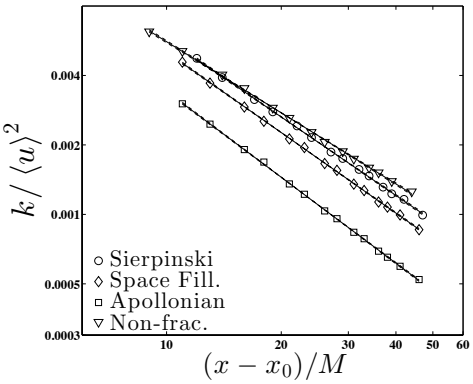

(D): Passive grids, $x_0 \neq 0$.

Figure 3.15: Kinetic energy rates of the four different active and passive grid configurations using a virtual origin $x_0 \neq 0$. The corresponding exponent values and their associated errors are listed in tables 3.5, &3.6.

connects any near-grid exponential to power-law behavior as proposed by Mazellier & Vassilicos,[28] but the focus here is on the data at $x/M > 15$ where the power-law is already established.

The downstream evolution of the Taylor-scale Reynolds number Re_λ is also of interest. The results are plotted on a logarithmic scale in Fig. 3.17. The active and passive grid cases behave in an expected manner. Since $Re_\lambda^2 \sim [(x - x_0)/M]^{1-n}$, Re_λ is approximately constant with downstream distance for the grid configurations

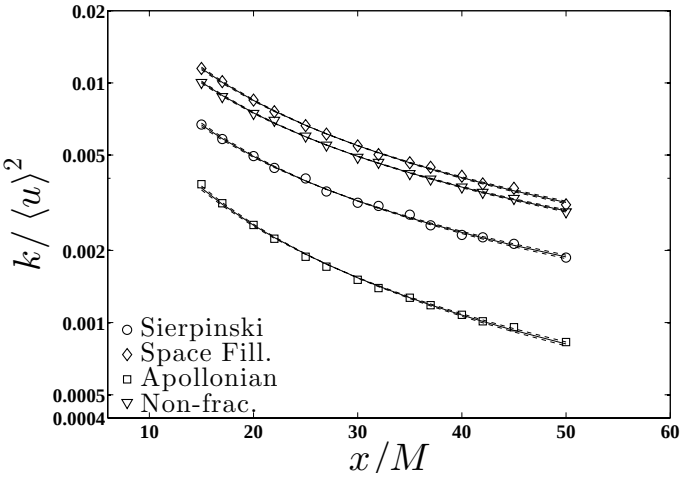

(A)

Figure 3.16: Semi-logarithmic plot of the kinetic energy rates of the four different active grid configuration using no virtual origin x_{0k}, as listed in Tables 3.5 and 3.6. If the decay were exponential, these curves would have to be straight lines.

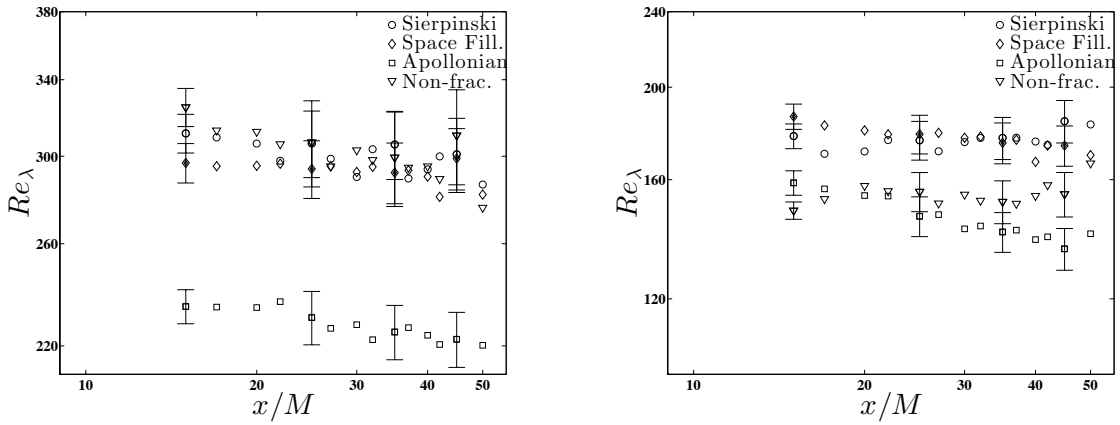

(A): Active grids (B): Passive grids

Figure 3.17: Re_λ as function of the downstream location x/M. The error bars are displayed every four points to avoid clutter

that produced decay exponents close to unity (after the implementation of a virtual origin), such as the Space Filling active and Non-Fractal passive grids.

3.4.3 Dependence of the decay exponent on grid geometries and flow properties

The results presented in the preceding section raise the question whether any particular trends can be established between the decay exponent and flow and grid parameters. This study covers particular ranges of Re_λ, turbulence intensity, grid blockage ratio, isotropy levels, and fractal dimensions for both the active and the passive grids. Figures 3.18 & 3.19 present the fitted decay exponents and their error bars, as function of these grid and flow parameters.

In viewing the general trends in Figures 3.18 & 3.19, one may distinguish an increasing trend of n with increasing blockage ratio, fractal dimension, and turbulence intensity for the active grids. Conversely, for the passive grids, it appears that the general trends are that n decreases with increasing fractal dimension, with blockage ratio and with turbulence intensity. The significant scatter and error bars in our results, however, preclude us from claiming that these trends are generally robust. For both active and passive grids, it appears that n is larger when the anisotropy ratio $u_{\rm rms}/v_{\rm rms}$ exceeds unity, whereas n is close to unity for the cases where $u_{\rm rms}/v_{\rm rms} < 1$. The lack of additional information prevents us from drawing any physical conclusions from this information, but we remark that Lavoie[64] also found that n increases with deviations from anisotropy. Any clear trends with Reynolds number are even more difficult to distinguish. We recall that George[10] and Burattini *et al.*[65] explored depen-

dencies of n with Re_λ and argued that the decay exponent tends to 1 for increasing Re_λ.

3.4.4 Correlation functions and integral scales

The longitudinal two-point correlation function is computed for each downstream location for the four different active grids according to its definition (using Taylor's hypothesis):

$$f(r) = \langle u'(x+r)u'(x)\rangle / \langle u'^2\rangle. \tag{3.6}$$

Results are shown in Fig. 4.10. It is interesting to note that the non-fractal grid does not show a negative lobe, and the negative lobe is very weak for the low-turbulence intensity Apollonian Packing grid. For the Sierpinsky and Space Filling Fractal cases, the negative lobes are more pronounced. However, these features do not seem to be correlated with the different flow parameters introduced in this study (fractal dimension, blockage ratio, isotropy ratio, turbulence intensity, and Reynolds number).

The longitudinal integral lengthscale is defined as

$$\ell_{fc} \;=\; \int_0^{r_c} f(r)\; dr \tag{3.7}$$

where r_c is the first zero crossing of $f(r)$. ℓ_{fc} is computed for the 14 downstream

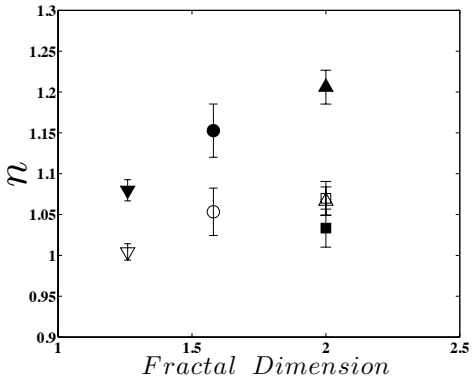

(A): n vs. fractal dimension of the agitators

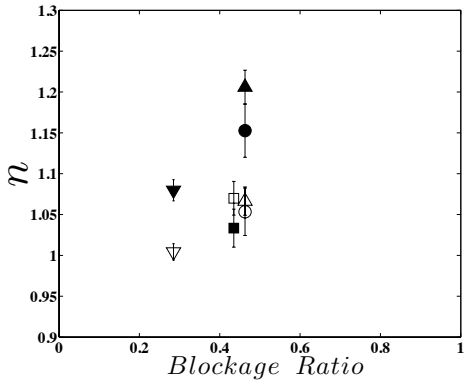

(B): n vs. blockage ratio

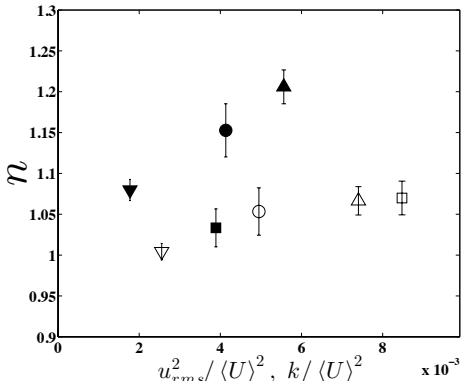

(C): n vs. $u^2_{\mathrm{rms}}/\langle u\rangle$ and $k/\langle u\rangle$

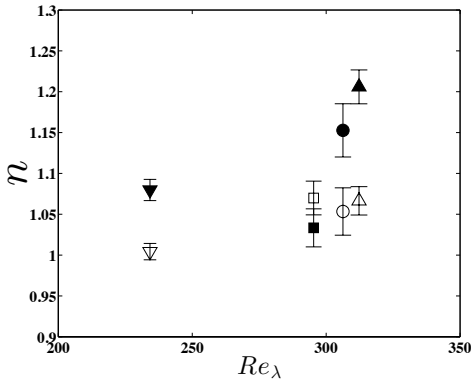

(D): n vs. Re_λ

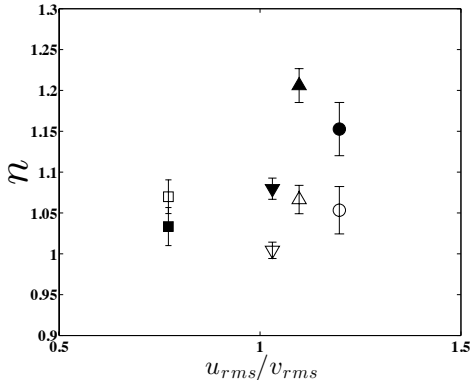

(E): n vs. $u_{\mathrm{rms}}/v_{\mathrm{rms}}$

Figure 3.18: Fitted decay exponents and their error bars of the four active grids, as function of the flow parameters recorded at x/M = 20: ◯: Sierpinski, □: Space Filling Squares, ▽: Apollonian Packing, △: Non-Fractal. Filled symbols: n_u; empty sympols: n_k.

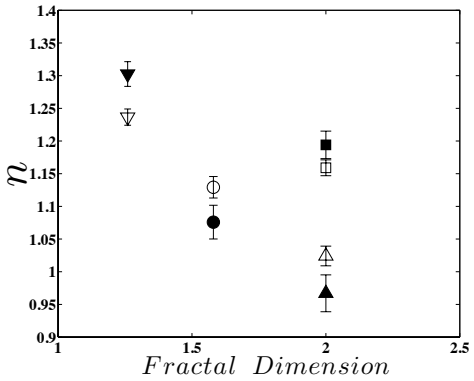

(A): n vs. fractal dimension of the agitators

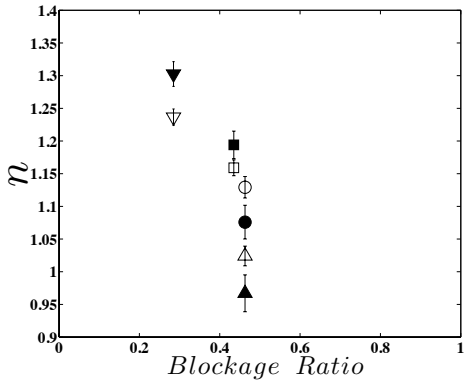

(B): n vs. blockage ratio

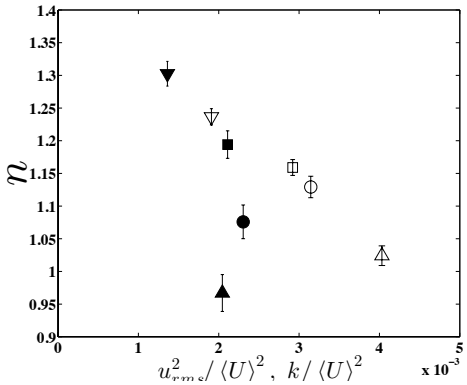

(C): n vs. $u^2_{\mathrm{rms}}/\langle u\rangle$ and $k/\langle u\rangle$

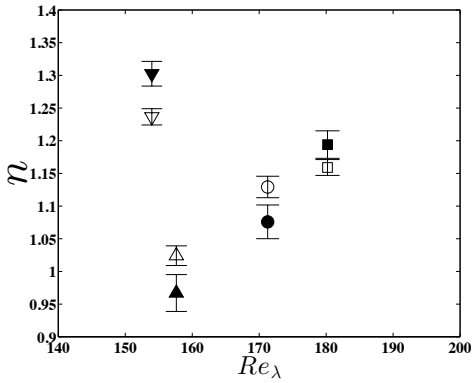

(D): n vs. Re_λ

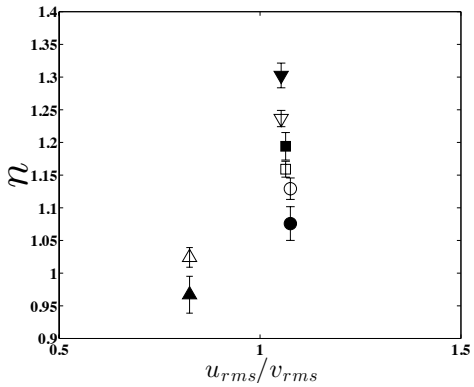

(E): n vs. $u_{\mathrm{rms}}/v_{\mathrm{rms}}$

Figure 3.19: Fitted decay exponents and their error bars of the four active grids, as function of the flow parameters recorded at x/M = 20: ◯: Sierpinski, □: Space Filling Squares, ▽: Apollonian Packing, △: Non-Fractal. Filled symbols: n_u; empty sympols: n_k.

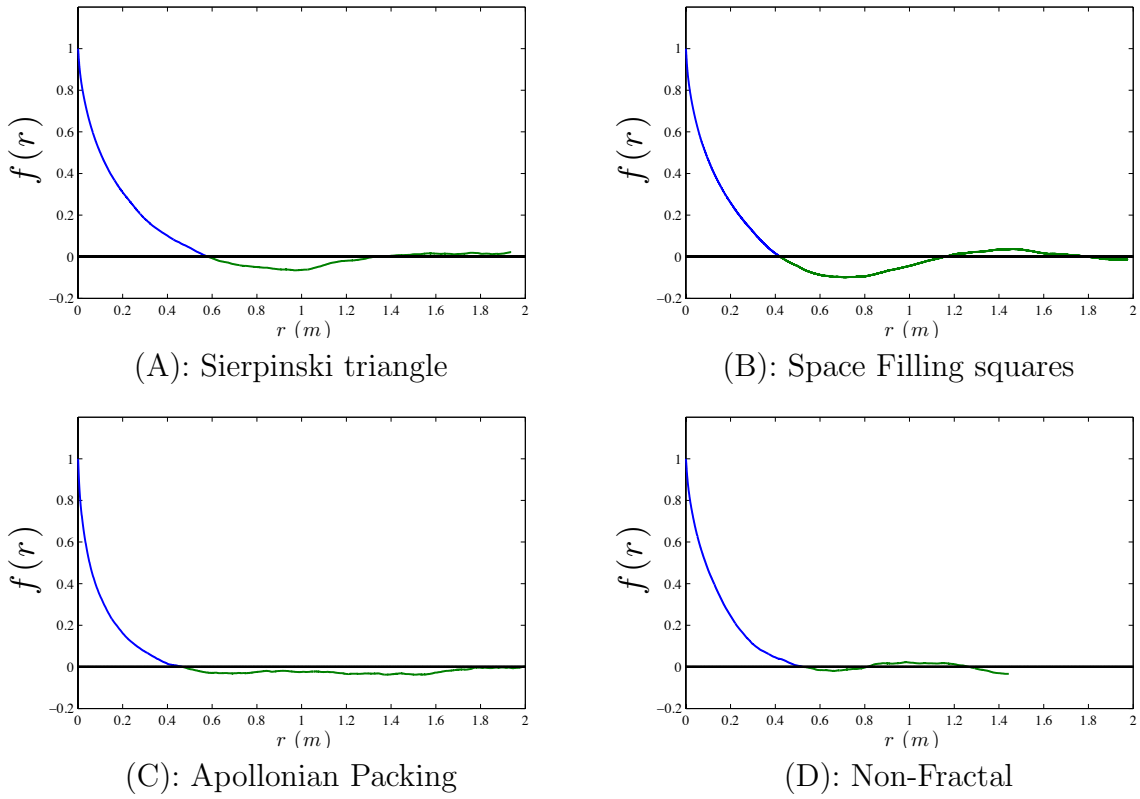

(A): Sierpinski triangle (B): Space Filling squares

(C): Apollonian Packing (D): Non-Fractal

Figure 3.20: Longitudinal correlation functions at $x/M = 30$ for the four active grids.

locations from the two-points correlation functions, for the active and passive grids. The analysis was also performed by integrating r over the entire available range of r in the measurements,

$$\ell_f = \int_0^{\infty} f(r)\, dr \approx \int_0^{r_{\max}} f(r)\, dr, \tag{3.8}$$

and the results are represented by the black line in Figs. 3.21 & 3.22. Specifically, Figure 3.21 presents the integral length scales computed from the longitudinal correlation function plotted versus the downstream location for each active grid. Similarly,

figure 3.22 presents the integral length scales computed for each passive grid.

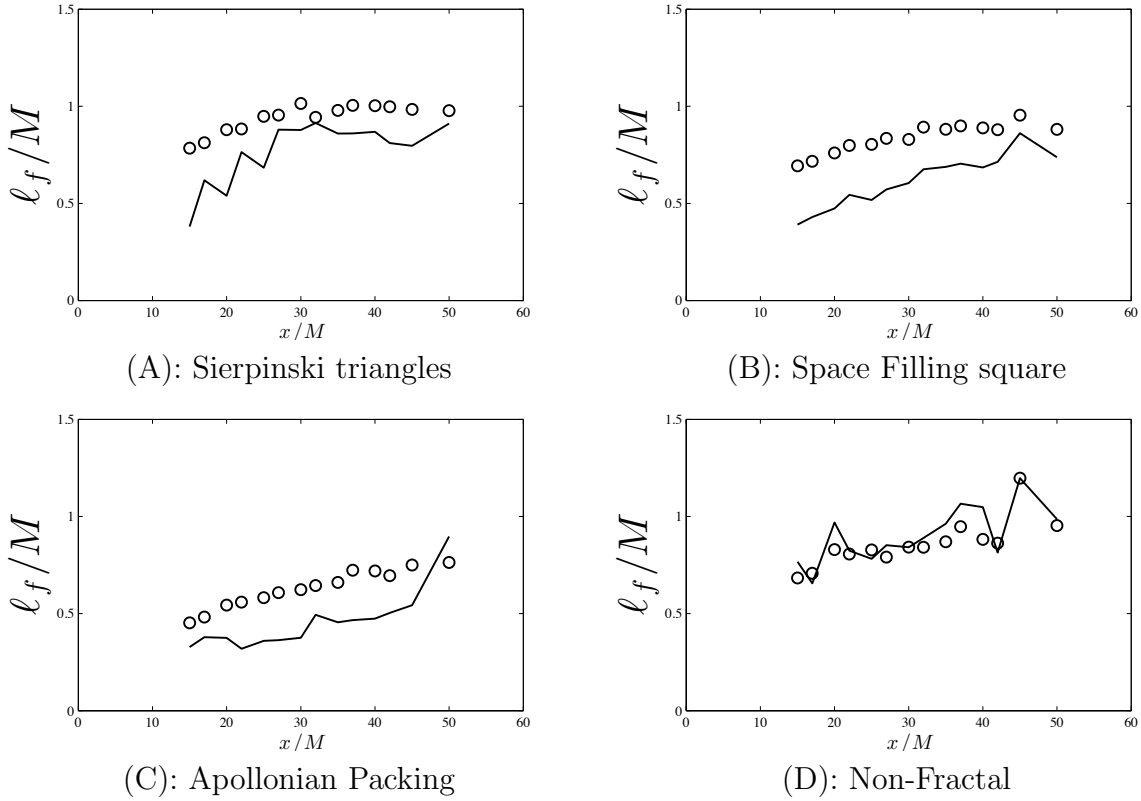

(A): Sierpinski triangles (B): Space Filling square

(C): Apollonian Packing (D): Non-Fractal

Figure 3.21: Integral lengthscale ℓ_f obtained from the longitudinal correlation function $f(r,t)$ for the four active grids. The circles represent ℓ_{fc}/M obtained by integrating $f(r,t)$ up to the first zero-crossing, whereas the solid line give ℓ_f/M obtained by integrating the correlation function over the entire range of r.

With the integral lengthscale ℓ_{fc} and the dissipation ϵ, we can study the coefficient C_ϵ. It is obtained from the classical definition of ϵ given in Eq. 2.5, which leads to:

$$C_\epsilon = \frac{\epsilon \ell_{fc}}{u_{\text{rms}}^3}, \quad \text{or} \quad C_\epsilon = \frac{\epsilon \ell_{fc}}{(2k/3)^{3/2}} = \frac{\epsilon \ell_{fc}}{u_{iso}^3}, \qquad \text{where} \qquad u_{iso}^3 = (2k/3)^{1/2}$$

when considering the turbulent kinetic energy, k involving both measured velocity components.

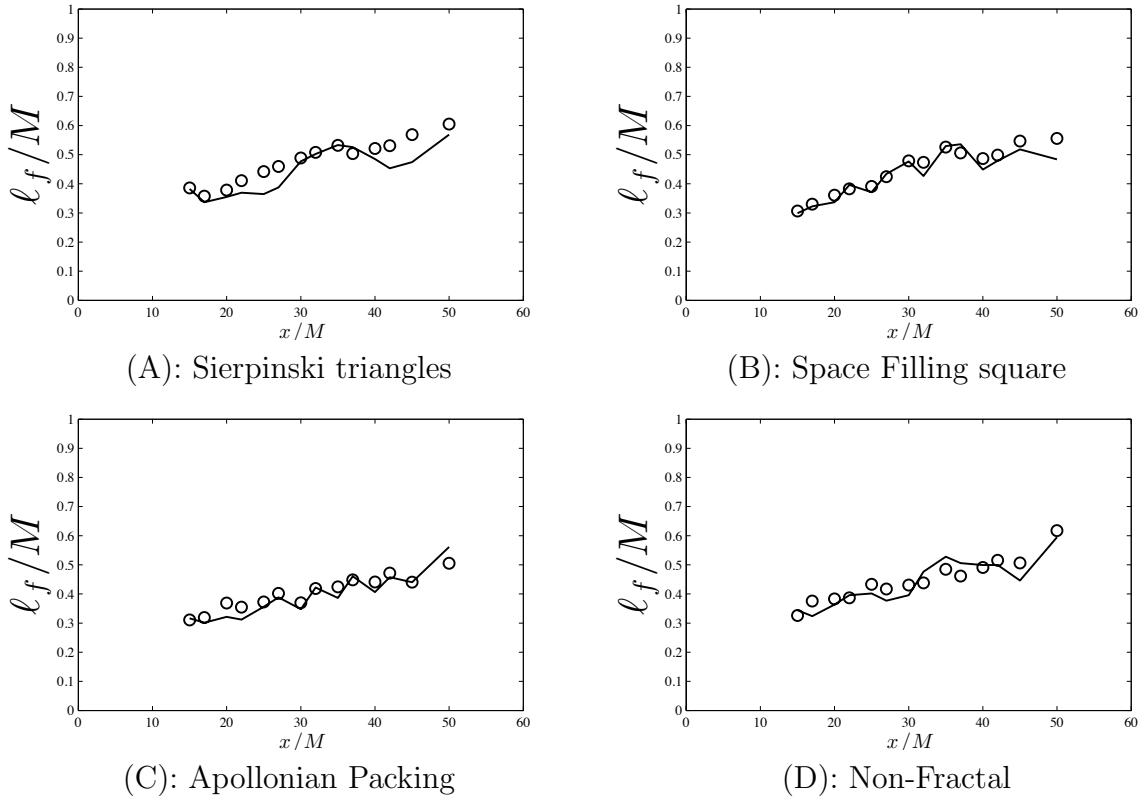

(A): Sierpinski triangles (B): Space Filling square

(C): Apollonian Packing (D): Non-Fractal

Figure 3.22: Integral lengthscale ℓ_f obtained from the longitudinal correlation function $f(r,t)$ for the four passive grids. The circles represent ℓ_{fc}/M obtained by integrating $f(r,t)$ up to the first zero-crossing, whereas the solid line give ℓ_f/M obtained by integrating the correlation function over the entire range of r.

Properties of C_ϵ (the normalized dissipation rate) have received considerable attention over several decades, as summarized by Sreenivasan[66] and Burattini et al.[67] The coefficient C_ϵ determined from both $u^2_{\rm rms}$ and k are shown in Figures. 3.23 and 3.24 for the active and passive cases, respectively. As can be seen C_ϵ is of order unity in all active-grid cases, with a weakly downstream decaying trend for the four different grids (Fig. 3.23). For the passive grid cases, the trends are very similar to the ones observed above. The trend is weakly decreasing in all cases except for the Space

Filling squares, where an approximately constant value can be discerned. Figure 3.25 presents $C_\epsilon = \epsilon \ell_{fc}/u_{\rm rms}^3$ as a function of Re_λ calculated for the 8 flows considered. The values of C_ϵ presented here are based on $u_{\rm rms}$. The graph presents two main clusters with a similar spread of values between 0.65 and 1.30, approximately, and a third one, with higher C_ϵ (~ 1.35), obtained for the intermediate Re_λ, Space Filling Square active grid. The active grid measurements are generally at higher Re_λ, forming a cluster to the right of the figure, and the passive grid data, acquired at lower Re_λ, forming the one to the left of the plot. As is clear, the values obtained differ between the different grid configurations, with the active space-filling squares (plotted as empty squares) leading to the highest coefficient C_ϵ. The Sierpinski grid yields the smallest coefficients for the passive mode (at lower Re_λ) but the second highest coefficients for the active grids at the higher Re_λ. This wide range of values show that the initial condition (here the grid geometry) play an important role as one may expect since C_ϵ depends on the large scale structure of the flow. Such dependence on initial conditions and grid geometry is in agreement with the wide range of data summarized previously by Sreenivasan[66] and Burattini et al.[67]

3.4.5 Spectral characteristics of the flow

In order to document the spectral characteristics of the flow, we compute the one-dimensional longitudinal energy spectra and present some representative results below. Hanning windowing is applied to individual segments of length of 2^{13} and

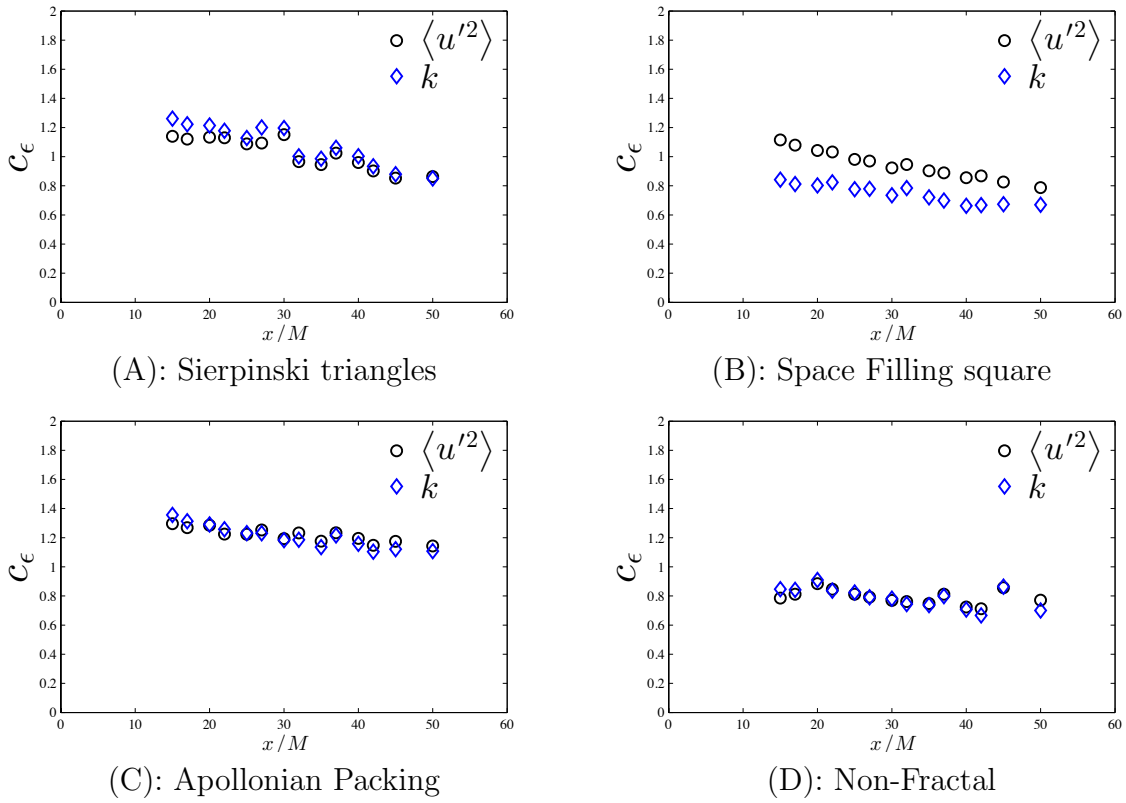

(A): Sierpinski triangles

(B): Space Filling square

(C): Apollonian Packing

(D): Non-Fractal

Figure 3.23: C_ϵ for the four active grids obtained from $\langle u'^2 \rangle$ (circles) and k (rhombs).

over 1500 such segments of the data are considered for averaging. Figure 3.26 shows $E_{11}(k_1)$ measured at $x/M = 20$ for the four grids, both active and passive. In these plots, the energy spectra are normalized in viscous units. Normalized spectra show reasonable collapse at intermediate and high wave numbers. This would be consistent with classical (Kolmogorov) scaling at inertial range and small-scales. Some differences are visible at low wave numbers as expected for different large-scale flow conditions due to different types of grids.

Another topic of interest is the downstream evolution of the energy spectra during the decay and on what length-scale a best collapse can be achieved. One should note

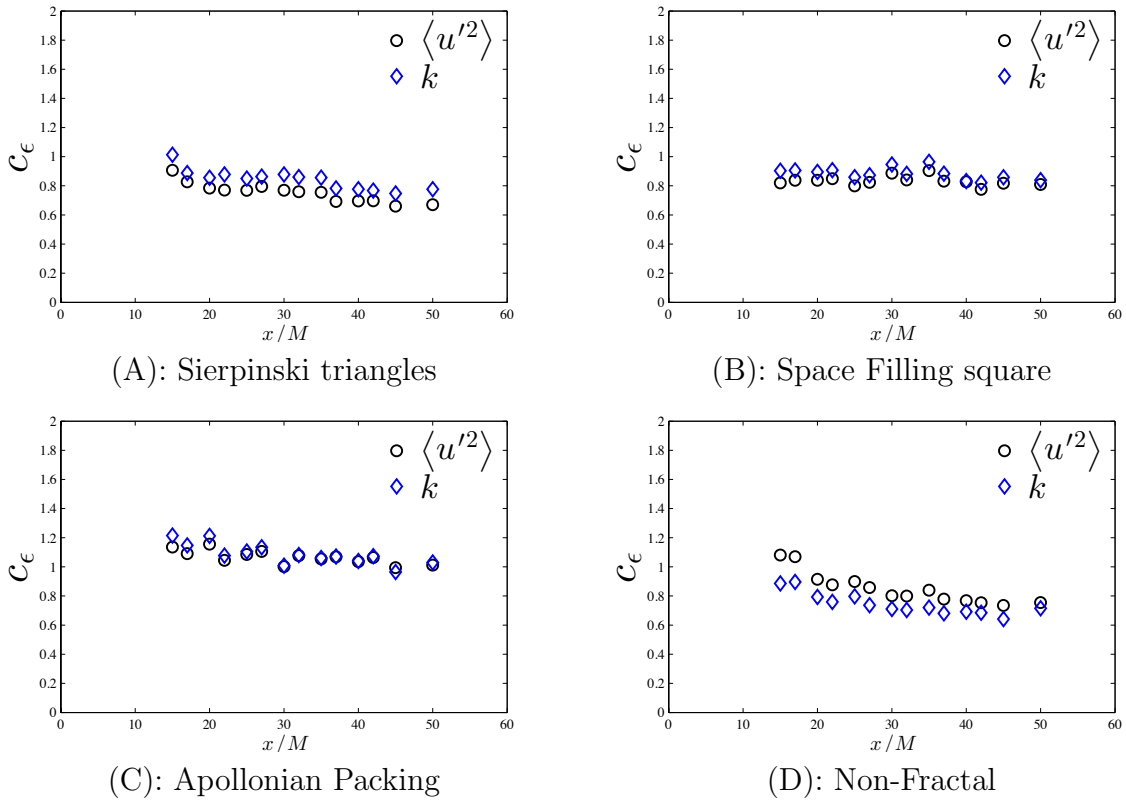

(A): Sierpinski triangles

(B): Space Filling square

(C): Apollonian Packing

(D): Non-Fractal

Figure 3.24: C_ϵ for the four passive grids obtained from $\langle u'^2 \rangle$ (circles) and k (rhombs).

that the finite spatial resolution of the hot-wire anemometers is ≈ 0.5mm, and thus, will not allow us to resolve the tails of the spectra shown below. Fig. 3.27 presents the energy spectra computed for the active Sierpinski triangle, and Space Filling fractal grids, between $x/M = 15$ and $x/M = 50$. They are here normalized by the integral length scale ℓ_{fc} (Figs. 3.27 (A) & (D)), the Taylor scale λ (Fig. 3.27 (B)), and the Kolmogorov scale η (Fig. 3.27 (C)). Both spectra normalized by the Kolmogorov and Taylor scales present good collapse in the inertial and viscous scales, as also seen in prior works.[10] The energy spectra normalized by the integral length-scale ℓ_{fc}

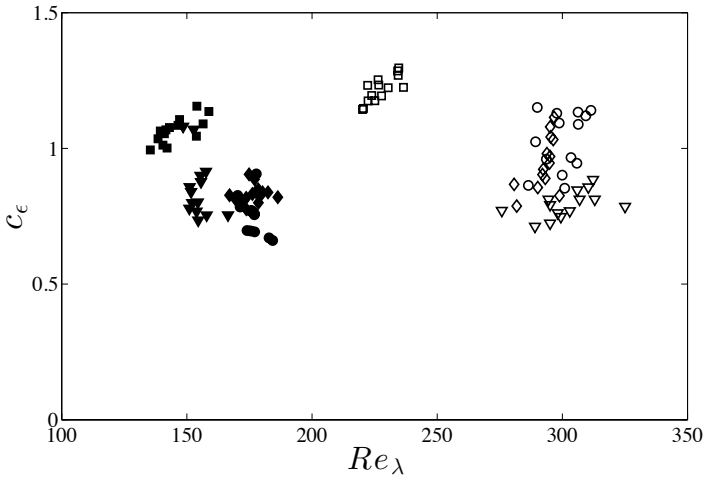

(A)

Figure 3.25: The quantity $C_\epsilon = \frac{\epsilon \ell_{fc}}{u_{\rm rms}^3}$ as a function of Re_λ for the 8 different flows presented in this study. ◯: Sierpinski, □: Space Filling Squares, ◇: Apollonian Packing, ▽: Non-Fractal.
Empty symbols: Active Grid; filled symbols: Passive Grid.

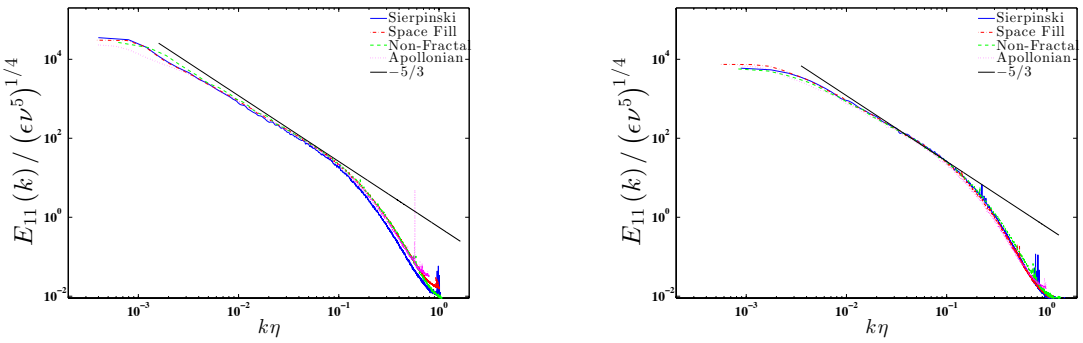

(A) (B)

Figure 3.26: Normalized 1D longitudinal energy of the four grids measured at $x/M = 20$, for both the active and passive cases, normalized by viscous units.
(A): Longitudinal energy spectra of the four active grids measured at $x/M = 20$. (B): Longitudinal energy spectra of the four passive grids measured at $x/M = 20$.

show poor collapse at the small scales, but better collapse at low wave numbers, as expected. This is also valid for the normalized spectra of the Space Filling squares (Fig. 3.27 (D)), which has a decay exponent close to 1. One should note that this

argument also holds for the active Apollonian fractal and the non-fractal grids, as well as the four passive grids (not presented here). This suggests that the spectra need more than one length scale to collapse the entire wave number range, which was also observed by Krogstad & Davidson.[16] This observation differs from the findings of Mazellier & Vassilicos[28] and of Valente & Vassilicos,[29] who in the regions closer to the grid obtained good results based on a single-length scale.

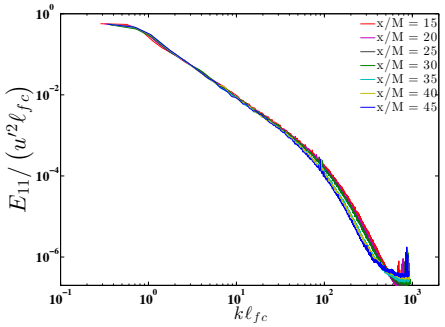

(A): Active Sierpinski: Integral scale

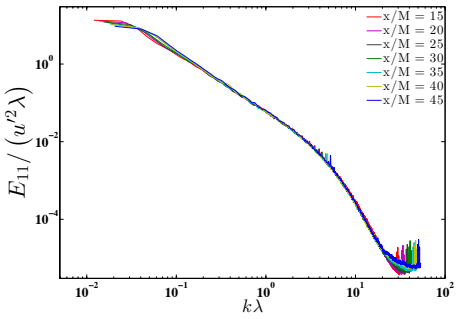

(B): Active Sierpinski: Taylor scale

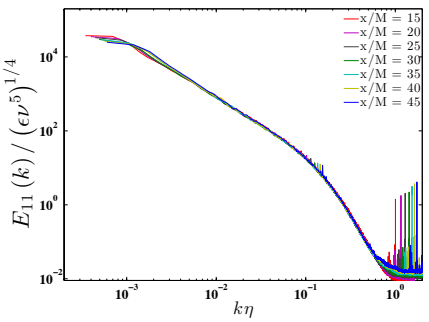

(C): Active Sierpinski: Kolmogorov scale

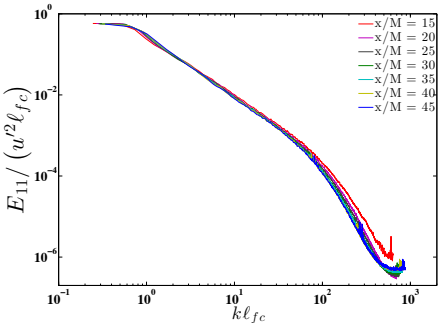

(D): Active Space Filling: Integral scale

Figure 3.27: Normalized 1D longitudinal energy spectra for active grid with the Sierpinski triangles and the Space Filling squares, from $x/M = 15$ to $s/M = 50$.

3.5 Conclusions

The study of decaying isotropic turbulence continues to be of interest due to the importance of this flow for turbulence theories and as a benchmark for numerical simulations. Motivated by recent interest in the fate of turbulence with multi-scale injection of turbulent kinetic energy[16,27,28] we have performed a set of wind tunnel experiments with various fractal grids, both active and passive. The former has allowed us to reach more elevated Reynolds numbers further downstream compared to prior experiments using passive grids.

Transverse profiles of mean velocity and turbulence r.m.s. were presented to document the level of spatial homogeneity of the flow. Special attention was placed to make sure that there is no remaining mean shear that could provide production of kinetic energy and affect the observed rate of decay. Beyond $x/M \approx 15$, the transverse spatial homogeneity was found to be quite good. The exception was the case of passive Space Filling Square fractal grid, which had to be manually adjusted to produce a flat mean velocity profile. Different fractal grids lead to different levels of large-scale anisotropy of the flow, with the ratio of root-mean-square velocities $u_{\rm rms}/v_{\rm rms}$ ranging between ~ 0.77 and 1.19, and one case leading to excellent level of isotropy (the Apollonian Packing case).

As a main conclusion from the experiments, the streamwise decay of turbulence variance $u^2_{\rm rms}$ and kinetic energy $k = (u^2_{\rm rms} + 2v^2_{\rm rms})/2$ was found to be consistent with power-law behavior, with decay exponents between about 1.0 and 1.3. The

downstream accessible range was between $15 < x/M < 50$, where M is the mesh-size of the grids (i.e. the spacing between shafts that support the winglets whose diagonal size is M).

The rate of dissipation ϵ was estimated from the measured and fitted kinetic energy decay rate, leading to estimates of Taylor scale λ, Reynolds number Re_λ and the coefficient $C_\epsilon = \epsilon_{\text{decay}} \ell_{fc} / u_{\text{rms}}^3$. Longitudinal correlation functions showed some deviations from classically expected trends at large scales for several of the active grid cases, displaying negative lobes. But the inferred integral length-scales could be used to determine C_ϵ and its associated uncertainties. C_ϵ was found to depend weakly on the type of fractal grid, and in some cases was constant or in other cases evolved slowly downstream. Also, Re_λ decayed in most cases, but in some cases remained reasonably constant. Energy spectra and their scaling were examined and good collapse in viscous or Taylor-scale units was found in the inertial and viscous ranges.

The precise values of the decay exponent n, the coefficient C_ϵ or the trends in Re_λ were found to depend on the geometry of the initial condition, although it was challenging to discern systematic or monotonic trends with respect to Re_λ, component anisotropy, grid fractal dimension, turbulence intensity or blockage.

As is well-known, the properties of decay of isotropic turbulence are intimately linked with the behavior of the largest scales of the flow, i.e. the low-wavenumber region in Fourier space. It is quite possible that the largest eddies in our experiment are

affected by wind tunnel walls, considering that the integral scale was on the order of $M = 0.16$ m, i.e. only about 1/3 of the distance between the centerline measurement location and the wind tunnel walls. Moreover, as can be seen in the correlation functions presented in Figure 4.10, significant correlations (specifically anti-correlations) exist at distances comparable with the wind tunnel cross-section. The challenges in identifying particular trends of the decay exponent and other parameters associated to the decay may be due to the lack of ideal conditions at the largest scales of the experiment. Nevertheless, the basic observations of power-law decay with exponents in the quoted range for all the types of grids tested (fractal, non-fractal, active and passive) are robust.

Chapter 4

Decaying Turbulence in the Presence of a Shearless Uniform Kinetic Energy Gradient

4.1 Introduction

As we have seen in the preceding chapters, the rate of decay of kinetic energy in homogeneous isotropic turbulence is of great interest and has been studied extensively for the past decades using theoretical, computational, and experimental tools. Different experimental approaches have been developed to generate such a flow, ranging from classic passive grid experiments at moderate Reynolds numbers[14] and recent measurements in pressurized facilities at high Reynolds numbers,[18] to active grid se-

tups,[15,33] and more recently, with the use of fractal (or multi-scale) grids (Chapter 3).[16,37,68] The great majority of these works have reported observing power-law behaviors with downstream decay distance (x) of the form $k \sim x^{-n}$ (where $k = \frac{1}{2}\langle u_i' u_i' \rangle$ is the turbulent kinetic energy, or single-component surrogates), with decay exponents n ranging from $1 \leq n \leq 1.4$. As summarized in Chapter 2, most results fall within the range of values obtained by the theoretical approaches of Batchelor,[23] Saffman,[24] Kolmogorov,[22] and George,[10] but a trend has emerged recently[15,16,18,37] where agreement with the prediction by Saffman[24] is being observed more often than not.

Building on homogeneous isotropic flow, the fate of turbulence in the so-called shearless turbulent mixing layer[69–71] has also been studied, although less extensively than homogeneous turbulence. In this flow, two regions exist with two distinct levels of turbulent kinetic energy but with a uniform mean velocity. Downstream the initially sharp jump in kinetic energy levels mixes, and the jump becomes smoother. The flow evolution depends upon the interactions between the two kinetic energy layers. This flow can be considered to be a simple approach to study inhomogeneous turbulence since the absence of mean shear in the flow prevents shear-production of turbulent kinetic energy while still exhibiting non-trivial spatial transport. The prior studies[69–71] have examined the downstream evolution and the growth of the width of the kinetic energy mixing layer, as well as deviations from Gaussian statistic in the velocity field (large-scale intermittency). It was shown that the location of the largest

anomaly in skewness and flatness occurs below the center line of the kinetic energy mixing layer, specifically in the low kinetic energy region. Energetic eddies from the high energy side that occasionally penetrate the regions of lower kinetic energy provide a plausible explanation for the measured trends. However, the streamwise decay of kinetic energy at various locations across the mixing layer remains poorly characterized.

The objective of this work is to study the decay of kinetic energy in a shearless turbulent flow by simplifying the problem as much as possible. We note that in the context of canonical turbulent shear flows, homogeneous shear flow is in many ways "simpler" than the standard mixing layer. In the former, the shear and rate of turbulent production is homogeneous, while the classic mixing layer has significant changes in shear across the layer, the mean velocity has inflection points, and spatial transport occurs towards various directions at different rates. Motivated by this observation, we pose a similar analogy for the spatial distribution of kinetic energy: how does a flow evolve in which the spatial distribution of kinetic energy does not go from one constant value to another as in a shearless mixing layer, but displays a uniform (linear) gradient. For such a study an experimental setup has been designed to generate a linear distribution of turbulent kinetic energy in a direction (y) perpendicular (spanwise) to the mean velocity, in a flow in which the mean velocity is uniform. I.e. at some initial (reference) downstream position x_{ref}, we seek to generate

a kinetic energy distribution of the form:

$$k\left(x_{\mathrm{ref}}, y\right) \sim \beta(y - y_0) \tag{4.1}$$

for some constant β and spanwise reference location y_0. The reader should note that in the context of this work (presented in this Chapter and in Chapter 5), the coordinate system has been rotated such that the horizontal direction (spanwise) is represented by the y component, and the vertical one by the z component.

Experiments will be performed to explore the decay rates of kinetic energy at different y locations, and to investigate any departure from Gaussian statistics in the velocity field. The experimental apparatus is described in section 4.2, the flow characterization is presented in section 4.3, and the results, discussions, and conclusions are provided in sections 4.4 to 4.5.

4.2 Experimental Facilities

4.2.1 Wind tunnel and active grid

Measurements for this experiments are also performed using the Corrsin Wind Tunnel at the Johns Hopkins University. More details on the facility are provided in Chapter 1. The experimental setup is shown schematically in Figure 4.1.

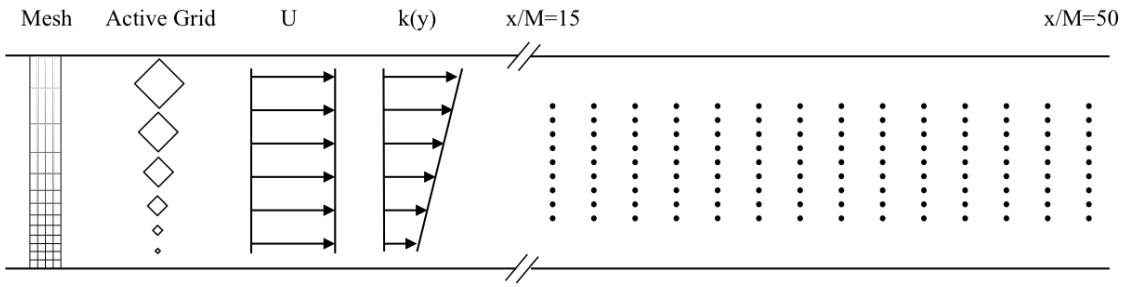

(A)

Figure 4.1: Schematic of test section of the wind tunnel viewed from the top (not to scale) showing the combination of the mesh and the active grid producing the desired uniform mean velocity and linear kinetic energy profiles. Also shown schematically are the locations of the various measurement points downstream of the active grid that allow to characterize the streamwise decay at various spanwise positions.

The active grid apparatus was equipped with 66 winglets arranged such that in the horizontal (y) direction there are large winglets with strong flow blockage generating high levels of kinetic energy, then winglets with holes that provide lower blockage, then smaller winglets which are placed less densely, ending at the other side of the grid with no winglets and only the rods providing the smallest level of kinetic energy. An empirical iterative procedure was used and different configurations were tested and profile measurements (to be described below) performed. The configuration presented (see Figure 4.2) was the one that displayed the most desirable profile of kinetic energy, i.e. the one most closely linear with a significant range of kinetic energy values (changing by over a factor 2 from one end to the other).

In order to achieve a shearless flow with constant mean velocity in both the horizontal and vertical directions, meshes of various sizes were installed upstream of the active grid. In order to prevent lower mean velocity in the higher-blockage side, and

vice versa, the coarser meshes were placed in front of the larger winglets while the finer meshes were placed upstream of the least fluctuating side of the grid. Again, an iterative empirical method had to be used to choose the various meshes and their locations. Such configuration leads to the generation of a shearless flow while maintaining a linear gradient of kinetic energy in the horizontal plane, which will be presented in Section 4.3. The applied flow conditioning did not succeed in generating completely isotropic turbulence. As will be verified, the r.m.s based levels of anisotropy were on the order of 15% with, in this flow, the spanwise velocity fluctuation exceeding the streamwise component.

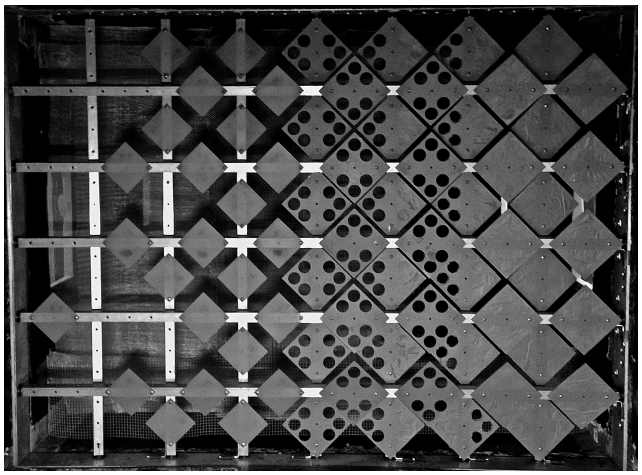

(A)

Figure 4.2: Photograph of the active grid in the wind tunnel. The images shows the range of sizes and blockage of the winglets fitted to the shafts of the grid, as well as the upstream meshes in the background. The blockage area of the four agitators used are (from left to right) 54 cm^2, 73 cm^2, 88 cm^2, and 103 cm^2, respectively.

4.2.2 Instrumentation and data acquisition

Data are acquired using the in-house built, constant temperature X-wire anemometers introduced in Chapters 1 and 3. The probes are calibrated in the jet of a TSI automatic velocity calibrator using flow velocities ranging from 3 to 17 m/s, and the angular calibration is performed at eleven different yaw angles α, with 6^o increments. The anemometers are operated in a constant-temperature anemometry (CTA) mode, and are controlled by a TSI-IFA-300 system. For this study, three data records are acquired at each location. They are sampled at 40kHz using a 20kHz low-pass filter for 104.86 seconds, adding up to a total sampling time of $3 \times 104.86 = 314.58$ seconds, or over 12.5×10^6 samples.

The measurements are taken at 14 different downstream locations located at $x/M = [15, 17, 20, 22, 25, 27, 30, 32, 35, 37, 40, 42, 45, 50]$, which is then repeated at 9 spanwise locations $y = [0.40, 0.45, 0.50, 0.55, 0.60, 0.65, 0.70, 0.75, 0.80]$ meters from the walls. Thus the total number of acquisition points is 126 locations downstream of the active grid (see Figure 4.1). Tests for homogeneity are performed both in the horizontal and vertical directions at $x/M = 14$, upstream of the first measuring points, as shown in Figure 4.3.

4.3 Flow characterization

The main objective of the experimental setup is to generate a shearless flow with an initially linear distribution of the turbulent kinetic energy in the transverse plane of the form:

$$\frac{k}{\langle u \rangle^2}(x_{\text{ref}}, y) = \beta \left(\frac{y - y_0}{M} \right), \tag{4.2}$$

at some reference, initial downstream location x_{ref}. The parameter β and offset y_0 characterize the profile at this initial reference location (as before, M is the mesh-size). In the remainder we shall set $x_{\text{ref}} = 15M$. The active grid was iteratively designed as discussed in Section 4.2. Horizontal and vertical traverses of the mean velocity and fluctuating velocity variance profiles are obtained downstream of the active grid at $x/M = 14$, from $y/M = 0.98$ to $y/M = 6.90$, at the test-section core at $z/M = 2.96$ and another perpendicular profile from $z/M = 1.78$ to $z/M = 4.64$ at the centerline $y/M = 3.95$. While the main measurements will be performed in the core region of the wind tunnel at $z/M = 2.96$, and between $2.63 \leq y/M \leq 5.26$, the inflow profiles characterization is done across a larger region to ensure that the appropriate flow was also being generated outside of the direct area of interest, to minimize the possibility of mean shear existing near the region of interest. The hot-wire anemometer was set on a traverse system and data was acquired every 6 cm across the channel for these measurements.

Figure 4.3 shows the streamwise (u) and transverse velocity components (v in the horizontal direction, and w in the vertical one), taken both in the horizontal (y) and vertical (z) traverse directions at $x/M = 14$. The mean velocity shown in figures 4.3 (A) and (B) presents a nearly shear-free profile with a variation of 0.39 m/s between the maximum and minimum points, whereas the standard deviation is distributed in a different manner. The variance of both the u and v velocity fluctuations in the horizontal plane are distributed in an approximately linear fashion in the central portion of the test section, in the core region ($2.63 \leq y/M \leq 5.26$ at $z/M = 2.96$) considered for the decay measurements, as seen in Figure 4.3 (C). In the vertical direction (Figure 4.3 (D)) for both the u and w components the distribution is nearly constant since the mean gradient only occurs in the y and not in the z direction, by construction.

The results presented in Figure 4.3 were obtained by traversing the X-wire probe horizontally and vertically at $x/M = 14$ downstream of the grid. However, the actual measurements performed to study the decay rates were conducted by traversing the hot-wire probes in the streamwise (x) direction, and repeated for nine horizontal (y) positions. This resulted in nine independent sets of set of measurements. In each of these, the wind-tunnel was turned down, and the probes were re-calibrated in between each one of these streamwise traverses. In each of the experiments the mean velocity was slightly different due to difficulties to prescribe very precisely the velocity in the facility. Therefore, the mean velocities presented in Figure 4.4 have been normalized

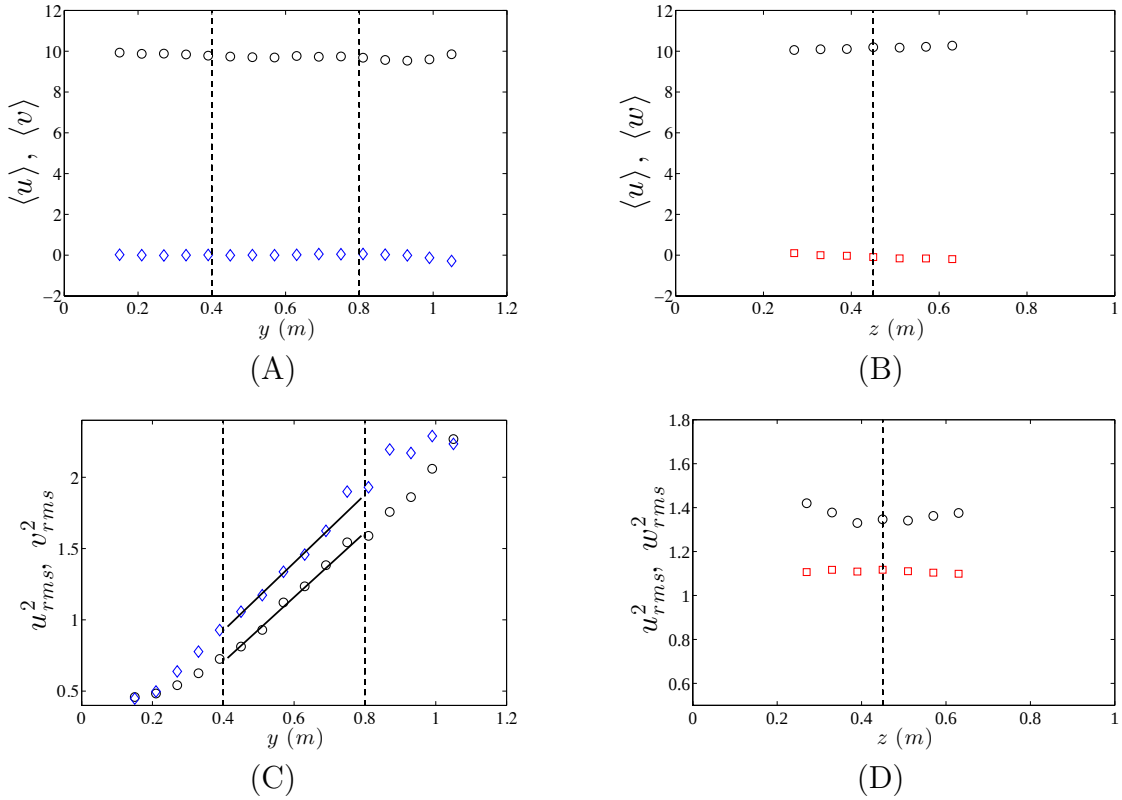

Figure 4.3: Vertical and horizontal transverse profiles of the flow at $x/M = 14$ behind the active grid. The vertical lines represent the limits of the region of interest, where the kinetic energy profile is nearly linear. Panels (A) & (B): $\circ$: $\langle u \rangle$, $\diamond$ $\langle v \rangle$, $\square$ $\langle w \rangle$. Panels (C) & (D): $\circ$: u^2_{rms}, $\diamond v^2_{rms}$, $\square$ w^2_{rms}. For (A) and (C) the transverse location is $z = 0.45$m, and for (B) and (D) it is $y = 0.6$m. The black lines fitted to panel (C) show the quasi-linearity of the distribution in the region of interest. $\langle u \rangle$, $\langle v \rangle$, and $\langle w \rangle$ are presented in m/s, and u^2_{rms}, v^2_{rms}, and w^2_{rms} are in m^2/s^2

by the ones measured at the first downstream location, $x/M = 15$. Similarly to the results presented in Figure 4.4 (A) the profile is nearly without mean shear, with the largest differences in velocity observed being on the order of 2%-3% at the end of the test section.

The quantities presented in figures 4.4 (B), (C), & (D) have been normalized by their respective mean velocities, and the same conclusions can be drawn; the variances in both directions are distributed in a nearly linear fashion at the first downstream location $x_{\text{ref}}/M = 15$, with $u_{\text{rms}} \leq v_{\text{rms}}$ throughout the test section. The isotropy ratio $I = u_{rms}/v_{rms}$ shown in Figure 4.4 (B) shows that the transverse component is larger than the longitudinal one, and therefore $I < 1$. This trend increases as the flow evolves downstream, starting from $I \sim 0.9\%$ at $x/M = 15$, to about $I \sim 0.75\%$ at $x/M = 45$.

4.4 Results and discussion

4.4.1 Energy decay rate

The measurements acquired in the test section of the wind tunnel at each spanwise location y are compared and fitted with power laws of the form:

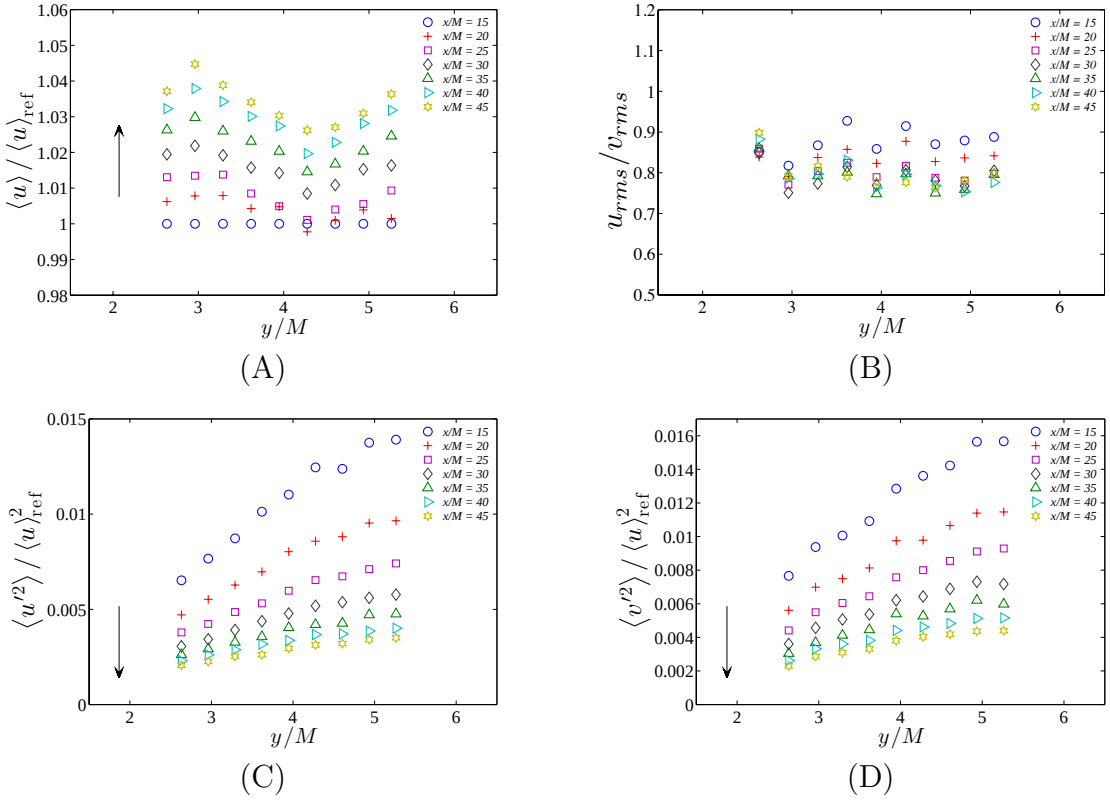

Figure 4.4: Profiles of mean velocity, variances, and isotropy ratios at all downstream location, plotted at every $x/M = 5$ for clarity. The arrows indicate the progression of the flow as it evolves downstream.

$$\frac{\langle u'^2 \rangle}{\langle u \rangle^2} \equiv A_u \left(\frac{x - x_{0u}}{M} \right)^{-n_u}, \quad \frac{\langle v'^2 \rangle}{\langle u \rangle^2} \equiv A_v \left(\frac{x - x_{0v}}{M} \right)^{-n_v}, \quad \frac{k}{\langle u \rangle^2} \equiv A_k \left(\frac{x - x_{0k}}{M} \right)^{-n_k} \tag{4.3}$$

where the kinetic energy is computed as a function the two measured velocity components, $k = \frac{1}{2}\left(\frac{3}{2}\langle u'^2 \rangle + \frac{3}{2}\langle v'^2 \rangle\right)$, and x_{0u}, x_{0v}, and x_{0k} are the corresponding virtual origins for each variable. Initially, fits without virtual origins are performed (i.e. setting $x_{0u} = x_{0v} = x_{0k} = 0$). Figure 4.5 show log-log plots of $\langle u'^2 \rangle / \langle u \rangle^2$, $\langle v'^2 \rangle / \langle u \rangle^2$, and $k / \langle u \rangle^2$, for the 9 spanwise locations. The solid lines are least-square fits of the power laws computed in a logarithmic scale, of the form:

$$\ln\left(\frac{\langle u'^2 \rangle}{\langle u \rangle^2}\right) = \ln\left(A_u\right) - n_u \ln\left(\frac{x - x_{0u}}{M}\right), \tag{4.4}$$

(similarly for $\langle v'^2 \rangle$ and k), and the dashed lines represent the error associated with the quality of the fits. These experimental uncertainties associated with each decay exponent are determined with a 95% (2 σ) confidence interval.[63] The decay exponents n, the prefactors A, and the virtual origins x_0 (when these are used) have dependencies on y position.

All energy decay rates measured in the wind tunnel, and shown in Figure 4.5, exhibit clear power-law behaviors with only small associated deviations, despite the uniform kinetic energy gradient in the spanwise direction. As presented in Table 4.1,

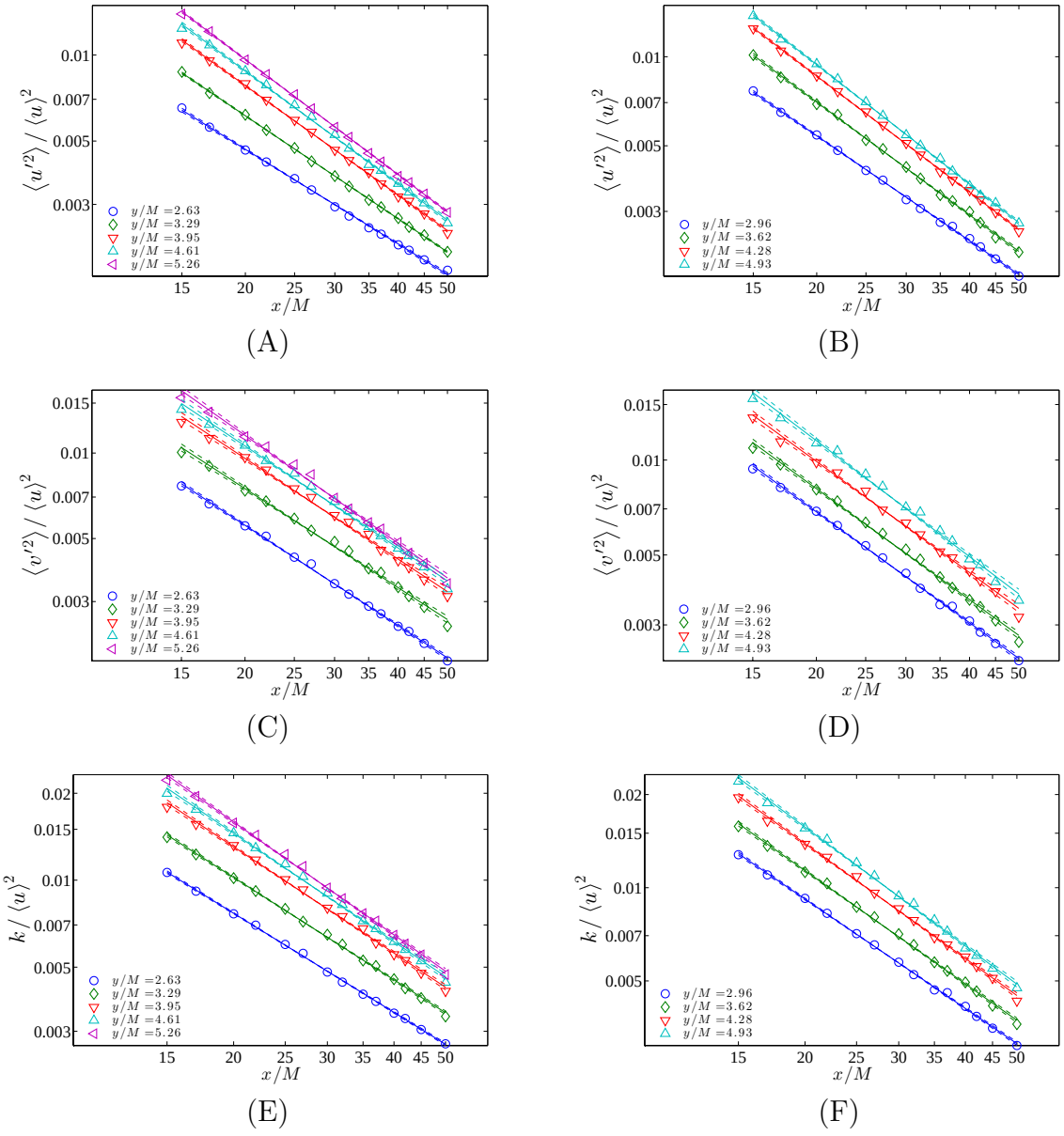

Figure 4.5: Decay rates of velocity component variances and turbulent kinetic energy for the nine different spanwise directions, for $\langle u'^2\rangle / \langle u\rangle^2$, $\langle v'^2\rangle / \langle u\rangle^2$, and $k / \langle u\rangle^2$, without using virtual origins.

the decay exponent n ranges between $n_u = 1.1$ at the lowest, and $n_u = 1.35$ at the highest, when no virtual origins are included in the power law fits. Similar trends are observed for the other components of the flow, and more details are provided in Table 4.1. Overall, the decay exponents are in a similar range as the ones reported in the literature for decaying fully homogeneous turbulence. Among others, Comte-Bellot & Corrsin (1966)[14] found $1.15 < n < 1.29$, Krogstad & Davidson (2010)[62] obtained values that fall between $n = 1.15$ and 1.20, and Thormann & Meneveau (2014)[37] reported $1.0 < n < 1.30$ for a large array of cases using fractal grids.

However, the lines are not precisely parallel as y is varied. In particular, it is apparent that the higher y curves have slightly steeper slopes. Figure 4.6 presents the decay exponents n_u, n_v, & n_k obtained from the fits at all y locations with and without (see below) a virtual origin. A clear upward trend in present in all cases, leading to the observation that the decay exponent of the power-law behavior increases with the local turbulent intensity inside the layer with linear kinetic energy gradient: the higher the turbulent kinetic energy, the higher the decay exponent.

It is often mentioned in the literature[37,62] that results can depend significantly on the use of a virtual origin. We determine x_0 at which a minimum σ_{fit} for each horizontal position is obtained (σ_{fit} is defined as the standard deviation of the difference between the power law fit and the recorded data[37]). The decay exponents shown in Table 4.1, and plotted in figures 4.6 (B), (D), and (F), obtained with a virtual origin x_0, differ in magnitude from those cited above without virtual origin as

they now fall between $n_u \sim 1$ and $n_u \sim 1.6$. However, the trends in the distribution remains the same: a clear increasing trend with respect to the horizontal position y is observed. Therefore, despite being quite sensitive to using a virtual origin, the decay exponents n consistently exhibits an increasing trend with the gradient of kinetic energy produced by the active grid.

4.4.2 Kinetic energy decay parameterization

In section 4.3, we have shown that a linear gradient of kinetic energy was successfully imposed in the transverse direction at the first downstream location of the test section of the wind tunnel, x_{ref}. Furthermore, in the previous section (4.4.1) we have observed a well defined power-law behavior for the spatial evolution of the turbulent kinetic energy downstream. Next we examine the possible y-dependence of the prefactor of the power law, $A(y)$, as determined from the fitting of the power laws discussed in the previous section. Figure 4.7 shows a comparison of the prefactor as function of y and compared with the linear behavior $\beta(y - y_0)/M$, observed at the initial location. Good agreement can be observed.

Results presented so far suggest that a possible functional form as function of both x and y can be proposed. Specifically, a functional form for either $k^* = \langle u' \rangle^2$, $k^* = \langle v' \rangle^2$, or $k^* = \frac{1}{2}\left(\frac{3}{2}\langle u' \rangle^2 + \frac{3}{2}\langle v' \rangle^2\right)$ that complies with linear behavior at a fixed

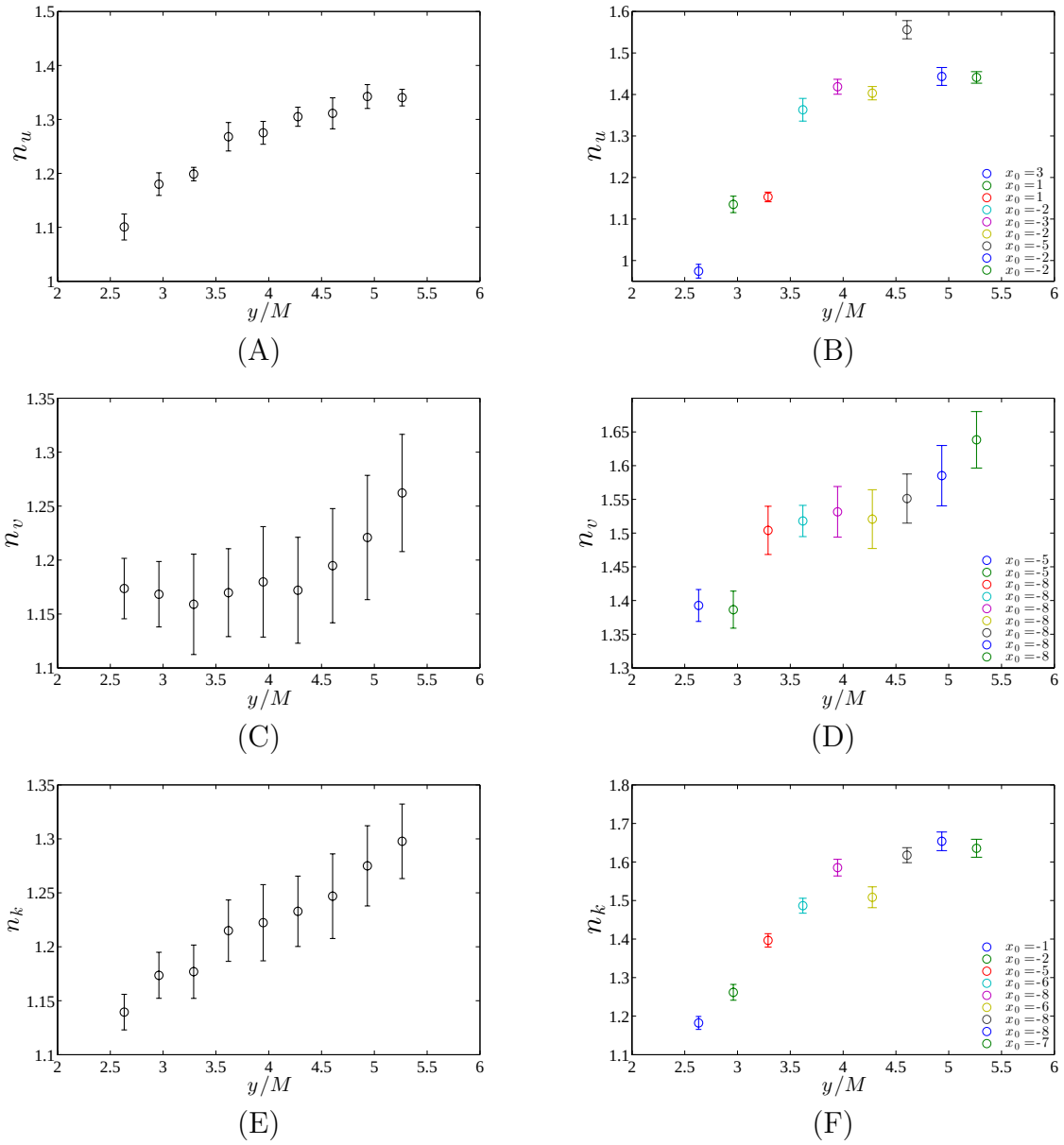

Figure 4.6: Measured decay exponent $n(y)$ for $\langle u'^2\rangle / \langle u\rangle^2$, $\langle v'^2\rangle / \langle u\rangle^2$, and $k/\langle u\rangle^2$, computed with (left column) and without (right column) virtual origins, as function of spanwise position y. A clear trend of increasing in the direction of increasing turbulent kinetic energy is observed in all cases. The symbol colors indicate the virtual origin value that minimizes the error in the fit.

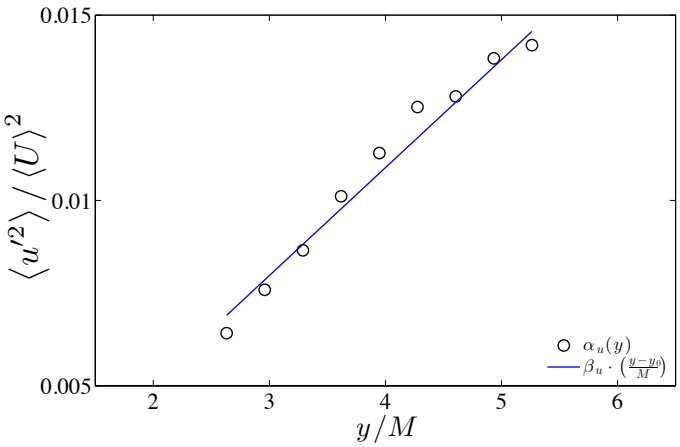

(A)

Figure 4.7: Comparison of the coefficient from the model for the evolution of $\langle u'^2 \rangle$ and the fit $\beta\,(y - y_0)\,/M$ plotted as function of y, with β and y_0 fitted through the data at $x_{\text{ref}} = 15M$ in Equation 4.2. $\alpha(y)$ is the prefactor of the renormalized power-law $\alpha(y)\,(x/x_{\text{ref}})^{-n(y)}$, and determined from fits at the 9 horizontal locations. The coefficients shown are for $\langle u' \rangle^2$ (similar results are obtained for $\langle v' \rangle^2$, and k).

$x = x_{\text{ref}}$ and a power-law behavior in x with a y-dependent exponent is given by

$$\frac{k^*(x,y)}{\langle u \rangle^2} = \beta \left(\frac{x}{x_{\text{ref}}}\right)^{-n(y)} \left(\frac{y - y_0}{M}\right) \tag{4.5}$$

where β is the slope of the the imposed kinetic energy gradient at $x = x_{\text{ref}} = 15M$ obtained with a linear fit, and y_0 its corresponding offset. The values of the decay exponent $n(y)$ used for this model are the ones obtained by fitting the data without a virtual origin presented in Figures 4.6 (A), (C), and (E).

Comparing this simple model to the data shows good agreement, as presented in figures 4.8 (A), (B), and (C), respectively.

While a linear distribution in the horizontal plane is indeed recovered at the first

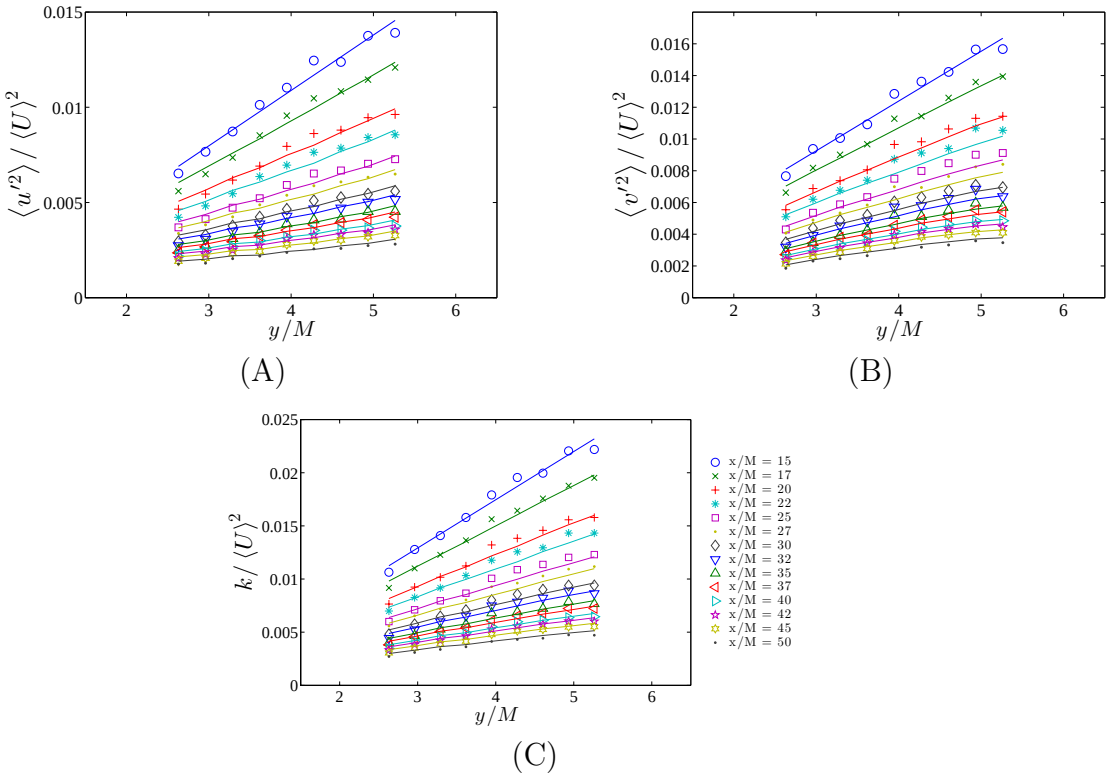

Figure 4.8: Comparison of the parameterization for the evolution of the kinetic energy (Equation 4.5) with the measured data.

downstream location and power laws are obtained as function of x for any given y value, the relation shows that at downstream locations $x > x_{\text{ref}}$ the y-dependence ceases to be exactly linear, since the exponent $n(y)$ depends upon y.

It is worthy to note that we cannot be certain that the dissipation measured from the variance of the derivative of the velocity based on the X-wire probes is sufficiently accurate (in Chapter 5 this issue will be addressed using a more accurate probe). That is because the active length of the hotwire probe is larger than the smallest scales in the flow. Furthermore, the classical approaches to determine ϵ used for homogeneous isotropic flows, such as based on the structure functions or the spectra, may be less reliable in this flow due to the inhomogeneity introduced in the y-direction by the grid.

Testing a $k-\epsilon$ model based approach is possible using the distribution of the turbulent kinetic energy as parameterized in Equation 4.5. In the $k-\epsilon$ model, the dissipation rate evolves as follows (neglecting streamwise spatial diffusion):

$$\langle u \rangle \frac{\partial k}{\partial x} = \frac{\partial}{\partial y}\left(\frac{\nu_T}{\sigma_k}\frac{\partial k}{\partial y}\right) - \epsilon \tag{4.6}$$

where $\nu_T = c_\mu \, k(x,y)^2/\epsilon(x,y)$ (the standard values for the coefficients, $c_\mu = 0.09$ and $\sigma_k = 1$ are taken). Replacing the parameterized expression for $k(x,y)$ (i.e. we assume it is known), one obtains a first-order nonlinear ODE for ϵ to be integrated in the y

direction (it is first order in y because ϵ enters only in the eddy-diffusivity acted upon by the divergence operator). This ODE in y can be integrated separately for each x, provided a boundary condition $\epsilon(x, y_1)$ is provided at some particular y_1. Since we do not have sufficiently accurate measurements of $\epsilon(x, y_1)$, we adopt the following procedure to select a boundary condition: the dissipation rate $\epsilon(x, y_1)$ is set to the value of $-dk/dt = -\langle u \rangle dk/dx$ obtained at $y_1 = 1$m from the wall using Equation 4.5. A linear function is fitted to the distribution of decay exponent (see Figure 4.6 (F)) to obtain a value of $n = 1.37$ at $y = y_1$. In that region the isotropy ratio between the two components is close to 1, and the distribution of the kinetic energy flattens out, as shown in Figure 4.3 (D), thus suggesting that spatial transport is likely to be less important. Once the boundary condition is set, the ODE is integrated between $y = 1$m toward smaller values of y.

Solving for $\epsilon(x, y)$ at each given x gives the results presented in Figure 4.9. The results show that given the initial conditions as described above, the $k - \epsilon$ model predicts a relatively small contribution from the spatial diffusion term. If it is correct that the values obtained for ϵ are very close to the ones obtained for $-dk/dt$, in that case it would imply that the evolution of the kinetic energy is driven mostly by the dissipation rate that yields a y-dependent decay rate exponent dictating the decay, rather by lateral spatial diffusion. However, it must be recalled that the $k - \epsilon$ modeled dissipation is very uncertain due to possible limitations of the $k - \epsilon$ model in this flow where it has never been tested before, and also due to uncertainties in the

boundary condition values $\epsilon(x, y_1)$ we used. One should also recall the possible effects of pressure fluctuations. The full spatial diffusion term contained in the transport equation for the turbulent kinetic energy (again neglecting streamwise diffusion and molecular viscous diffusion) can be written as:

$$\langle u \rangle \frac{\partial k}{\partial x} = -\frac{\partial}{\partial y} \left(\frac{1}{2} \left\langle v' u_j' u_j' \right\rangle + \frac{\langle v' p' \rangle}{\rho} \right) - \epsilon. \tag{4.7}$$

Further measurements with more accurate sensors to evaluate ϵ with sufficient accuracy must be conducted in order to infer the net impact of the spatial diffusion term, including the pressure fluctuations (see Chapter 5).

4.4.3 Correlation functions and integral length-scale

In this study we are also interested in the evolution of the integral length-scale in this inhomogeneous flow. It can be obtained from the second order longitudinal correlation functions $f(r) = \langle u'(x+r)u'(x) \rangle / \langle u'^2 \rangle$ (Taylor's frozen equilibrium hypothesis is used to evaluate the correlation function from the data). Figure 4.10 (A) and (B) show representative longitudinal correlation functions at fixed horizontal and longitudinal positions, respectively. As can be seen, the autocorrelation functions are well behaved, with only very small negative lobes being observed in some of the cases, before reaching the asymptotic decorrelation at large distances.

The longitudinal integral scale ℓ is determined by integrating $f(r)$ up to the first

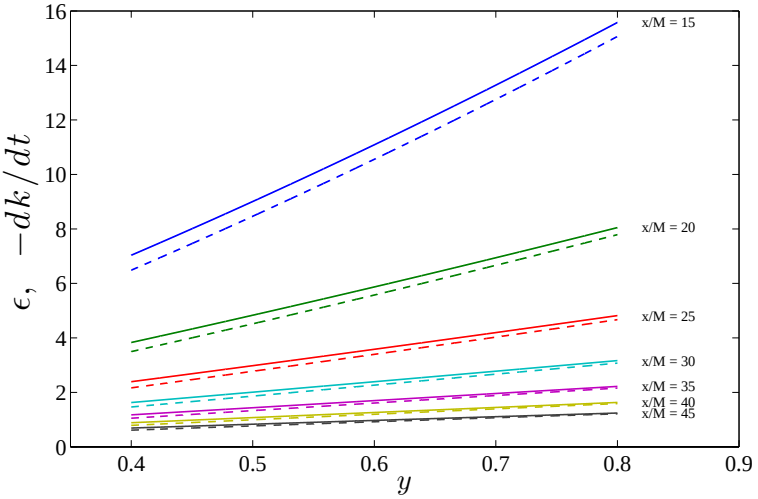

(A)

Figure 4.9: Terms from the kinetic energy transport equation plotted in m^2/s^3. The dashed lines represent the decay rate of kinetic energy, dk/dt (strictly speaking $\langle u \rangle \frac{\partial k}{\partial x}$, obtained analytically from Equation 4.5), whereas the solid lines show the results obtained from the integration of the ϵ equation using the $k-\epsilon$ model to estimate the spatial diffusion term, and the values of $-dk/dt$ set at $y = 1$ as boundary condition for the integration. Results are plotted for 7 downstream locations: $x/M = 15$, $x/M = 20$, $x/M = 25$, $x/M = 30$, $x/M = 35$, $x/M = 40$, $x/M = 45$, ranging from top to bottom on the plots).

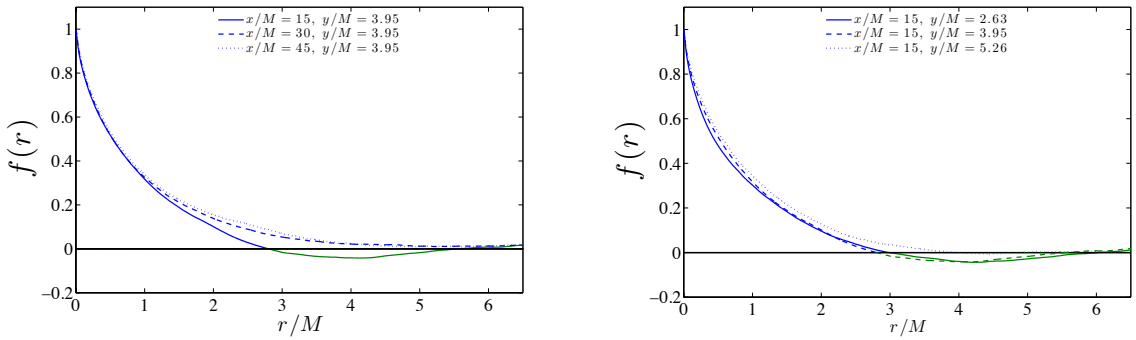

(A) (B)

Figure 4.10: Longitudinal autocorrelation functions computed at different locations in the test section.

zero-crossing, as follows:

$$\ell_{fc} = \int_0^{r_c} f(r)dr \tag{4.8}$$

where r_c is the first zero-crossing of $f(r)$, which is a procedure commonly used.[16,37] In this manner, ℓ_{fc} is measured at each of the 126 streamwise and spanwise measurement locations. The results, normalized by the mesh size of the grid M, are presented in Figure 4.11.

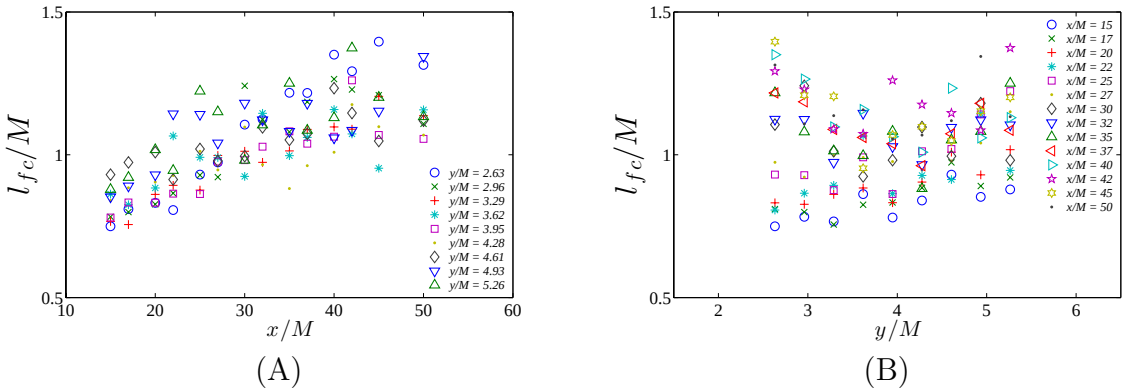

Figure 4.11: Normalized longitudinal integral length-scale, ℓ_{fc} obtained by integrating the correlation function $f(r,t)$ up to the first zero-crossing, plotted against x/M (a) and y/M (b).

It is observed that the integral lengthscale grows slowly with x as the flow evolves downstream, as it is the case of homogeneous isotropic turbulence[14,62] (see Figure 4.11 (A)). However, when plotted against the y direction (Figure 4.11 (B)), ℓ_{fc} does not show any clearly distinguishable trend.

4.4.4 Spectral Characterization of the Flow

In this section, energy spectra are shown for data characterization. Figure 4.12 presents energy spectra plotted for four different spanwise locations: $y = [0.45, 0.55, 0.65, 0.75]$ meters from the wall. Hanning windowing was used on individual segments, and over 1500 segments of the data were used for the averaging in each case. The energy spectra display well-resolved inertial ranges, and weak high-frequency noise, which shows that the data acquired was not corrupted by unwanted background noise. However, one should note that because of the finite spacial resolution of the hot-wire anemometers used for this study (≈ 0.5 mm), we do not have the confidence, at this time, that we can resolve sufficiently accurately the high-k tails of the spectra needed to evaluate the dissipation from $\epsilon = 15\nu\langle(\partial u/\partial x)^2\rangle$ and without resorting to assumptions of K41 spectral scaling.

4.4.5 PDFs, Skewness and Flatness Factors

The skewness and flatness coefficients of fluctuating velocities in shearless mixing layers flows have been reported in previous studies.[69–71] These parameters are defined by the normalized 3^{rd} and 4^{th} moments of velocity according to:

$$S_u = \frac{\langle u'^3\rangle}{\langle u'^2\rangle^{3/2}}, \qquad S_v = \frac{\langle v'^3\rangle}{\langle v'^2\rangle^{3/2}}. \tag{4.9}$$

$$K_u = \frac{\langle u'^4\rangle}{\langle u'^2\rangle^{4/2}}, \qquad K_v = \frac{\langle v'^4\rangle}{\langle v'^2\rangle^{4/2}}. \tag{4.10}$$

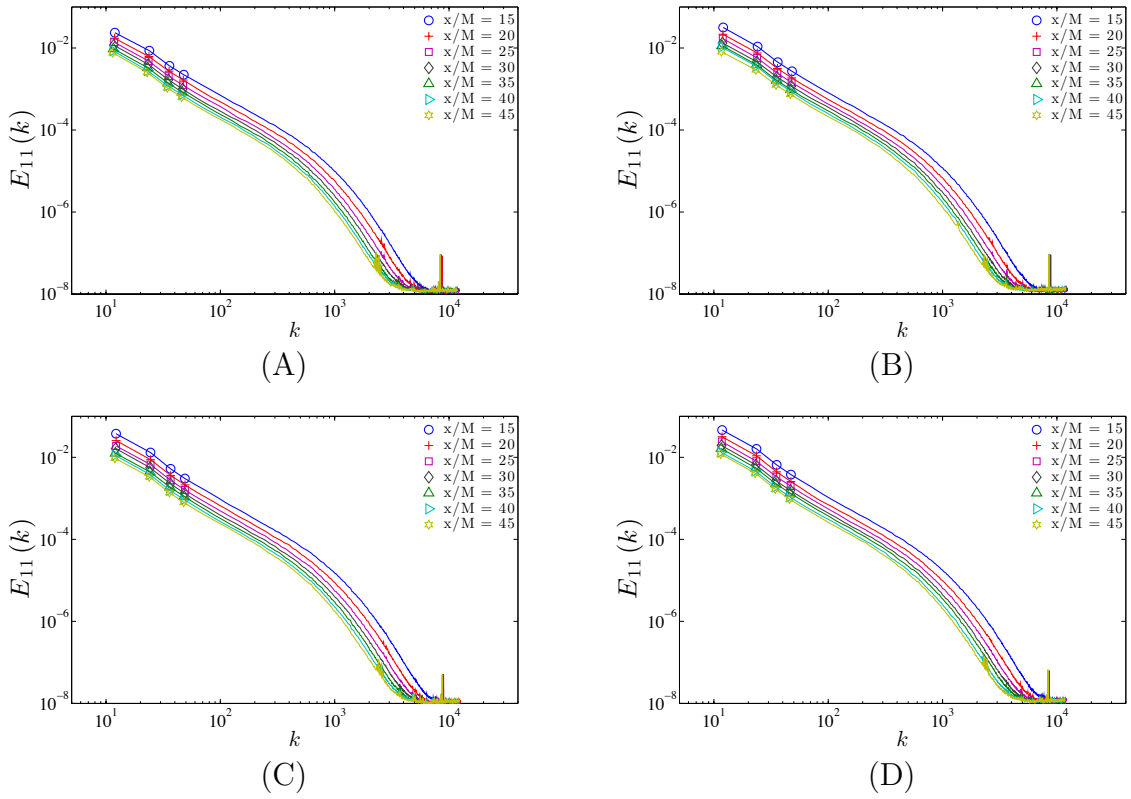

Figure 4.12: Longitudinal energy spectra plotted every $x/M = 5$ at four different spanwise positions $y = 0.45$ (A), 0.55 (B), 0.65 (C), 0.75 (D) meters off the wall. The units of $E_{11}(k)$ presented in these figures are in m^3/s^2.

Figure 4.13 shows the probability densities and skewness and flatness factors of the velocity components across the flow, at various spanwise and downstream locations.

The results obtained show clear trends, especially in the spanwise velocity component, v'. The skewness of v', shown in Figure 4.13 (C), is negative, and exhibits a decreasing slope for decreasing horizontal position, y. This trend become more apparent, and the slope becomes steeper, as the flow evolves downstream. At $x/M = 45$, the skewness is much greater in magnitude in the low-turbulence intensity region ($y/M = 2.63$), where $S_v = -0.66$, than in the highest fluctuating region

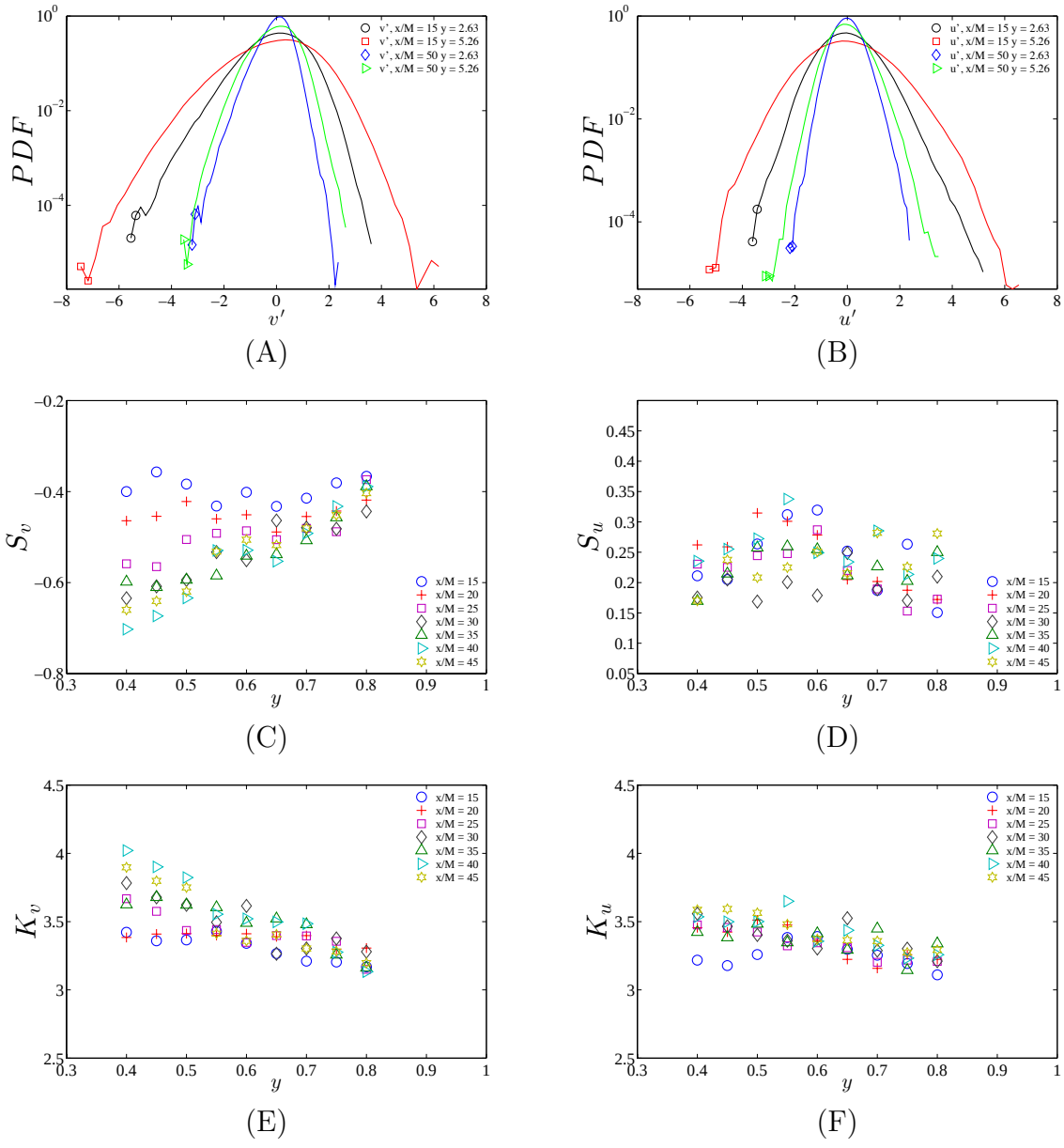

Figure 4.13: PDF, skewness, and kurtosis coefficients of streamwise and spanwise velocity components as function of the inhomogeneous direction, y.

($y/M = 5.26$), where the skewness takes a value of $S_v = -0.40$. Such trends have been observed in previous shearless mixing layer studies.[69–71] The trend shown in Figure 4.13 (C) can be explained by the fact that bursts of high energy generated in one end of the cross section of the wind tunnel, penetrate in the low energy regions as the flow is being transported downstream. By comparison, the skewness of the u-component of the flow is positive, smaller in magnitude, and does not present any clear trends.

Non-Gaussian behavior is also observed for the kurtosis (Figure 4.13 (E) and (F)). Both components of the velocity exhibit super-Gaussian behavior, and larger magnitudes are again observed for the v'-component. The latter also shows an apparent linear behavior with respect to spanwise position, y. The deviations from Gaussian statistics are stronger for low y, and high downstream distances x/M, which is self-consistent with the trends presented by the skewness of v' .

The previous studies cited above show that the peaks in skewness and flatness were not located near the center of the shearless mixing layer, but closer to the lower kinetic energy side. These results agree with the ones presented here, consistent with the view that non-Gaussian behavior arises from high kinetic energy fluctuations occasionally penetrating the low kinetic energy regions, a sign of intermittency.

4.5 Conclusions

In this study, we have explored a specific flow configuration that has not been studied in the past. Our efforts focused on introducing a linear distribution of turbulent kinetic energy only in the horizontal direction, while the kinetic energy remained homogeneous in the vertical direction. Such a flow was successfully realized, as attested to by horizontal and vertical profiles of the mean and the variance of the velocity. The lateral component of the velocity field was found to consistently exhibit higher values than the longitudinal one, leading to an isotropy ratio $I = u_{rms}/v_{rms} < 1$ throughout the flow. Despite this uniform gradient of kinetic energy, the flow remained quasi-shearless, implying that no significant production of kinetic energy existed in the test section. This characteristic enabled us to study the decay of energy by measuring velocity time series at 14 downstream and 9 spanwise locations, with constant temperature X-wire anemometers.

All the measurements performed showed that the streamwise and the spanwise decay of the turbulence variance, u^2_{rms} and v^2_{rms} respectively, as well as the kinetic energy $k = 1/2\,(3/2u^2_{rms} + 3/2v^2_{rms})$, were consistent with the power-law behavior observed in homogeneous isotropic turbulence. The values of the decay exponents were found to increase with increasing turbulence intensity across the spanwise direction.

The measured power laws, as well as the imposed linear gradient of turbulent kinetic energy at the start of the test section, allowed us to formulate an "empirical" expression that fits the behavior of the turbulent kinetic energy under these particular

conditions, of the form:

$$\frac{k(x,y)}{\langle u \rangle^2} = \beta \left(\frac{x}{x_{\text{ref}}} \right)^{-n(y)} \cdot \left(\frac{y - y_0}{M} \right)$$

This parameterization, presented in Section 4.4.2, shows good agreement with the data acquired.

The evolution of the skewness and of the flatness of the signal was also studied in this work. It was observed that penetration of the high kinetic energy eddies to the low kinetic energy region is a cause of intermittency also in this shearless turbulent flow.

Table 4.1: Decay rate exponents (n), pre-factors (A) and r.m.s. of data about the fitted power-law (σ_{fit}), obtained for the 9 horizontal position across the test section.

Without a virtual origin

	y = 40	y = 45	y = 50	y = 55	y = 60	y = 65	y = 70	y = 75	y = 80
n_u	1.10	1.18	1.19	1.27	1.28	1.30	1.31	1.34	1.34
error in fit	± 0.024	± 0.021	± 0.012	± 0.026	± 0.021	± 0.018	± 0.029	± 0.022	± 0.015
x_0/M	0	0	0	0	0	0	0	0	0
A_u	0.126	0.185	0.222	0.313	0.356	0.429	0.446	0.524	0.535
σ_{fit}	0.0142	0.0124	0.0073	0.0156	0.0125	0.0105	0.0170	0.0131	0.0091
n_v	1.17	1.17	1.16	1.17	1.18	1.17	1.19	1.22	1.26
error in fit	± 0.028	± 0.030	± 0.047	± 0.041	± 0.051	± 0.049	± 0.053	± 0.058	± 0.054
x_0/M	0	0	0	0	0	0	0	0	0
A_v	0.187	0.227	0.241	0.270	0.329	0.332	0.380	0.446	0.507
σ_{fit}	0.0165	0.0179	0.0275	0.0241	0.0302	0.0290	0.0313	0.0340	0.0321
n_k	1.14	1.17	1.18	1.21	1.22	1.23	1.25	1.27	1.30
error in fit	± 0.016	± 0.021	± 0.025	± 0.028	± 0.035	± 0.033	± 0.039	± 0.037	± 0.035
x_0/M	0	0	0	0	0	0	0	0	0
A_k	0.233	0.309	0.347	0.432	0.508	0.558	0.609	0.715	0.776
σ_{fit}	0.0097	0.0126	0.0146	0.0168	0.0208	0.019	0.0232	0.0220	0.0204

With a virtual origin

	y = 40	y = 45	y = 50	y = 55	y = 60	y = 65	y = 70	y = 75	y = 80
n_u	0.97	1.14	1.15	1.36	1.42	1.40	1.56	1.44	1.44
error in fit	± 0.0167	± 0.020	± 0.012	± 0.027	± 0.018	± 0.016	± 0.022	± 0.022	± 0.014
x_0/M	3	1	1	-2	-3	-2	-5	-2	-2
A_u	0.074	0.153	0.183	0.476	0.670	0.659	1.321	0.816	0.832
σ_{fit}	0.0111	0.0122	0.0072	0.0150	0.0096	0.0089	0.0110	0.0118	0.0077
n_v	1.39	1.39	1.50	1.52	1.53	1.52	1.55	1.59	1.64
error in fit	± 0.024	± 0.028	± 0.036	± 0.023	± 0.038	± 0.044	± 0.036	± 0.045	± 0.042
x_0/M	-5	-5	-8	-8	-8	-8	-8	-8	-8
A_v	0.495	0.597	1.132	1.283	1.586	1.581	1.873	2.280	2.728
σ_{fit}	0.0118	0.0137	0.0163	0.0106	0.0171	0.0199	0.0166	0.0204	0.0191
n_k	1.18	1.26	1.30	1.49	1.59	1.51	1.62	1.65	1.64
error in fit	± 0.017	± 0.021	± 0.017	± 0.019	± 0.022	± 0.027	± 0.019	± 0.024	± 0.023
x_0/M	-1	-2	-5	-6	-8	-6	-8	-8	-7
A_k	0.281	0.455	0.920	1.448	2.585	1.901	3.207	3.903	3.507
σ_{fit}	0.0096	0.0113	0.0086	0.0094	0.0098	0.0131	0.0089	0.0110	0.0110

Chapter 5

Further Measurements in a Shearless Kinetic Energy Gradient Flow Using Princeton's NSTAP

5.1 Introduction

This work is motivated by the study described in Chapter 4 and published in Thormann and Meneveau.[38] The experiment aims to study decaying turbulence in the presence of a linear kinetic energy gradient. Similarly to the study reported in the previous section, we introduce at some initial (reference) downstream position, x_{ref}, a kinetic energy distribution of the form: $k\left(x_{\mathrm{ref}}, y\right) \sim \ \beta \ \left(y - y_0\right)$, for some constant β and spanwise reference location y_0.

The data for this experiment are measured with the Princeton made nanoscale thermal anemometer probes (NSTAP) instead of the in-house built X-wires. The NSTAP allows for more accurate measurements of the rate of dissipation of the flow due to the probe's sub-Kolmogorov scale size, and hence, allows us to resolve all the scales in the dissipation range of the energy spectrum.

In this study, the experiment is performed to verify the measurements of spatial distribution of the decay rate exponent n as a function of spanwise direction obtained in Chatper 4. Moreover, the NSTAP allows direct measurements of ϵ, and thus captures an additional term in the energy budget (or more specifically, the budget of the streamwise normal Reynolds stress component). The experimental setup is described in Section 5.2, the flow characterization is documented in Section 5.3, and the results are presented in Section 5.4. Section 5.5 provides the conclusions drawn from this study.

5.2 Experimental Setup

In the experiments the kinetic energy gradient in y presented in Equation 5.1 is generated with the use of an active grid and screens mounted upstream of the wind-tunnel test section, iteratively designed to produce a uniform gradient of turbulent kinetic energy (TKE) without mean velocity shear (see Figure 4.1 in Chapter 4). The grid was slightly modified from the one presented in the previous study, only to

improve the linear distribution of the TKE and enhance the shearless distribution of the mean velocity in the y direction.

For a precise comparison with the study presented in Thormann and Meneveau[38], the flow is measured in the Corrsin Wind Tunnel at the same 14 downstream locations located at $x/M = [15,\ 17,\ 20,\ 22,\ 25,\ 27,\ 30,\ 32,\ 35,\ 37,\ 40,\ 42,\ 45,\ 50]$, where $M = 15$ cm is the mesh size of the grid. The acquisition is also repeated at 9 spanwise locations, starting at $y = [0.40,\ 0.45,\ 0.50,\ 0.55,\ 0.60,\ 0.65,\ 0.70,\ 0.75,\ 0.80]$ meters from the wall.

All the measurements are performed with the single component, Princeton-made, NSTAP[43–48] and acquired at 60 kHz, with a 30 kHz low-pass filter to avoid aliasing errors. 10 time series of 30 seconds are taken at each downstream location, adding up to a total of 300 seconds per point. More details on the operation NSTAP are provided in Section 1.4, in appendix B and in the cited references.[43–48]

5.3 Flow Characterization

5.3.1 Profiles

The aim of this work was to reproduce the linear kinetic energy profile introduced in Chapter 4 where the turbulent kinetic energy k, at some initial downstream location

x_{ref}, is of the form:

$$\frac{k}{\langle u \rangle^2}(x_{\text{ref}}, y) = \beta \left(\frac{y - y_0}{M} \right). \tag{5.1}$$

The slope β and the offset y_0 are fitted parameters, and thus will differ slightly from the ones presented in the previous study as the turbulence generating grid was slightly modified. However, the mesh size $M = 15.2$ cm remains the same, and is used as a length-scale to non-dimentionalize quantities presented in this chapter.

Figure 5.1 presents the data acquired while using a horizontal traverse downstream of the grid, at $x/M = 14$. This first panel, Figure 5.1 (A), shows the streamwise component of the mean velocity $\langle u \rangle$ acquired in the horizontal direction (y), which displays a quasi-shearless profile. Figure 5.1 (B) shows the distribution of $u^2_{\text{r.m.s}}$ in the flow generated by the grid, as described in Equation 5.1.

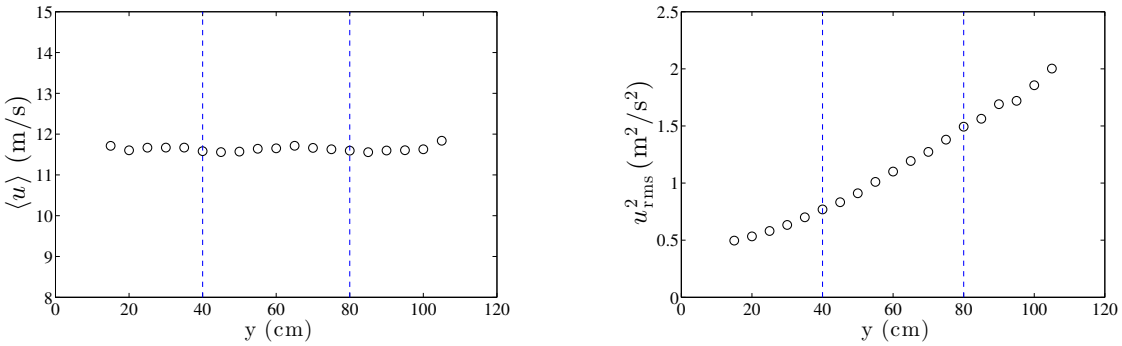

Figure 5.1: Mean velocity (A) and $u^2_{\text{r.m.s}}$ (B) of the horizontal traverse acquired at $x/M = 14$. The vertical dashed lines, plotted between $40 \leq y \leq 80$, represent the spanwise region where the downstream data were acquired.

The same acquisition methodology presented in Chapter 4 was used here, where

the data were acquired by traversing the hot-wire probe in the streamwise (x) direction, and repeated for the nine horizontal (y) positions. Since the wind tunnel was turned off between each of these nine independently calibrated data acquisitions, the data presented in Figure 5.2 (A) and (B) are normalized by the respective mean velocities recorded at the first downstream position ($x_{\text{ref}} = 15M$). Figure 5.2 (A) exhibits a nearly shearless profile, as desired. Figure 5.2 (B) presents the desired nearly linear distribution of the variance, as described in Equation 5.1, for the first downstream position. An improvement can be seen in the distribution of the profiles when comparing Figure 5.2 to the profiles presented in Figure 4.4 in Chapter 4. The mean velocity variations across the channel are of the order of $1 - 2\%$, with the largest deviation in the end of the test section. The initial distribution of kinetic energy at $x/M = 15$ shown in Figure 5.2 (B) presents a more constant gradient than the one previously studies (the coefficient of determination obtained from a linear fit of the spanwise profiles at $x/M = 15$ improved from $R^2 = 0.973$ to $R^2 = 0.987$). The improved profiles brings this study closer to the theoretical flow proposed.

5.3.2 Range of Scales

The active grid used to generate the flow presented in this study introduces a wide range of scales in the test section. Figure 5.3 presents the Taylor microscale based Reynolds number, $Re_\lambda = u_{\text{rms}}\lambda/\nu$ as a function of streamwise and spanwise locations. The Taylor microscale is obtained from $\lambda = (15\nu u_{\text{rms}}^2/\epsilon)^{1/2}$, where ϵ is the dissipation

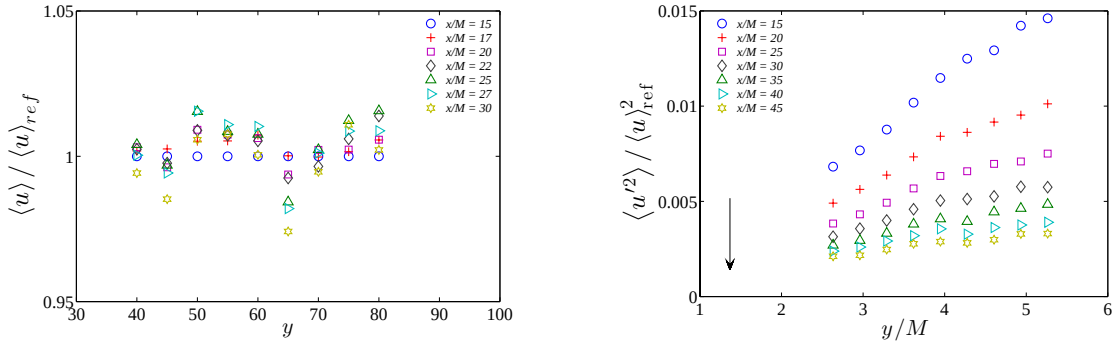

(A) (B)

Figure 5.2: (A)Mean velocity normalized by the data acquired at $x/M = 15$. (B) Lateral distribution of turbulent kinetic energy normalized by the same mean velocity.

(see Section 5.4.2 for more information on how ϵ is obtained). The Reynolds number is moderately high in the test section, and spans between $270 \leq Re_\lambda \leq 500$. As expected, the highest Reynolds numbers occur at large y, the high kinetic energy side of the cross section.

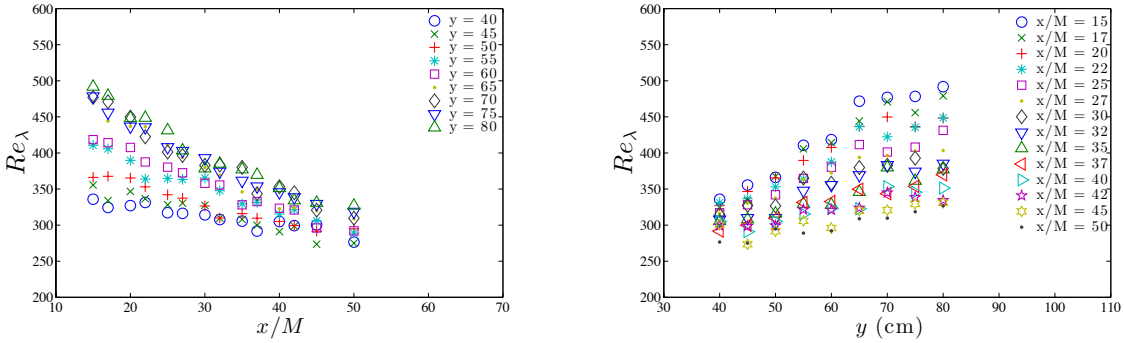

(A) (B)

Figure 5.3: Reynolds number based on the Taylor microscale presented as a function of streamwise and spanwise directions. y values quoted in the legend in (A) are given in cm.

The associated Kolmogorov scales, $\eta = (\nu^3/\epsilon)^{1/4}$, are shown in Figure 5.4. The values of η (in meters) are found to be distributed between $1.4\times10^{-4} \leq \eta \leq 3.2\times10^{-4}$,

with the smaller magnitudes found for high Re_λ, as expected. With the smallest scale exceeding $\sim$ 120 μm, we expect to fully resolve the flow using the NSTAP with its 60 μm active length, which was a point of uncertainty in the study conducted in Chapter 4 with the 0.5 mm X-wire probes. One should note that the acquisition frequency needed to capture these scales should be set to $\sim$ 100 kHz. However, as it will be demonstrated in Section 5.4.2 by analyzing the energy spectra, t the spectra decayed to very small values (negligible spectral content) for frequencies above 15 kH, i.e. Consistent with the data acquisition frequency used. Therefore, any higher data acquisition frequency would not provide any additional physical information and fall beyond the noise floor of the acquisition system at any rate.

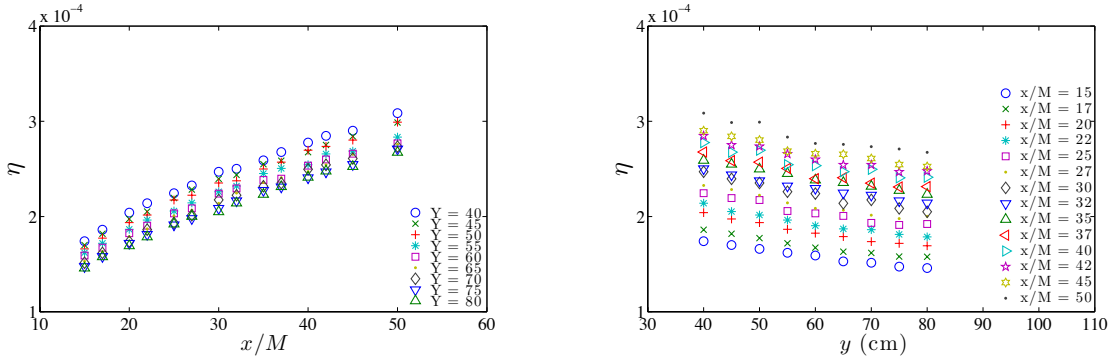

Figure 5.4: Kolmogorov scale (in meters) as a function of the streamwise and spanwise direction (y in cm).

After characterizing the small scales, we examine the distribution of the integral scale. It is computed from the longitudinal two-points correlation function, as described by Equation 4.8. The results presented in Figure 5.5 show an increase of ℓ_{fc} for increasing x/M, which is a behavior reported for homogeneous isotropic turbu-

lence,[14,38,62] and found in Thormann and Meneveau[38] as well.

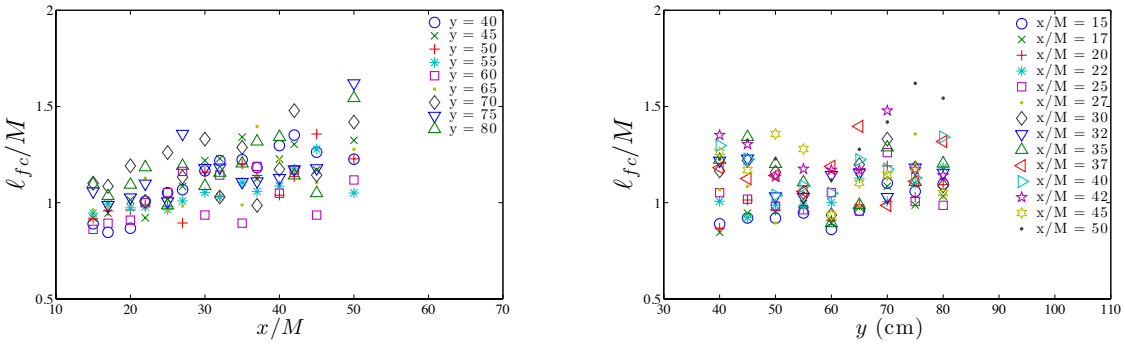

(A) (B)

Figure 5.5: The integral lengthscale, ℓ_{fc}, plotted as a function of x/M and y

5.4 Results

5.4.1 Power Law Decay

The measurements acquired in the test section at each spanwise location y with the NSTAP are compared and fitted with power laws for the streamwise component, of the form:

$$\frac{\langle u'^2 \rangle}{\langle u \rangle^2} \equiv A_u \left(\frac{x}{M} \right)^{-n_u} \tag{5.2}$$

where the coefficient A_u is a fitting parameter and n_u the fitted decay exponent. Figure 5.6 shows log-log plots of $\langle u'^2 \rangle / \langle u \rangle^2$, where very clear power law trends can

be seen. One should note that the dashed lines represent the error associated with the quality of the fits. The errorbars associated with each decay exponent are determined with a 95% (2 σ) confidence interval.

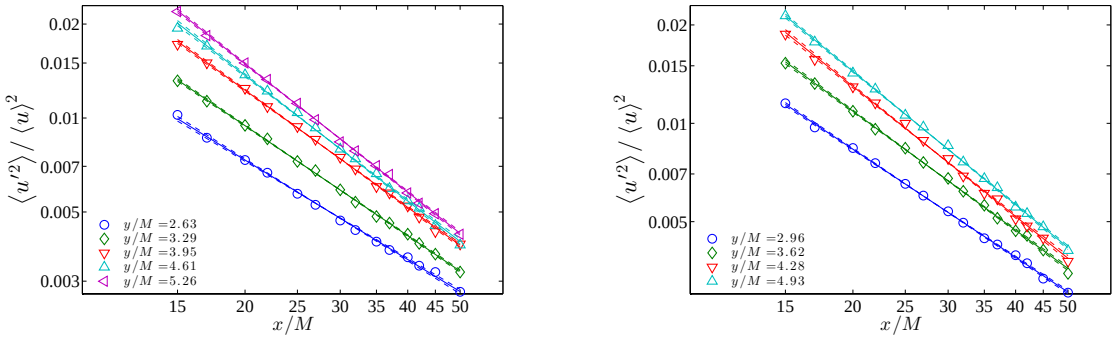

Figure 5.6: Preliminary results on decay rates of velocity component variances and turbulent kinetic energy for the nine different spanwise directions, for $\langle u'^2 \rangle / \langle u \rangle^2$.

The decay exponent n_u ranges between $n_u = 1.05$ at the lowest, and $n_u = 1.36$ at the highest. Figure 5.7 presents n_u as a function of y obtained from the fits at all y locations. The magnitude of the decay exponent measured in the streamwise direction increases for increasing turbulent kinetic energy (i.e. for increasing y), which confirms the trend and the magnitudes presented in Figure 4.6 (A) in § 4. The replication of these results with different instruments (using in-house X-wire in § 4, and the NSTAP here) lends further credibility to the reported results.

The results presented here were obtained from fitting data without a virtual origin x_{0u}, but it was shown in Chapter 4 that the addition of a virtual origin to the fit does not change the general distribution of the decay exponent with respect to the spanwise location, y.

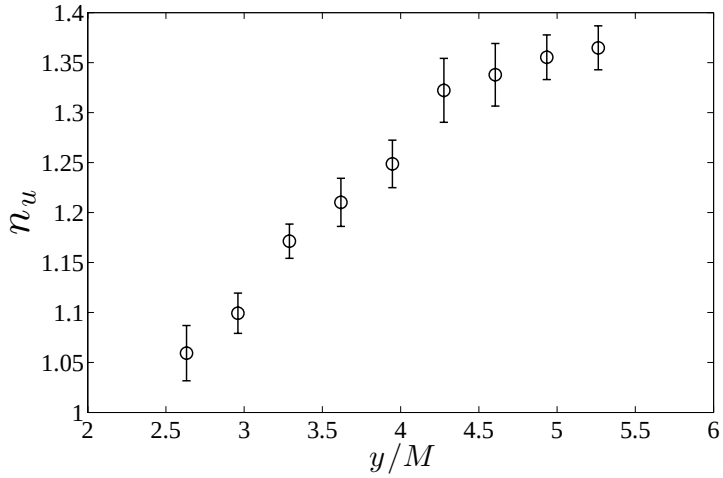

(A)

Figure 5.7: Fitted decay exponent $n(y)$ for $\langle u'^2 \rangle$ as function of spanwise position y. A clear trend of increasing in the direction of increasing turbulent kinetic energy is observed.

5.4.2 Reynolds-stress budget

Since we have a single-wire sensor, only the streamwise velocity fluctuations can be measured. Hence, strictly speaking, only the streamwise normal Reynolds stress is being measured. It is thus of interest to consider the Reynolds stress equation expressed as:[2]

$$\frac{d}{dt}\left\langle u_i' u_j' \right\rangle + \frac{\partial}{\partial x_k}\left(T_{kij}^{u} + T_{kij}^{p'} + T_{kij}^{\nu}\right) = \mathcal{P}_{ij} + \mathcal{R}_{ij} - \epsilon_{ij} \tag{5.3}$$

where $\frac{d}{dt} = \frac{\partial}{\partial t} + \langle u_k \rangle \frac{\partial}{\partial x_k}$. The flux terms on the left-hand side of the expression are defined as follow:

$$T^u_{kij} = \left\langle u'_i u'_j u'_k \right\rangle \qquad \text{turbulent convection}$$

$$T^{p'}_{kij} = \frac{2}{3}\delta_{ij} \left\langle u'_k p' \right\rangle / \rho \qquad \text{pressure transport}$$

$$T^{\nu}_{kij} = -\nu \frac{\partial \left\langle u'_i u'_j \right\rangle}{\partial x_k} \qquad \text{viscous diffusion}$$

On the right side , $\mathcal{P}_{ij} = -\left\langle u'_i u'_k \right\rangle \frac{\partial \langle u_j \rangle}{\partial x_k} - \left\langle u'_j u'_k \right\rangle \frac{\partial \langle u_i \rangle}{\partial x_k}$ is the production of kinetic energy, and the following term, the pressure-rate-of-strain tensor $\mathcal{R}_{ij}$, is defined by:

$$\mathcal{R}_{ij} = \left\langle \frac{p'}{\rho} \left(\frac{\partial u'_i}{\partial x_j} + \frac{\partial u'_j}{\partial x_i} \right) \right\rangle \tag{5.4}$$

The last term, the dissipation rate, ϵ_{ij} is a quantity that can be reasonably well approximated assuming small-scale isotropy and thus measured with the NSTAP, and is defined by:

$$\epsilon_{ij} = \frac{2}{3}\epsilon\delta_{ij} \tag{5.5}$$

where ϵ is the dissipation rate. The Reynolds stress equation can be reduced for decaying turbulence since no production of energy is present in a flow with no mean velocity gradients. Furthermore, the NSTAP is not a multi-component probe, thus only the streamwise component is of interest. Equation 5.3 can be expressed for the

u component only ($i = 1$, $j = 1$, $k = 2$, $x_1 = x$, $x_2 = y$, $u'_1 = u'$, and $u'_2 = v'$):

$$\frac{d\left\langle u'^2\right\rangle}{dt} + \frac{\partial T_{xxy}}{\partial y} = -\frac{2}{3}\epsilon, \tag{5.6}$$

where

$$T_{xxy} = \left\langle v'u'u'\right\rangle + \frac{1}{\rho}\left\langle v'p'\right\rangle - 2\nu\frac{\partial\left\langle u'u'\right\rangle}{\partial y}. \tag{5.7}$$

The derivative of the transport term is now only taken in the spanwise direction, y, as it is only in that direction that the initial gradient was introduced, and the slow x-direction gradients of turbulent fluxes are negligible compared to those in the y-direction.

The different terms that constitute the transport term cannot be measured directly because we do not have simultaneous measurements for p', u', v'. However, the clear power laws obtained in the streamwise direction give a useful analytical expression for $d\left\langle u'^2\right\rangle/dt$:

$$\frac{d\left\langle u'^2\right\rangle}{dt} = \left\langle u\right\rangle\frac{\partial\left\langle u'^2\right\rangle}{\partial x} = \left\langle u\right\rangle\frac{\partial}{\partial x}\left[\left\langle u\right\rangle^2 A\left(\frac{x}{M}\right)^{-n(y)}\right] = -n(y)A\frac{\left\langle u\right\rangle^3}{M}\left(\frac{x}{M}\right)^{-n(y)-1} \tag{5.8}$$

The Kolmogorov scale was found to be $\eta \sim 10^{-4}$m in the results presented in Figure 5.4. These scales can be resolved by the Princeton-made probe, which has an active length of $\ell = 60$ μm, thus allowing us to measure accurately the dissipation

rate. It is obtained by integrating the energy spectra after assuming local isotropy:

$$\epsilon = 15\nu \int_0^{k_{\max}} E_{11} k^2 dk \tag{5.9}$$

where E_{11} is the 1D energy spectrum of the streamwise component, u. The upper bound of the integration, $k_{\max}$, corresponds to wavenumber at which the signal reaches the electronics noise level. In practice, $k_{\max}$ is the wavenumber corresponding to the minimum of the energy spectrum. The higher wave number, i.e $k > k_{\max}$, are discarded (see Figure 5.8). Assuming local isotropy, one can plot the Kolmogorov normalized spectra and compare with the classical 1-D streamwise Kolmogorov expression:

$$\frac{E_{11}}{(\epsilon\nu^5)^{1/4}} = \frac{18}{55} C_k (k\eta)^{-5/3}. \tag{5.10}$$

The value of the Kolmogorov constant is taken to be $C_k = 1.61$, a value commonly seen in this facility,[15] and consistent with the values reported in the literature.[72] Figure 5.8 shows good agreement with Kolmogorov $-5/3$ spectrum, thus validating the values obtained for the dissipation rate.

Equations 5.8 and 5.9 provide robust methods to determine $d\left\langle u'^2 \right\rangle / dt$ and ϵ. These two terms are the only contribution to the Reynolds Stress equation in the case of homogeneous isotropic turbulence. However, in the presence of the initial energy gradient studied here, the transport term also makes contributions (see Equation

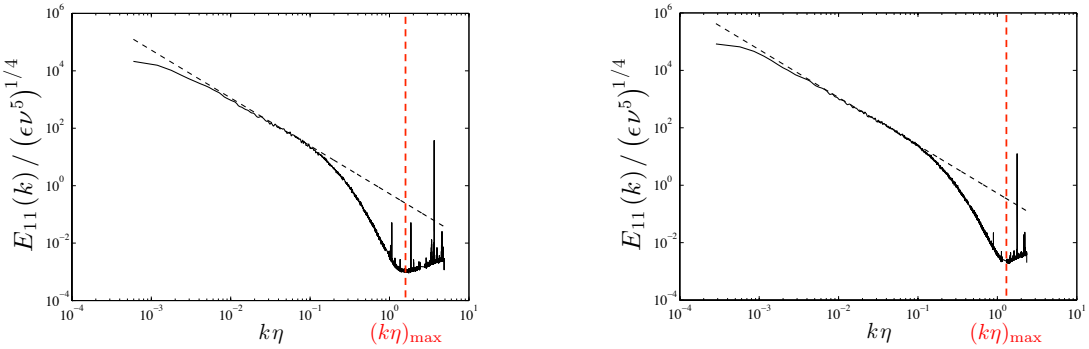

Figure 5.8: Compensated Kolmogov spectra taken at Y = 40 and x/M = 50 for figure (A), and at Y = 80 and x/M = 15 for figure (B). These two locations bound all the other measurements points, meaning that the turbulence intensity is at its highest value at Y = 80, x/M = 15, and at its lowest at Y = 40, x/M = 50. The black dash line is Eq. 5.10 with $C_k = 1.61$. The vertical red dash-lines indicate the wavenumber cutoff, $k_{\max}$ used integration performed in Eq. 5.9.

5.6).

Figure 5.9 presents the measured values for $d\langle u'^2\rangle/dt$ and $-2/3\epsilon$ at each of the 126 measurement locations. The magnitude of the total decay of energy in time is larger than the 2/3 of the dissipation rate, indicating that the difference of these two terms, $\partial T_{xxy}/dy$, is positive (see Equation 5.6). Specifically, in Figures 5.9 (C) and (D) we plot:

$$\frac{\partial T_{xxy}}{\partial y} = -\frac{d\langle u'^2\rangle}{dt} - \frac{2}{3}\epsilon \tag{5.11}$$

As it can be seen, this quantity is increasing for increasing spanwise location, y, following the initial distribution of turbulent kinetic energy and $\langle u'^2\rangle$.

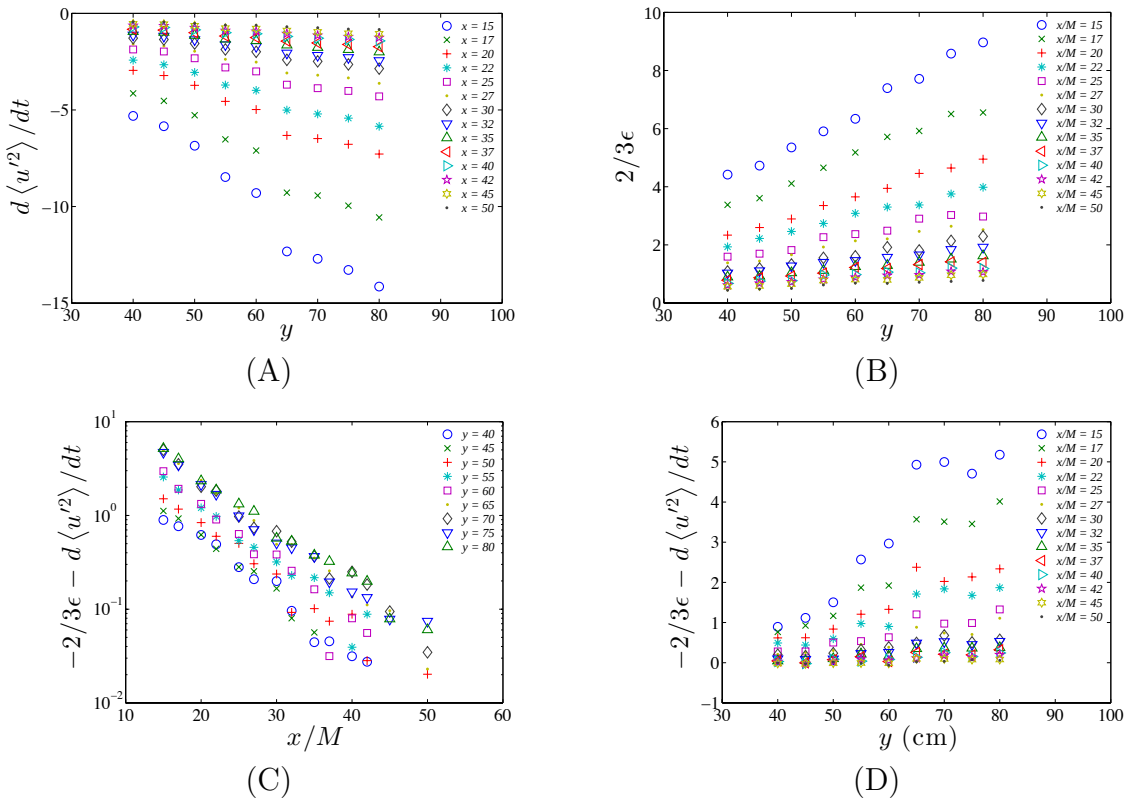

Figure 5.9: (A): $\frac{d\langle u'^2\rangle}{dt}$ as a function of y for different downstream location. (B): Similar representation of the dissipation $2/3\epsilon$. (C) and (D): Difference between $-\frac{d\langle u'^2\rangle}{dt}$ and $\frac{2}{3}\epsilon$ plotted as a function of x/M and y (in cm). All quantities plotted on the y-axes are in $\mathrm{m}^2/\mathrm{s}^3$.

The transport term, expressed in Equation 5.7 for the horizontal component, is comprised of three terms. While it is not possible to measure separately the different components of this relation, one can integrate the results obtained for $\partial T_{xxy}/\partial y$ to get the total flux across the spanwise direction as follow:

$$T_{xxy}(y) - T_{xxy}(y_{\min}) = \int_{y_{\min}}^{y} \frac{\partial T_{xxy}}{\partial y'} dy' \tag{5.12}$$

where $T_{xxy}(y_{\min})$, the constant of integration, corresponds to an initial offset. The outcomes of this integration are presented in Figure 5.10. The flux of energy across the wind tunnel has to have a positive slope with respect to the spanwise location, mandated by the observation that $|\frac{d\langle u'u'\rangle}{dt}| \geq \frac{2}{3}\epsilon$.

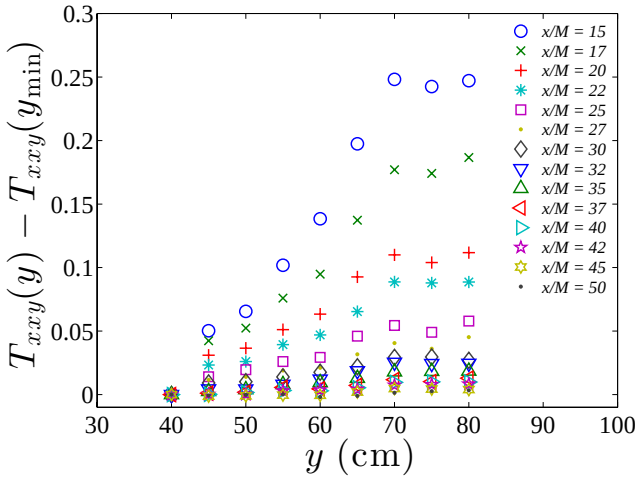

(A)

Figure 5.10: Flux $T_{xxy}(y) - T_{xxy}(y_{\min})$ (in m^3/s^3) measured in the flow, where $T_{xxy}(y_{\min})$ is an unknown offset.

Looking back at the relation for the flux presented in Equation 5.7, one can make

the assumption that the viscous contribution are small compared to the other two terms. Therefore, the results presented in Figure 5.10 are dominated by the third order moment $\langle v'u'u' \rangle$ and by the velocity-pressure fluctuation correlation $\langle v'p' \rangle / \rho$. The data gathered with the single-component probe does not allow for further investigation of these two quantities. The primary conclusions drawn from these data are that, in the presence of an initial energy gradient, a considerable spatial transport of energy is induced in the spanwise direction of the flow. The direction of which is unknown as the offset $T_{xxy}(y_{\min})$ cannot be determined. However, because we do not know the value of the offset $T_{xxy}(y_{\min})$, we do not know the sign of $T_{xxy}(y)$. Therefore, we cannot tell whether the flux is negative (which would indicate a flux in the down-gradient direction of kinetic energy), or positive (which would imply an upgradient spatial flux).

In order to provide some comparisons to possible model predictions, we compare the acquired data to gradient-diffusion and turbulent-viscosity models of the form:

$$\begin{aligned} T_{xxy} &= -\nu_{Tu} \frac{\partial \langle u'u' \rangle}{\partial y} \\ \frac{\partial T_{xxy}}{\partial y} &= -\frac{\partial}{\partial y} \left[\nu_{Tu} \frac{\partial \langle u'u' \rangle}{\partial y} \right] \end{aligned} \tag{5.13}$$

where ν_{Tu} is an unknown eddy viscosity. Expanding this relation gives:

$$\frac{\partial T_{xxy}}{dy} = -\frac{\partial \nu_{Tu}}{\partial y} \frac{\partial \langle u'u' \rangle}{\partial y} - \nu_{Tu} \frac{\partial^2 \langle u'u' \rangle}{\partial y^2}. \tag{5.14}$$

If we wish to use the measurement results for the left-hand side of this expression, we still are left with a first-order ODE for the eddy viscosity. To simplify the problem further, at least as an approximation, a linear dependence between $\langle u'u' \rangle$ and y is assumed at every downstream location. While this assumption contrasts with the findings presented in Equation 4.5, it is at least qualitatively correct when considering the data presented in Figure 5.14. If such approximation is made, Equation 5.14 simplifies to the following:

$$\frac{\partial T_{xxy}}{\partial y} = -\Lambda \frac{\partial \nu_{Tu}}{\partial y} \tag{5.15}$$

where Λ is the slope of the linear profile (β) assumed for $\langle u'u' \rangle$ at $x/M = 15$, and then a linear approximation at the subsequent downstream positions. The gradient of the eddy viscosity leads to:

$$\frac{\partial \nu_{Tu}}{\partial y} = -\frac{1}{\Lambda} \frac{\partial T_{xxy}}{\partial y} \tag{5.16}$$

Figure 5.11 presents the results obtained for $\partial \nu_{T_u}/\partial y$ using the expression above. The negative values seen on the figure indicate that the diffusivity is decreasing for increasing turbulent intensity.

We observe from Figure 5.11 that $\partial \nu_{T_u}/\partial y$ has negative values, and a negative slope. This means that either ν_{T_u} is negative (which is unexpected since it corresponds to an up-gradient flux) but increases in magnitude for larger TKE (that would

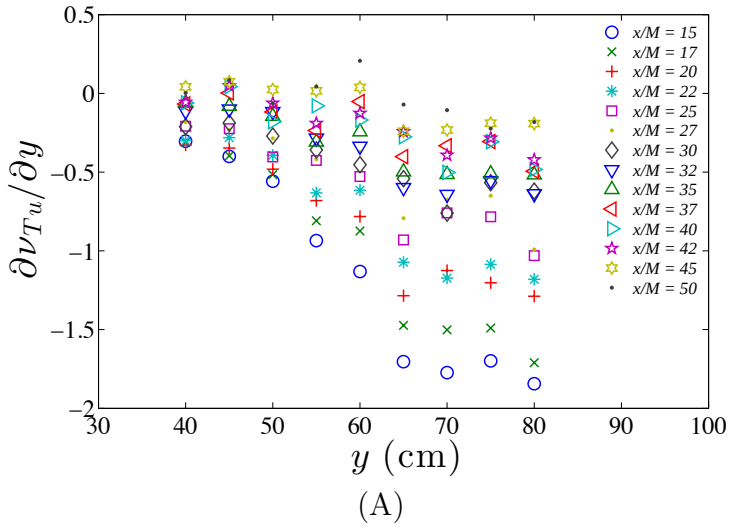

(A)

Figure 5.11: Values for $\partial\nu_{T_u}/\partial y$ (here plotted in m^2/s^3) if a gradient diffusion-model was used to characterize the flow presented in this study (see Equation 5.16).

be expected), or it is positive (expected behavior since it corresponds to a down-gradient flux) but then since its derivative is negative, the magnitude of ν_{T_u} would be a decreasing function of y (unexpected).

5.4.2.1 Comparison with X-wire data

The gradient-diffusion hypothesis presented above is often argued[2] to model only the first term of Equation 5.7, $\langle v'u'u'\rangle$, hence, the contributions from the pressure transport are not captured by this approach. The NSTAP restricts the analysis to the streamwise component. However, both streamwise (u) and spanwise (v) components of the flow were acquired in the study presented in Chapter 4. The data, which were acquired for a nearly idential flow configuration, can give insights on the contribution of the turbulent convective term, $\langle v'u'u'\rangle$. First, for comparison, Figure

5.12 presents the difference between $-2/3\epsilon$ and $d\left\langle u'u'\right\rangle/dt$, which is very similar to the results shown in Figure 5.9 (D). These two studies were independently conducted and data were acquired with two different instruments, but yet the same results are recovered.

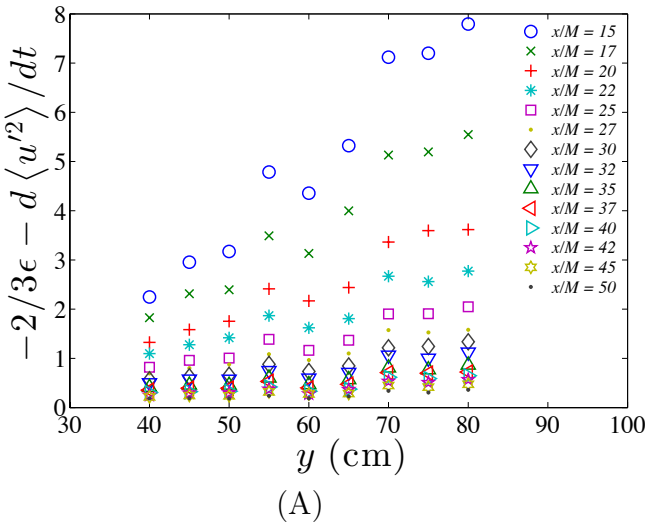

(A)

Figure 5.12: X-Wire results of $\frac{\partial T_{xxy}}{\partial y} = -\frac{2}{3}\epsilon - \frac{d\langle u'u'\rangle}{dt}$ plotted in m^2/s^3.

Figure 5.13 shows the values computed for the triple moment $\left\langle v'u'u'\right\rangle$ (see Equation 5.7) using the X-wire data. Clearly, the flux is negative, i.e. it is down-gradient as is consistent with eddy-viscosity modeling. Moreover, $\partial\left\langle v'u'u'\right\rangle/\partial y < 0$, that is to say, the (negative) flux increases in magnitude as one moves towards the high kinetic energy region. These trends are as on would expect since higher turbulence levels should be accompanied by larger eddy-diffusivity of kinetic energy. Nevertheless, comparing with Fig. 5.12 (or 5.9 (D)), the sign of $\partial\left\langle v'u'u'\right\rangle/\partial y$ is opposite to what

would be required to match or close the budget of $\langle u'u' \rangle$.

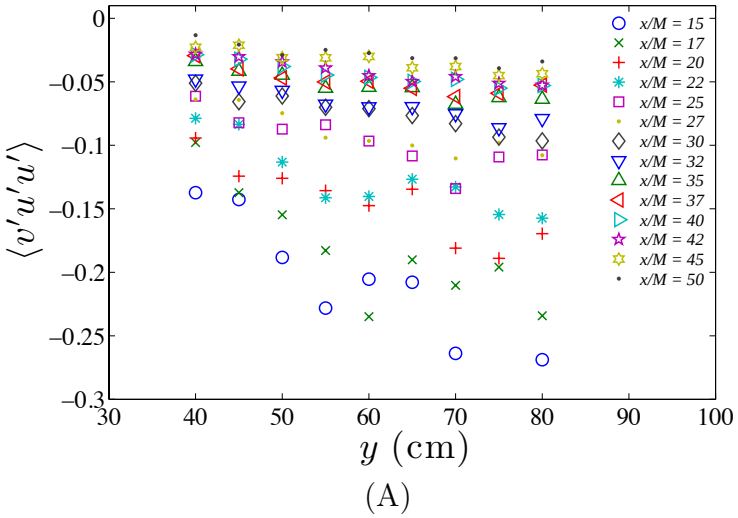

(A)

Figure 5.13: Third order moment $\langle v'u'u' \rangle$ in m^3/s^3 acquired with the X-wire.

5.4.2.2 A comparison with predictions of the $k - \epsilon$ model

In this section, we compare the results obtained for the flux T_{xxy} with the $k - \epsilon$ model:

$$\begin{aligned} T_{xxy} &= -\frac{\nu_T}{\sigma_k}\frac{\partial k}{\partial y}, \qquad \text{where } \sigma_{\mathrm{k}} = 1 \text{ and} \\ \nu_T &= c_\mu \frac{k^2}{\epsilon}, \qquad \text{with } \mathrm{c}_\mu = 0.09. \end{aligned} \tag{5.17}$$

The model is evaluated and compared with the data assuming $k = \frac{3}{2}\langle u'^2 \rangle$, and by using the values of ϵ obtained earlier by integrating the energy spectra. The energy gradient, $\frac{\partial k}{\partial y}$ is computed analytically using the kinetic energy parameterization proposed in Equation 4.5. For further simplicity, a linear function of the form $n(y) =$

$ay/M + b$ is assumed to describe the distribution of the decay exponent. The results of this parameterization are shown in Figure 5.14 and it can be seen that the model captures both the initial spanwise linear distribution of the TKE (at the reference $x_{ref} = 15M$) and the power law decay in the streamwise direction. Then, $\partial k/\partial y$ takes on the following form:

$$\begin{aligned} \frac{\partial k}{\partial y} &= \frac{\partial}{\partial y}\left[\langle u\rangle^2 \beta \left(\frac{x}{x_{ref}}\right)^{-(a\frac{y}{M}+b)} \left(\frac{y-y_0}{M}\right)\right] \\ &= \langle u\rangle^2 \frac{\beta}{M}\left(\frac{x}{x_{ref}}\right)^{-(a\frac{y}{M}+b)} - a\langle u\rangle^2 \frac{\beta}{M}\left(\frac{x}{x_{ref}}\right)^{-(a\frac{y}{M}+b)} log\left(\frac{x}{x_{ref}}\right)\left(\frac{y-y_0}{M}\right) \end{aligned} \tag{5.18}$$

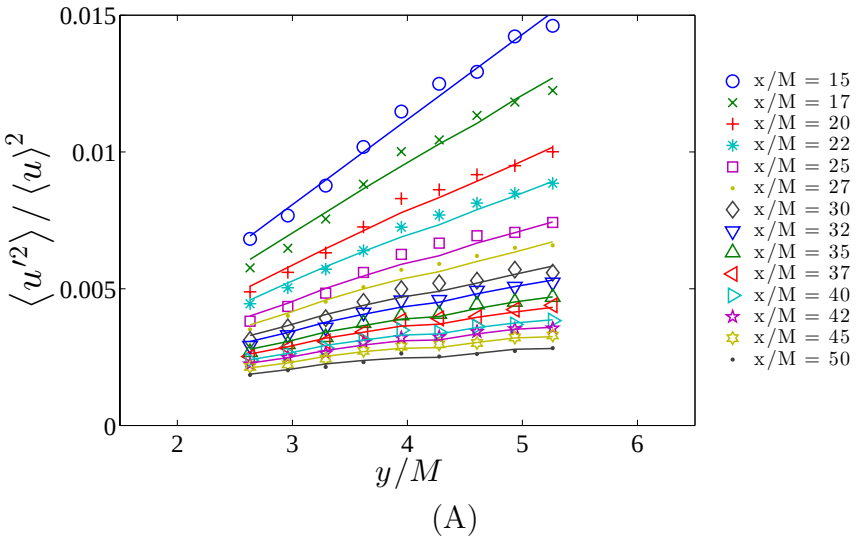

(A)

Figure 5.14: NSTAP data (symbols) compared with the parameterization presented in Equation 5.18 (solid lines).

The results of this model are presented in Figure 5.15 where the eddy diffusivity ν_T/σ_k is computed based on the parameterization of $k(x, y)$ and the measured values of ϵ, while $\partial k/\partial y$ for (B) is obtained from the parameterization in Equation 5.18. The

$k-\epsilon$ model suggests that the flux flows down-gradient and that the eddy-viscosity increases with increasing turbulent intensity. Such results are expected from this model.

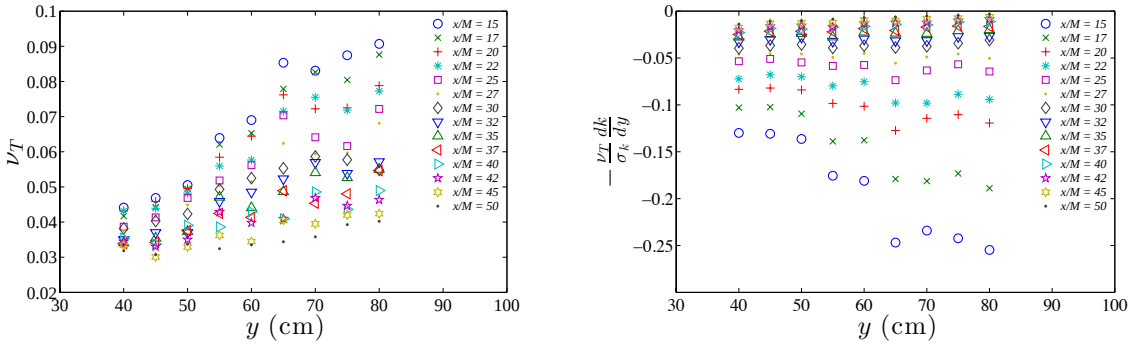

(A) (B)

Figure 5.15: (A) Eddy viscosity obtained from $\nu_T = c_\mu \frac{k^2}{\epsilon}$ (in m^2/s). (B) Flux computed with the eddy viscosity model: $T_{xxy} = -\frac{\nu_T}{\sigma_k}\frac{\partial k}{\partial y}$, plotted in m^3/s^3

Comparing Fig. 5.15 (B) with Fig. 5.13 we clearly see that the $k-\epsilon$ model is representing the $\langle v'u'u' \rangle$ term rather well. And yet, as already mentioned, this is insufficient, or even opposite, to the trends required to close the budget and explain the measurements in Figs. 5.12 and 5.9 (D). Referring back to the complete expression of the transport of kinetic energy (Equation 5.3), viscous contributions, denoted by T^{ν}_{kij}, can be assumed to be negligible, but the velocity-pressure correlation, $T^{p'}_{kij} = \langle v'p' \rangle / \rho$, therefore must play a role. In fact, the measurements results would suggest that this term must be responsible for considerable upgradient flux of kinetic energy, or of downgradient flux causing a diffusivity that is larger on the low turbulence side. Work by Lumley[73] and Demuren[74] provides support for an up-gradient influence of the velocity-pressure correlation, but the magnitude of such up-gradient flux proposed in

these prior works would be significantly smaller than what the present measurements suggest.

5.4.2.3 The pressure-rate-of-strain

The pressure-rate-of-strain tensor, $\mathcal{R}_{ij}$, is the last term in the Reynolds-stress equation that has not been studied in this Chapter (c.f. Equation 5.3 & 5.4). It has the role of redistributing the energy among the various velocity components. Since our flow is not entirely isotropic, there is a possibility that the budget also includes some redistribution from the $\langle u'u' \rangle$ term to, or from, the $\langle v'v' \rangle$ and $\langle w'w \rangle$ terms. Since we do not measure pressure-strain, we can only evaluate the pressure-strain terms using a RANS model. We use the LRR-IP model:[2]

$$\mathcal{R}_{ij} = -C_R \frac{\epsilon}{k} \left(\langle u_i u_j \rangle - \frac{2}{3} k \delta_{ij} \right) - C_2 \left(\mathcal{P}_{ij} - \frac{2}{3} \mathcal{P} \delta_{ij} \right). \tag{5.19}$$

The first term is Rotta's model for flows with zero mean velocity gradients, and thus is required for this shearless flow. However, the second term is present for cases with shear and hence can be ignored for this study. C_R, Rotta's constant, is taken to be 1.8, the usual value from the literature.[2,75] The NSTAP is a one-component only probe, hence X-wire data from §4 is used again in order to compute $k = 1/2\,(3/2\,\langle u'u' \rangle + 3/2\,\langle v'v' \rangle)$. Figure 5.16 shows the values obtained for the stream-wise normal pressure-rate-of-strain term using the Rotta model. The magnitude of

this term is relatively small compared to the ones obtained for $-d\left\langle u'^2\right\rangle/dt - 2/3\epsilon$ (Figure 5.9 (D)). For example, at low x/M, in the high turbulence region it appears to be about 10%, and about 40% in the low turbulence side. Hence, we do not see clear evidence that the pressure-strain correlation could close the budget and explain the surprising trends in the measured $\partial T_{xxy}/\partial y$ distribution. If R_{11} were 2-10 times larger than shown in Fig. 5.16, then it could explain the measurements (instead of non-trivial spatial diffusion).

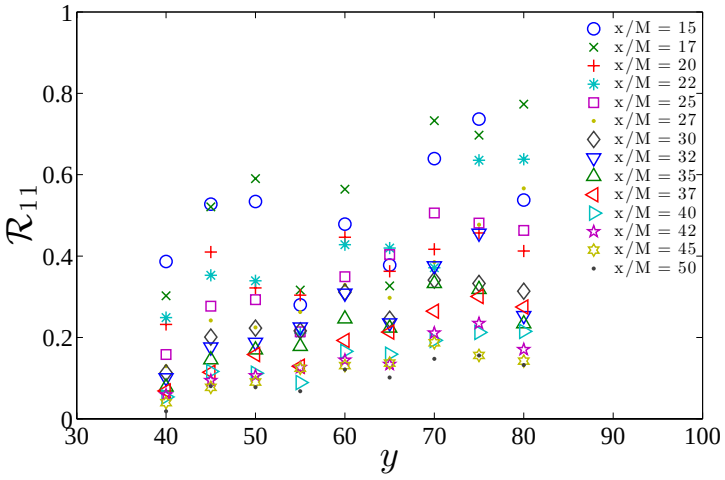

(A)

Figure 5.16: $\mathcal{R}_{11}$ using Rotta's model for cases with zero mean velocity gradients, computed using several components to obtain the kinetic energy. The results are presented in m^2/s^3

5.4.3 Study of the coefficient C_ϵ

Having accurately measured the dissipation for the this flow, one examine the coefficient C_ϵ. It is a quantity often studied in homogeneous isotropic turbulence,[27,28,37,66,67]

and often assumed to be of order unity. However, C_ϵ, defined by $C_\epsilon = \epsilon\ell/u_{\text{rms}}^3$, is a large-scale quantity and thus is not necessarily expected to be universal. Therefore, this quantity is not expected to be constant in the flow presented in this work. Figure 5.17 (A) shows an increase in C_ϵ with increasing x/M. Interestingly, Figure 5.17 (B) show lower values of C_ϵ in the high kinetic energy side (high y). This observation is represented in Figure 5.18 (A) where it is plotted against the Taylor scale based Reynolds number, Re_λ: a clearly decreasing trend of C_ϵ with increasing Re_λ is observed. The wide range of values recorded is also found in Figure 5.18 (B) where C_ϵ is plotted against the integral lengthscale ℓ_{fc}. These figures confirm the importance of the initial condition and the dependence on the large scales.

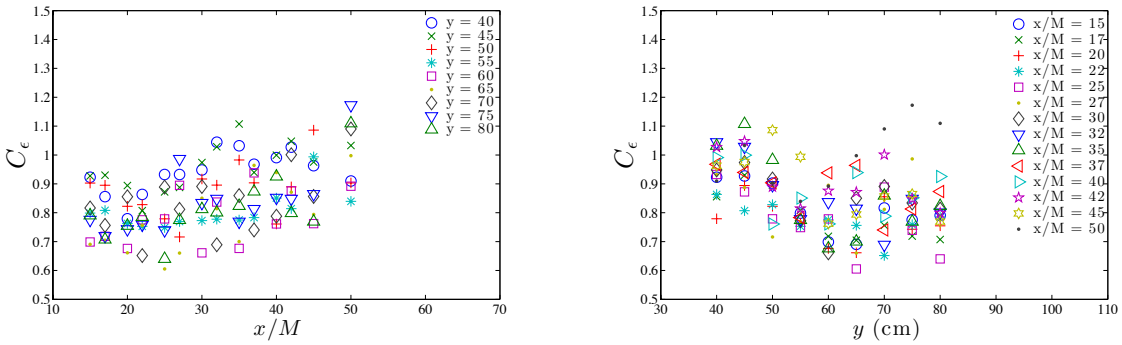

Figure 5.17: $C_\epsilon = \epsilon\frac{\ell_{fc}}{u_{\text{rms}}^3}$ plotted as a function of streamwise (A) and spanwise (B) locations

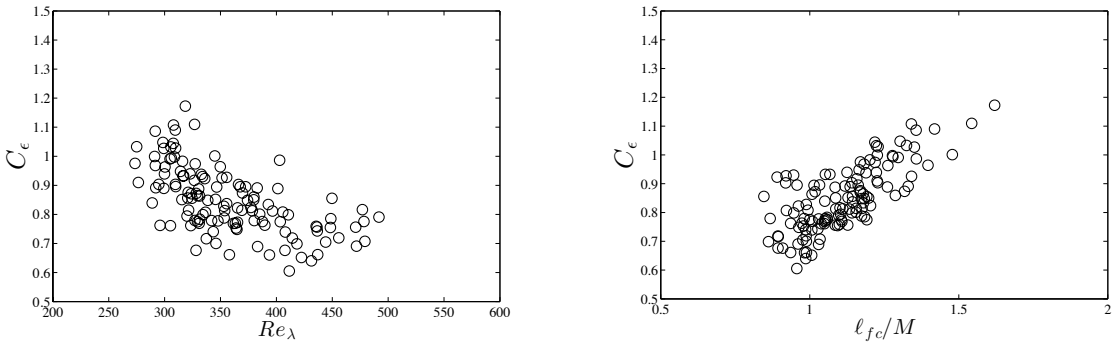

(A) (B)

Figure 5.18: C_ϵ against the values of Re_λ (A) and ℓ_{fc}/M (B) obtained in Section 5.3.2

5.5 Conclusions

In this study we repeated and validated the measurements performed and presented in Chapter 4, where an initial linear distribution of kinetic energy was introduced in the horizontal plane (y) of a quasi-shearless flow. The turbulent kinetic energy was observed to decay as a power law in time, with a decay exponent increasing for increasing kinetic energy. Beyond repeating and confirming this trend first characterized in the previous section, the novelty of this study relies on the spatial resolution of the probes used for the data acquisition. The measurements were performed using the state of the art Princeton-made nanoscale thermal anemometer probes (NSTAP). These probes enabled us to perform measurements down to the Kolmogorov scale. This allowed to perform accurate measurements of the dissipation rate, ϵ, and thus to determined with higher confidence the behavior of the spatial flux divergence, a term in the streamwise normal Reynolds stress budget.

Summarizing qualitatively the results, they show that the decay of kinetic energy is larger than can be explained by the dissipation rate at each point (taking $3/2\,\langle u'^2\rangle$ as surrogate of k). Thus, at every point energy must be lost also due to spatial diffusion due to turbulent velocity and pressure fluctuations. For this to happen, two options exist: either the flux is pointed from the high to the low kinetic energy region (down-gradient, into the negative y-direction of the flow, shown on right in Fig. 5.19). But then the flux must be larger at smaller y than at larger y (so as to cause a reduction in k at every point). Since the gradient of k is approximately constant in the y-direction, this means that the effective turbulent diffusion coefficient would have to be larger in the low-kinetic energy region. This would be somewhat surprising. The other option (shown on left of sketch in Fig. 5.19), perhaps even more surprising, would be an up-gradient flux, from the low kinetic energy region towards the high kinetic energy region. If the flux is pointed towards the positive y-direction in our flow, for there to be net loss of k at each point, it means that the flux on the high-k side must be larger than on the low-k side. This would mean a diffusion coefficient whose magnitude is larger at larger k, which seems reasonable, but the diffusion coefficient would need to be negative (up-gradient transport). A possible effect that could have explained these trends was evaluated is the pressure-strain effects since the flow is not fully isotropic. But this term was shown to be significantly smaller than what would be required to explain the trends, at least based on classical model predictions for the pressure-strain term. The other option, that the dissipation is not accurately captured due

to possible lack of small-scale isotropy appears unlikely since we would need to have underestimated the dissipation by about $30 - 40\%$ and small-scale isotropy is known to be obeyed to better accuracy than that for flows at this Reynolds number.

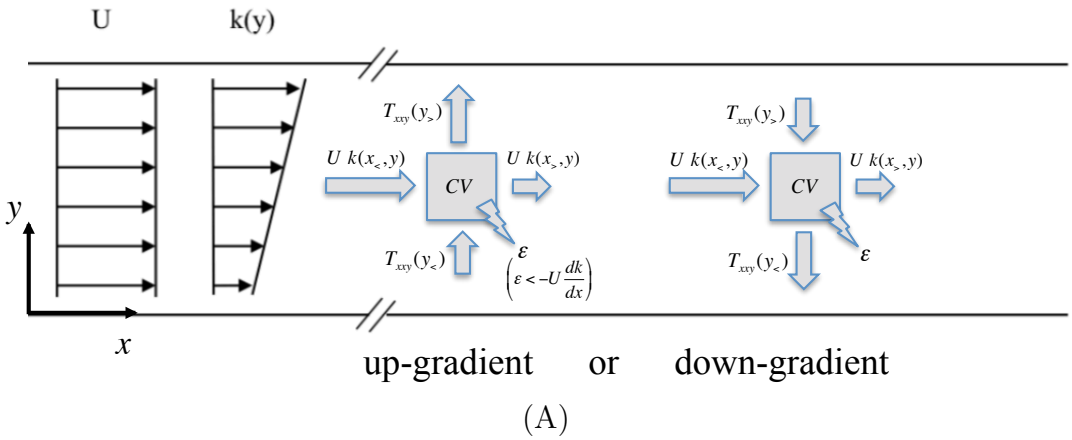

(A)

Figure 5.19: Bird's eye-view sketch of the wind-tunnel test section. Control volumes are drawn to quantitatively show the two possible options for the transport of the turbulent kinetic energy: up-gradient flux with an increasing diffusion coefficient for increasing k (left), or a down-gradient flux with a decreasing diffusion coefficient for increasing k (right)

Chapter 6

Concluding remarks

Experimental investigation of decaying turbulence under various conditions have been performed and results have been presented in this thesis. Obtaining empirical laboratory data on decaying turbulence is significant for turbulence theories and numerical simulations. The various studies presented in this thesis were all performed in the Stanley Corrsin Wind Tunnel on the Johns Hopkins University campus and the measurements were performed using hot-wire anemometers, which required adopting specialized manufacturing techniques. Guides on hot-wire anemometers are provided in two appendices.

The first part of this work focuses on the study of decaying homogeneous isotropic turbulence. In order to study unconventional injection of kinetic energy (injection at many scales), the turbulence generating grid was fitted with various types of fractal-

shaped agitators, and was used both in active and passive modes. Despite the unusual nature of the turbulence generation and claims made in several published prior studies for flows with fractal grids, no abnormal behaviors were recorded and commonly accepted power law decays were recovered. However, the precise values of the decay exponent n were found to depend on the geometry of the initial condition, although no systematic or monotonic trends with respect to Reynolds number, component anisotropy, grid fractal dimension, turbulence intensity or blockage could be discerned. Together with other recent publications,[16,17,58] our results put to rest the topic of anomalous decay of turbulence kinetic energy behind fractal grids and we confirm that the decay in the far field is clearly of power-law type. Nevertheless, the fact that the decay exponent is confirmed to not be universal suggests that in the $k-\epsilon$ model the coefficient $C_{\epsilon 2}$ may need to be chosen depending on the type of flow. Conversely, since no clear trends between the decay exponent and flow properties could be discerned from the data, no improvement to current practice of using a single value can be proposed at present.

The seconds part of the work presented in this document explores a new kind of shearless flow configuration. In this flow, a linear distribution of turbulent kinetic energy is introduced in the spanwise direction, while the kinetic energy remained homogeneous in the other direction. The flow was generated with the combination of an active grid and passive meshes. Power-law behavior was found for the streamwise

and spanwise decay of the turbulence variance, $\langle u'^2 \rangle$ and $\langle v'^2 \rangle$ respectively, as well as for the total kinetic energy, k approximated in this study as a 2D surrogate based in measurements of $\langle u'^2 \rangle$ and $\langle v'^2 \rangle$. The main result of this study is that the values of the decay exponents were found to increase with increasing turbulence intensity across the spanwise direction. Unlike the results in the prior section, here a clear trend of the decay exponent could be discerned.

The third part of this thesis is a continuation of the second chapter. It explores in greater depths the topic of shearless flows in the presence of an initial kinetic energy gradient with a novel hot wire type. The Princeton-made nanoscale thermal anemometer probe (NSTAP) was used to acquire high spatial-resolution data. The measurements confirmed the presence of a increasing decay exponent in the direction of increasing turbulence intensity, confirming the main conclusion of the previous measurements using larger X-wire probes. The NSTAP allowed us to better resolve the small-scales of the flow and determine with increased certainty precise values for the dissipation rate, ϵ (we still have to assume isotropic at the viscous scales, which is quite reasonable in this flow and high Reynolds numbers). Two behaviors could explain the counterintuitive results found in this study, with the first one being an up-gradient flux with increasing magnitude of the (negative) diffusion coefficient in the high turbulent kinetic energy side. The second possible explanation relies, instead, on having a down-gradient flux, but with a diffusion coefficient increasing in the low

turbulent kinetic energy side. However, the turbulent convective part of the flux, T^u_{kij}, is found to behave as expected and is captured rather well by gradient-diffusion models such as the $k-\epsilon$ model. This conclusion suggests that strong contributions are made by the velocity-pressure correlation, $T^{p'}_{kij}$ term. However, this term has not been extensively studied in the literature which makes any comparisons and parallels challenging to make, therefore, no strong claims on the magnitude of this terms are being made in this manuscript. The use of direct numerical simulations (DNS) could shed light on the peculiar behavior of this flow configuration.These surprising and counter-intuitive outcomes could possibly be attributed to the velocity-pressure correlation, which has been reported in previous studies[73,74] to have that effect.

With regards to future work, it would be of interest to perform DNS of decaying turbulence in the presence of a uniform kinetic energy gradient. Performing such simulations can be challenging due to the lack of periodic boundary conditions in the direction of the gradient. However, the ability of DNS to provide simultaneous velocity and pressure measurements could shed needed light on this interesting flow.

Appendix A

Hot-wire Manufacturing Process

Hot Wire Anemometry (HWA) has been a recurring topic throughout this manuscript. An introduction to their basic operation was given in section 1.4, and some details on the in-house build probes used for the studies conducted for the work presented in this thesis were given in sections 3 and 4. In this section, I will list the different steps of the manufacturing process so that it can be reproduced.

A.1 Copper Platting

The 2.5 μm tungsten wire has to be electroplated with copper so that it can be handled and soldered on the prongs of the probe. The tungsten wire has to be fixed to a bracket and then placed in a solution for the electrolysis. The composition of the solution is given is table A.1.

Table A.1: Composition of the solution needed for the electrolysis.

Distilled Water	H_2O	1000 ml
Copper Sulphate	$C_uSO_4{-}5\,H_2O$	200 g/l
Sulfuric Acid	H_2SO_4	25 ml/l
Salt	NaCl	5 g/l

For a proper mixing, 750 ml of H_2O should first be poured in a beaker. To that initial volume, one should add the copper sulfate, the sulfuric acid, and then the salt. Once the solution is mixed and reaches homogeneity, the rest of the distilled water should be added in order to obtain 1000 ml of solution. One should note that the solution is corrosive, and should be handled with care under a fume hood.

As mentioned above, the tungsten wire has to be mounted on a conductive bracket in order to go through the electrolysis process. In order to do so, one can suspend the tungsten wire between a plexiglass rod and a copper wire (taken from a thick electrical cable), as shown in figure A.1. For the electrolysis to be successful, a good electrical contact between the wire and the copper rod is needed, which is achieved by fixing the tungsten wire on the copper rod with a silver based conductive paste (ref: AI Technology product EG8020).

In this setup, the tungsten wire acts as the cathode and a copper sheet plunged into the solution is the anode. The DC current needed to drive the electrolysis is provided by a 1.5V battery until the desired amount of copper is plated onto the tungsten wire. The aim is for the wire to have a diameter go from $d_{\mathrm{Tu}} = 2.5\ \mu$m, which is the diameter of the tungsten wire, to $d_{\mathrm{Cu}} = 25\ \mu$m. Therefore, the total

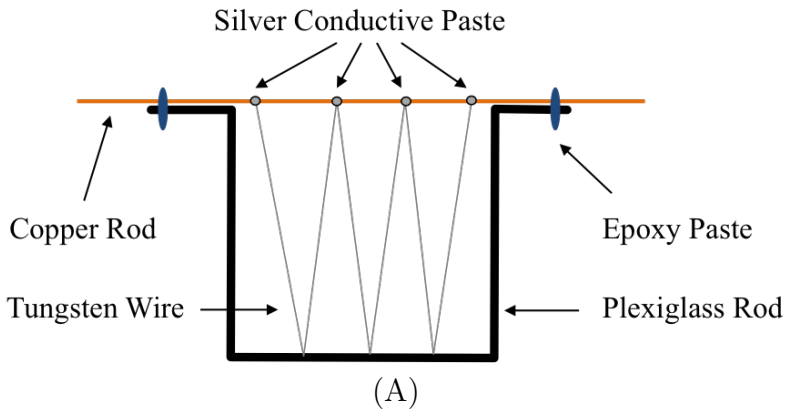

Figure A.1: Frame support used to suspend the tungsten wire in the electrolysis solution

volume of copper needed for this operation is:

$$V_{\mathrm{Cu}} = \pi L \left(\frac{{d_{\mathrm{Cu}}}^2}{4} - \frac{{d_{\mathrm{Tu}}}^2}{4} \right)$$

If the total wire length mounted on the bracket is $L = 0.2$ m, we require the electrolysis to deposit $V_{\mathrm{Cu}} = 9.7 \cdot 10^{-11}$ m^3 on the tungsten wire. Using the density of copper, $\rho_{\mathrm{Cu}} = 8930$ kg m^{-3}, we can get the total mass needed to be deposited on the wire: $m = 8.7 \cdot 10^{-7}$ kg, which corresponds to $n_{\mathrm{Cu}} = 1.36 \cdot 10^{-5}$ moles (using the molar mass of copper). Now that we have the physical quantities, let us look at the reaction for the production of copper at the cathode:

$$\mathrm{Cu}^{2+} + 2\mathrm{e}^- \rightarrow \mathrm{Cu(s)} \tag{A.1}$$

This balance equation shows that 2 moles of electrons are needed to produce 1

mole of copper. Thus, n_e=2n_{cu} = $2.72 \cdot 10^{-5}$ moles. Converting this value into a charge using Faraday's constant, we get: $2.72 \cdot 10^{-5}$ mol $\cdot$ 96485 Coulomb/mol = 2.62 Coulomb. Considering that the electrolysis circuit has a resistance of $R = 1\text{k}\Omega$ and is powered by a 1.5 V battery, the total time required to deposit the desired amount of copper on the tungsten wire is $2.72\text{C}/(1.5\text{V}/1000\Omega) \approx 30$ min.

A.2 Soldering and Etching

The copper-plated the tungsten wire obtained with the electrolysis can now be handled without too much trouble. It now can be soldered onto the prongs of the probe, which can be done by going through the following process.

1. Clean the prongs of the probe using a Q-tip and some Trichloroethylene.
2. Sand down very gently the end of the prongs using a very fine piece of sand paper.
3. Wet the tip of the prongs with some liquid soldering flux with the aid of a wooden toothpick.
4. Grind away some very small fakes (looking almost like 'dust') from the solder using a fine razor blade and place one on the tip of a given prong.
5. Use the soldering iron to 'melt' the flake on the tip of the prong. The step can be repeated until a small ball of solder is formed on all prongs.

6. Place a small amount of solder paste on the balls of solder obtained in the previous step.

7. Cut approximately 2.5 mm of the copper plated tungsten wire and place it across the tips of the two prongs.

8. Bring the soldering iron close to the tips of the prongs and apply heat so that the wire gets soldered to the probe by melting the solder ball.

Once the wire is soldered onto the tip of the prongs, one must check the resistance of the probe to make sure that a proper electrical contact has been obtained. The probes used in the lab always return $R = 4.8 - 5\ \Omega$ when a good connection was established. The copper surface must now be etched in order to expose a certain length of the tungsten wire, which will act as the active surface of the hot wire probe. In order to do so, place a drop of Nitric Acid on the hook provided in the lab. The drop will hold across the hook thanks to surface tension. While monitoring the resistance of the probe, bring the hook close to the copper-plated wire such that it now resides in the center of the nitric acid film (make sure not to make contact between the hook and the wire). Let the reaction go though until the resistance of the wire reaches 11 Ω. The wire now needs to be cleaned of all chemicals in order to prevent any reaction form occurring when an electrical current is passed through the anemometer. If the reaction does start again, the resistance of the wire will change during the operation and the calibration tables obtained prior to the measurements

will not be valid anymore. Having a stable probe is crucial for a proper operation of the system, and thus cleaning the probe throughly is an important step, which should be repeated as many times as needed. The probe must be dipped in ammonium hydroxyde, which is a base, to neutralize the reaction which was started during the etching with the nitric acid. Once the reaction is neutralized, the probe should be cleaned with deionized water to get rid of any chemicals that could be left on the surface of the wire. Trichloroethylene can be used to help the cleaning process as it is a very volatile solvant. This process must be repeated until the probe resistance is constant. Once the probe is clean, it is necessary to cure it before making any measurements. This is done by running the probe at length in a jet, wind tunnel, or any other flow. This step is important since the energy inputed by the heating current will enhance the chemical reaction mentioned above (copper etching) if any acid is left on the wire. This will cause the internal resistance of the probe to increase, which is something to avoid at all cost. Additional cleaning should be done if the probe resistance changes after the curing process, and the whole process must be repeated until a stable probe is obtained. The probe is ready to use when the curing process is completed.

Appendix B

NSTAP Operation, Calibration, and Temperature Correction

B.1 Overview

The Nano Scale Thermal Anemometer Probe has been developed by the Princeton group and has been documented in various publications,[43–48] therefore, the aim of this appendix is not to describe the background, but rather on the operation of the probes as a reference for future users. The NSTAP has an active length of 60μ m, which is about an order of magnitude smaller than the in-house built X-wire probe, which is 0.5 mm in length. The two probes are shown in figure B.1. The size of the probe is very important if one needs to measure all the scales in the energy cascade, including the Kolmogorov scale. This characteristic is valuable to determine accurately the

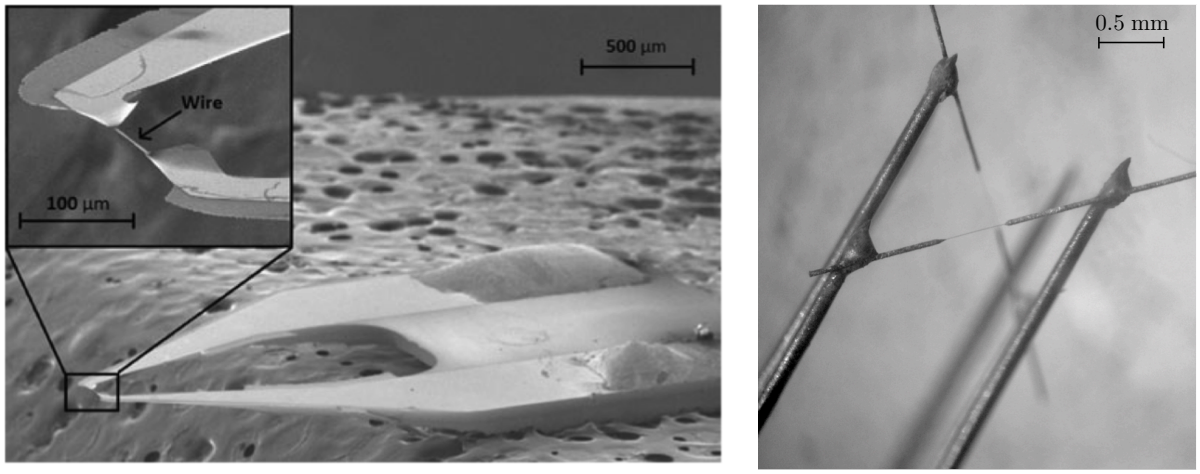

(A) (B)

Figure B.1: Hot-wire Anemoters: (A): NSTAP,[43–48] (B): In-house built X-wire probe

turbulent kinetic energy dissipation rate ϵ.

B.2 Operation

The NSTAP probes are used with the Dantec CTA with the use of an external bridge. The program controlling the operation of the CTA, StreamWare Pro, does not allow for the proper use of the NSTAP. The current that is sent when measuring the resistance is too high, which results in burning the probe. Instead, the following steps have to be taken in order to use the NSTAP properly:

- Do not connect the probe until indicated
- Setup external bridge with 'box resistance'
- Measure the probe resistance and multiply it by an overheat ratio of 1.2. Set

the resulting value on the 'box resistance' of the external bridge (make sure to include the offset of that resistance, which is $3 - 4\Omega$ usually)

- Connect a 10Ω resistance to the 'probe' input to trick the system into thinking that a "normal" probe is plugged in.

- Click on "Hardware Configuration" in StreamWare Pro, and then on "Signal Conditioner". These action will make the CTA check for the resistance of the probe, which will the the 10Ω of the resistance plug in as a 'probe'.

- It is now safe to plug in the NSTAP. Click on "operate" to activate the probe and "Standby" to put off line, which is necessary if you want to unplug it.

- From this window you can choose the offset (around $0.571V$), gain (usually 64), and low pass filter.

B.3 Calibration

Once you've chosen the proper gain and offset (see section B.2), it is time to calibrate the probe. Open up TSI's ThermalPro $\rightarrow$ IFA300 $\rightarrow$ dP & Vel Cal, then set the velocities, one by one, wanted for the calibration.

In parallel to this, acquire the data using the Labview acquisition script. The velocity is recovered by fitting the calibration data with a 4th order polynomial (see figure B.2), and then by applying these coefficient to the voltages during the experiment,

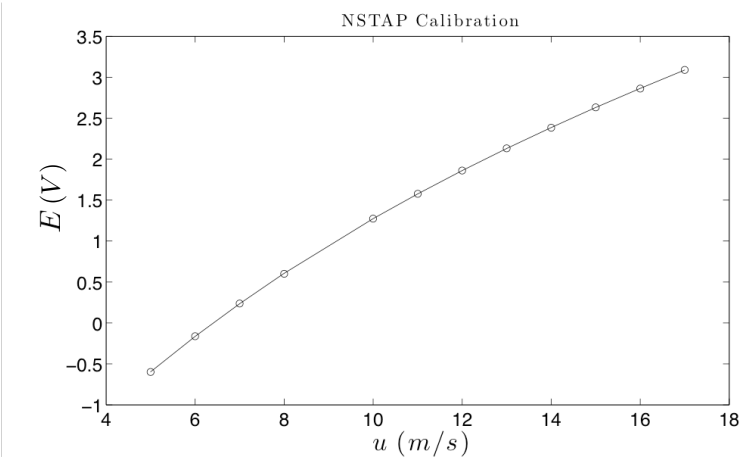

(A)

Figure B.2: 4^{th} order Polynomial fit of the points recorded during the calibration

as it is usually done:

$$U = c_0 + c_1 E + c_2 E^2 + c_3 E^3 + c_4 E^4 \tag{B.1}$$

B.4 Temperature Correction

B.4.1 Temperature Drift

The NSTAPs are extremely sensitive instrument, and as a result, are affected by the ambiant temperature changes; the resistance drifts by a large amount when the temperature of the measured flow changes. The resistance drift translates directly to a drift in the velocity measured (see figure B.3). This characteristic is a known issue in the hot wire literature[42] and is accounted for, but the behavior is more drastic

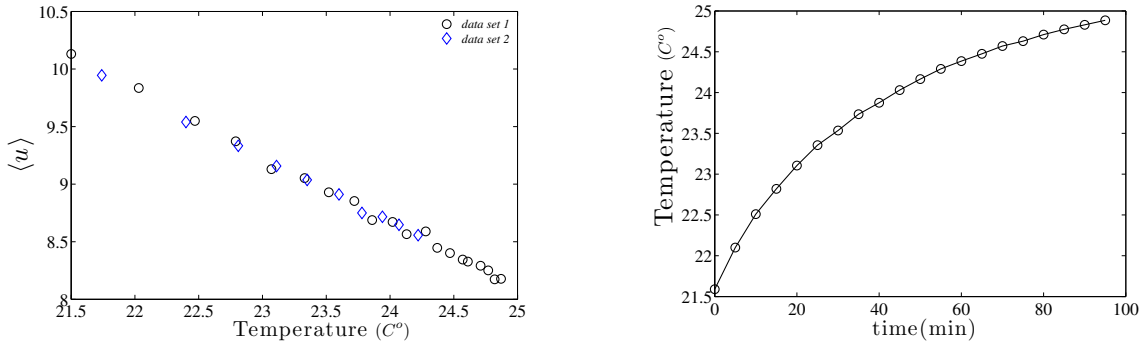

Figure B.3: Drift behavior with NSTAP: (A): Velocity drift as a function of temperature (^oC). The two data sets match almost perfectly, which shows that the probe response has a one-to-one relation with temperature, (B): Increase in temperature in the wind tunnel as a function of time.

for the NSTAP. Therefore, a different correction must be applied when using the Princeton-made nano probes.

B.4.2 Overheat Ratio and Wire Temperature

The basic operating principle of constant temperature and constant current operation is that the resistance of the sensor material increases with increasing temperature. A linear relationship of the following form between resistance R and temperature T is often assumed:

$$R_o = R_r(1 + \alpha(T_w - T_r)) \tag{B.2}$$

Where R_o is the operating resistance, R_r is the reference resistance, thus R_o/R_r is the overheat ratio. T_w is the wire temperature, T_r is the reference temperature, and α is

the temperature coefficient of resistance. It is set to $\alpha = 0.0016K^{-1}$ for the NSTAP. For example, if one is using an overheat ratio of 1.1, and the fluid temperature is 18^oC, it leads leads to $T_w = 353.6^oK$

B.4.3 Thermal Conductivity of Air as a Function of Temperature

The thermal conductivity of air can be found using the correlation given by Kannuluik and Carman (1951), where:

$$k = 418.4(5.75 \times 10^{-5}(1 + 0.00317T_f - 0.0000021T_f^2)) \tag{B.3}$$

Here T_f is the film temperature, defined by: $T_f = 1/2(T_w + T_a)$ (**Note:** The temperature are in degrees Celsius in this relation).

B.4.4 Kinematic Viscosity of Air

Since the thermal conductivity of air has to be adjusted to temperature changes, so does the kinematic viscosity. This involves adjusting the dynamic viscosity and the density, since $\nu(T) = \mu(T)/\rho(T)$.

B.4.4.1 Dynamic Viscosity μ.

Adjusting μ requires using Sutherland's law, which states the following:

$$\mu = \mu_{ref} \left(\frac{T_f}{T_{ref}} \right)^{2/3} \frac{T_{ref} + S}{T_f + S} \tag{B.4}$$

where

$$\begin{aligned} \mu_{ref} &= \text{Sutherland's viscosity} = 1.716 \times 10^{-5} \text{ kg m}^{-1}\text{s}^{-1} \\ T_{ref} &= \text{Reference temperature} = 273.15 \text{ K} \\ T_f &= \text{Film temperature} = \frac{1}{2}\left(T_w + T_{ambiant}\right) \\ S &= \text{Sutherland's constant} = 110.4\text{K} \end{aligned}$$

B.4.4.2 Density ρ.

We will use the ideal gas law to evaluate the density of air at the film temperature:

$$\rho = \frac{PM}{RT_f} \tag{B.5}$$

where

$$\begin{aligned} P &= \text{Pressure} = 101325 \text{ Pa} \\ M &= \text{Molecular Weight} = 28.96 \text{ kg kmol}^{-1} \\ R &= \text{Universal gas constant} = 8314.4 \text{ J kmol}^{-1}\text{K}^{-1} \end{aligned}$$

B.4.4.3 Kinematic Viscosity ν.

From these two relations, one can obtain the proper kinematic viscosity of air at the film temperature with the following relation:

$$\nu(T) = \frac{\mu(T)}{\rho(T)} \tag{B.6}$$

B.4.5 Compensating the Calibration Curves

In CTAs, the wire is held at a constant resistance. The Joule heating is balanced by the convective cooling (in this discussion we follow the discussion from M. Hultmark and A. J. Smits[43]):

$$\frac{E^2}{R} = hA\Delta T = \frac{k\text{Nu}}{d} A\Delta T \tag{B.7}$$

where

$$
\begin{aligned}
E &= \text{Voltage at the bridge (before applying gain and offset} \\
h &= \text{convective heat transfer coefficient} \\
k &= \text{Thermal conductivity} \\
A &= \text{Surface area of the wire} \\
\Delta T &= (T_w - T_{ambiant}) \\
\text{Nu} &= \text{Nusselt Number} = \frac{hd}{k}
\end{aligned}
$$

Since Nu = f(Re, Pr), but the Prandtl Number (Pr) has a weak dependence on temperature, we can assume Nu = f(Re). Therefore:

$$\frac{E^2}{R} = \frac{k}{d} f(\text{Re}) A \Delta T. \tag{B.8}$$

Because The resistance and the area are constant, we can rewrite it as follow:

$$E^2 = k \frac{U}{\nu} \Delta T \tag{B.9}$$

Thus, we are left with the following relation:

$$\frac{U}{\nu} = f\left(\frac{E^2}{k\Delta T}\right) \tag{B.10}$$

A 4^{th} order polynomial can be fitted to describe these two quantities. The coefficients obtained from the fit are used to then recover velocities from the recorded voltage readings (see equation B.1). This method adjusts the calibration curve to the data based on the ambient temperature changes.

Bibliography

[1] H. Tennekes and J. Lumley, *A first course in turbulence.* MIT Press, Cambridge MA, 1972.

[2] S. Pope, *Turbulent Flows.* Cambridge University Press, 2000.

[3] P. A. Davidson, *Turbulence, An Introduction for Scientists and Engineers.* Oxford University Press, 2004.

[4] G. Taylor, "Statistical theory of turbulence," *Proc. R. Soc. Lond. A.*, vol. 151, pp. 421–444, 1935.

[5] T. V. Kárman, "The fundamentals of the statistical theory of turbulence," *J. Aero. Sci.*, vol. 4, p. 131138., 1937.

[6] H. L. Dryden, "A review of the statistical theory of turbulence," *Quart. Appl. Math.*, vol. 1, p. 7, 1943.

[7] G. K. Batchelor and A. A. Townsend, "Decay of isotropic turbulence in the initial period," *Proc. R. Soc. Lond. A*, vol. 193, pp. 539–558, 1948.

[8] ——, "Decay of turbulence in the final period," *Proc. R. Soc. Lond. A*, vol. 194, pp. 527–543, 1948.

[9] A. L. Kistler and T. Vrebalovich, "Grid turbulence at large Reynolds numbers," *J. Fluid Mech.*, vol. 26, pp. 37–47, 1966.

[10] W. George, "The decay of homogeneous isotropic turbulence," *Phys. Fluids*, vol. 4, p. 1492, 1992.

[11] C. G. Speziale and P. S. Bernard, "The energy decay in self-preserving isotropic turbulence revisited," *J. Fluid Mech.*, vol. 241, pp. 645–667, 1992.

[12] J. C. Vassilicos, "Dissipation in turbulent flows," *Annu. Rev. Fluid Mech.*, vol. 47, pp. 95–114, 2015.

[13] M. S. Mohamed and J. C. Larue, "The decay power law in grid-generated turbulence," *J. Fluid Mech.*, vol. 219, pp. 195–214, 1990.

[14] G. Comte-Bellot and S. Corrsin, "The use of a contraction to improve the isotropy of grid generated turbulence," *J. Fluid Mech.*, vol. 25, p. 657, 1966.

[15] H. Kang, S. Chester, and C. Meneveau, "Decaying turbulence in an active-grid-generated flow and comparisons with large-eddy simulation," *J. Fluid Mech.*, vol. 480, pp. 129–160, 2003.

[16] P. Å. Krogstad and P. A. Davidson, "Freely decaying, homogeneous turbulence generated by multi-scale grids," *J. Fluid Mech.*, vol. 680, pp. 417–434, 2011.

[17] ——, "Near-field investigation of turbulence produced by multi-scale grids," *Phys. Fluids*, vol. 24, p. 035103, 2012.

[18] M. Sinhuber, E. Bodenschatz, and G. P. Bewley, "Decay of turbulence at high Reynolds numbers," *Phys. Rev. Lett.*, vol. 114, p. 034501, 2015.

[19] P. Orlandi, "Dns of rotating and non-rotating turbulent flows with synthetic inlet conditions," *Journal of Turbulence*, vol. 14, pp. 10–34, 2013.

[20] L. Djenidi, "Lattice-Boltzmann simulation of grid-generated turbulence," *J. Fluid Mech.*, vol. 552, p. 1335, 2006.

[21] S. M. de Bruyn Kops and J. J. Riley, "Dns of laboratory experiments in isotropic turbulence," *Phys. Fluids*, vol. 10, p. 2125, 1998.

[22] A. Kolmogorov, "The local structure of turbulence in incompressible viscous fluid for very large reynolds number," *C.R. Acad. Sci. U.S.S.R.*, vol. 30, p. 301, 1941.

[23] G. K. Batchelor, "Energy decay and self-preserving correlation functions in isotropic turbulence," *Q. Appl. Maths.*, vol. 6, pp. 97–116, 1948.

[24] P. G. Saffman, "The large-scale structure of homogeneous turbulence," *J. Fluid Mech.*, vol. 27, pp. 581–593, 1967.

[25] W. P. Jones and B. E. Launder, "The prediction of laminarization with a two-equation model of turbulence," *International Journal of Heat and Mass Transfer*, vol. 15, pp. 301–314, 1972.

[26] G. Comte-Bellot and S. Corrsin, "Simple Eulerian time correlation in full and narrow band velocity signals in grid-generated, isotropic turbulence," *J. Fluid Mech.*, vol. 48, pp. 273–337, 1971.

[27] D. Hurst and J. Vassilicos, "Scalings and decay of fractal-generated turbulence," *Phys. Fluids*, vol. 19, p. 035103, 2007.

[28] N. Mazellier and J. Vassilicos, "Turbulence without Richardson-Kolmogorov cascade," *Phys. Fluids*, vol. 22, p. 075101, 2010.

[29] P. C. Valente and J. Vassilicos, "The decay of turbulence generated by a class of multi-scale grids," *J. Fluid Mech*, vol. 687, pp. 300–340, 2011.

[30] R. Gomes-Fernandes, B. Ganapathisubramani, and J. Vassilicos, "Particule image velocimetry study of fractal-generated turbulence," *J. Fluid Mech.*, vol. 711, pp. 306–336, 2012.

[31] Y. Gagne, E. Hopfinger, and U. Frisch, "A new universal scaling for fully developed turbulence: The distribution of velocity increments," *New Trends in Nonlinear Dynamics and Pattern-Forming Phenomena*, vol. 140, pp. 63–89, 1984.

[32] H. Makita, "Realization of a large-scale turbulence field in a small wind tunnel," *Fluid Dyn. Res.*, vol. 8, pp. 53–64, 1991.

[33] L. Mydlarski and Z. Warhaft, "On the onset of high-Reynolds-number grid-generated wind tunnel turbulence," *J. Fluid Mech.*, vol. 320, pp. 331–368, 1996.

[34] ——, "Three-point statistics and the anisotropy of a turbulent passive scalar," *Phys. Fluids*, vol. 10, pp. 2885–2894, 1998.

[35] J. V. Larssen and W. J. Devenport, "On the generation of large-scale homogeneous turbulence," *Exp. Fluids*, vol. 50, pp. 1207–1223, 2011.

[36] E. Bodenschatz, G. P. Bewley, H. Nobach, M. Sinhuber, and H. Xu, "Variable density turbulence tunnel facility," *Review of Scientific Instruments*, vol. 85, p. 093908, 2014.

[37] A. Thormann and C. Meneveau, "Decay of homogeneous, nearly isotropic turbulence behind active fractal grids," *Phys. Fluids.*, vol. 26, p. 025112, 2014.

[38] ——, "Decaying turbulence in the presence of a shearless uniform kinetic energy gradient," *Journal of Turbulence*, vol. 16, pp. 442–459, 2015.

[39] J. Mathieu and E. Alcaraz, "Réalisation d'une soufflerie à haut niveau," *Comptes rendus hebdomadaires des séances de l'Académie des sciences*, vol. 261, p. 2435, 1965.

[40] M. Gad-El-Hak and S. Corrsin, "Measurements of the nearly isotropic turbulence behind a uniform jet grid," *J. Fluid Mech.*, vol. 62, p. 115, 1974.

[41] K. Thole, D. G. Bogard, and J. L. Whan-Tong, "Generating high freestream turbulence levels," *Exp. Fluids*, vol. 17, pp. 375–380, 1994.

[42] C. G. Lomas, *Fundamentals of Hot Wire Anemometry.* Cambridge University Press, 1986.

[43] M. Hultmark and A. J. Smits, "Temperature corrections for constant temperature and constant current hot-wire anemometers," *Measurements Science and Technology*, vol. 21, p. 105404, 2010.

[44] M. Vallikivi and A. J. Smits, "Fabrication and characterization of a novel nanoscale thermal anemometry probe," *J. MEMS*, vol. 99, p. 105404, 2014.

[45] A. Ashok, S. C. C. Bailey, M. Hultmark, and A. J. Smits, "Hot-wire spatial resolution effects in measurements of grid-generated turbulence," *Exp. Fluids*, vol. 53, p. 17131722, 2012.

[46] M. Vallikivi, M. Hultmark, S. C. C. Bailey, and A. J. Smits, "Turbulence measurements in pipe flow using a nano-scale thermal anemometry probe," *Exp. Fluids*, vol. 51, p. 15211527, 2011.

[47] S. C. C. Bailey, G. J. Kunjel, M. Hultmark, M. Vallikivi, J. P. Hill, K. A. Meyer, C. Tsay, C. B. Arnold, and A. J. Smits, "Turbulence measurements using a nanoscale thermal anemometry probe," *J. Fluid Mech.*, vol. 661, p. 60179, 2010.

[48] M. Hultmark, M. Vallikivi, S. Bailey, and A. Smits, "Turbulent pipe flow at extreme Reynolds numbers," *Phys. Rev. Lett.*, vol. 108, no. 9, p. 94501, 2012.

[49] K. Sreenivasan, "An update on the energy dissipation rate in isotropic turbulence," *Phys. Fluids*, vol. 10, pp. 528–529, 1998.

[50] T. V. Kármán and L. Howarth, "On the statistical theory of isotropic turbulence," *Prc. R. Soc. London Ser.*, vol. A 164, p. 192215., 1938.

[51] J. Vassilicos, "An infinity of possible invariants for decaying homogeneous turbulence," *Phys. Lett. A*, vol. 375, pp. 1010–1013, 2011.

[52] J. Gustafssona and W. K. George, "Energy spectra at low wavenumbers in homogeneous incompressible turbulence," *Physics Letters A*, vol. 375, p. 28502853, 2011.

[53] A. Llor and O. Soulard, "Comment on "energy spectra at low wavenumbers in homogeneous incompressible turbulence"," *Physics Letters A*, vol. 377, p. 11571159, 2013.

[54] R. A. Antonia, S. K. Lee, L. Djenidi, P. Lavoie, and L. Danaila, "Invariants for slightly heated decaying grid turbulence," *J. Fluid Mech.*, vol. 727, pp. 379 – 406, 2013.

[55] W. K. George and H. Wang, "The exponential decay of homogeneous turbulence," *Phys. Fluids*, vol. 21, p. 025108, 2009.

[56] M. Meldi, H. Lejemble, and P. Sagaut, "On the emergence of non-classical decay

regimes in multiscale/fractal generated isotropic turbulence," *Journal of Turbulence*, vol. 756, pp. 816–843, 2014.

[57] B. E. Launder and B. I. Sharma, "Application of the energy dissipation model of turbulence to the calculation of flow near a spinning disc," *Letters in Heat and Mass Transfer*, vol. 1, pp. 131–138, 1974.

[58] R. Hearst and P. Lavoie, "Decay of turbulence generated by a square-fractal-element grid," *J. Fluid Mech.*, vol. 741, pp. 567 – 584, 2014.

[59] E. Bodenschatz, G. P. Bewley, H. Nobach, M. Sinhuber, and H. Xu, "Decay of turbulence at high Reynolds numbers," *Rev. of Scientific instruments*, vol. 83, p. 093908, 2014.

[60] C. T. McMullen, "Hausdorff dimension and conformal dynamics III: Computation of dimension," *American Journal of Mathematics*, vol. 120(4), pp. 691–721, 1997 - Revised 2003.

[61] J. Hinze, *Turbulence: An Introduction to Its Mechanism and Theory.* McGraw-Hill, New York, 1959.

[62] P. Å. Krogstad and P. A. Davidson, "Is grid turbulence Saffman turbulence?" *J. Fluid Mech.*, vol. 642, pp. 373–394, 2010.

[63] S. Chatterjee and A. S. Hadi, "Influential observations, high leverage points, and outliers in linear regression," *Statistical Science.*, vol. 1, p. 379416, 1986.

[64] P. Lavoie, L. Djenidi, and R. A. Antonia, "Effects of initial conditions in decaying turbulence generated by passive grids," *J. Fluid Mech.*, vol. 585, pp. 395–420, 2007.

[65] P. Burattini, P. Lavoie, A. Agrawal, L. Djenidi, and R. A. Antonia, "Power law of decaying homogeneous isotropic turbulence at low Reynolds number," *Physical Review E*, vol. 73, p. 066304, 2006.

[66] K. Sreenivasan, "On the scaling of the turbulence energy dissipation rate," *Phys. Fluids*, vol. 27, p. 1048, 1995.

[67] P. Burattini, P. Lavoie, and R. A. Antonia, "On the normalized turbulent energy dissipation rate," *Phys. Fluids*, vol. 17, p. 098103, 2005.

[68] R. Seoud and J. Vassilicos, "Dissipation and decay of fractal-generated turbulence," *Phys. Fluids*, vol. 19, p. 105108, 2007.

[69] S. Veeravalli and Z. Warhaft, "The shearless turbulence mixing layer," *J. Fluid Mech.*, vol. 207, pp. 191–229, 1989.

[70] D. Tordella and M. Iovieno, "Numerical experiments on the intermediate asymtotics of shear-free turbulent transport and diffusion," *J. Fluid Mech.*, vol. 549, pp. 429–441, 2006.

[71] H. Kang and C. Meneveau, "Experimental study of an active grid-generated

shearless mixing layer and comparisons with large-eddy simulation," *Phys. Fluids*, vol. 20, p. 125102, 2008.

[72] K. Sreenivasan, "On the universality of the Kolmogorov constant," *Phys. Fluids*, vol. 7, p. 2778, 1995.

[73] J. L. Lumley, "Computational modeling of turbulent flows," *Advances in Applied Mechanics*, vol. 18, pp. 123–176, 1978.

[74] A. O. Demuren, M. M. Rogers, P. Durbin, and S. K. Lele, "On modeling pressure diffusion in non-homogeneous shear flows," *Center for Turbulence Research, Proceedings of the Summer Program*, pp. 63–73, 1996.

[75] B. E. Launder, G. J. Reece, and W. Rodi, "Progress in the development of a Reynolds-stress turbulence closure," *J. Fluid Mech.*, vol. 68, pp. 537 – 566, 1975.

Vita

Adrien R. W. M. Thormann received the B. A. degree in Physics & Astronomy from Goucher College in 2010. He then enrolled in the Mechanical Engineering M.S. program at Johns Hopkins University in the fall of 2010, and the Ph. D. program the following year, in 2011.

Starting in October 2015, Adrien will work for Renault's aerodynamics division in Paris, France.